

LA-UR- 11-04773

Approved for public release;  
distribution is unlimited.

*Title:* The BHR2 Turbulence Model: Incompressible Isotropic Decay, Rayleigh-Taylor, Kelvin-Helmholtz and Homogeneous Variable-Density Turbulence (U)

*Author(s):* K. Stalsberg-Zarling  
R. Gore

*Intended for:* Reference



Los Alamos National Laboratory, an affirmative action/equal opportunity employer, is operated by the Los Alamos National Security, LLC for the National Nuclear Security Administration of the U.S. Department of Energy under contract DE-AC52-06NA25396. By acceptance of this article, the publisher recognizes that the U.S. Government retains a nonexclusive, royalty-free license to publish or reproduce the published form of this contribution, or to allow others to do so, for U.S. Government purposes. Los Alamos National Laboratory requests that the publisher identify this article as work performed under the auspices of the U.S. Department of Energy. Los Alamos National Laboratory strongly supports academic freedom and a researcher's right to publish; as an institution, however, the Laboratory does not endorse the viewpoint of a publication or guarantee its technical correctness.

**The BHR2 Turbulence Model:  
Incompressible Isotropic Decay, Rayleigh-Taylor, Kelvin-Helmholtz  
and Homogeneous Variable-Density Turbulence (14)**

K. Stalsberg-Zarling, R. Gore

*X Division: Theory and Design, Los Alamos National Laboratory, Los Alamos, NM, USA*

**Abstract**

As part of an effort to develop a turbulence model universally applicable across a wide variety of flow configurations, a second-generation BHR turbulence model, BHR2, was developed to capture physics important in variable-density flows. This report includes a description of the model and the validation that has been performed for, primarily, Rayleigh-Taylor and Kelvin-Helmholtz instability-driven turbulence.

# The BHR2 Turbulence Model: Incompressible Isotropic Decay, Rayleigh-Taylor, Kelvin-Helmholtz and Homogeneous Variable Density Turbulence (U)

K. Stalsberg-Zarling, R. Gore

X Division: Theory and Design, Los Alamos National Laboratory, Los Alamos, NM, USA

## Abstract

As part of an effort to develop a turbulence model universally applicable across a wide variety of flow configurations, a second-generation BHR turbulence model, BHR2, was developed to capture physics important in variable-density flows. This report includes a description of the model and the validation that has been performed for, primarily, Rayleigh-Taylor and Kelvin-Helmholtz instability-driven turbulence.

Keywords: Rayleigh-Taylor; variable-density turbulence; turbulence modelling; BHR

## Table of Contents

1	Introduction.....	9
2	Background.....	13
2.1	Parameters for characterizing turbulence.....	13
2.2	Classes of turbulence .....	19
2.2.1	Kelvin-Helmholtz .....	19
2.2.2	Rayleigh-Taylor .....	22
2.2.3	Richtmyer-Meshkov .....	25
2.3	Methods for solving turbulent fluid flows: DNS, LES, RANS .....	27
2.3.1	Direct numerical simulations (DNS) .....	28
2.3.2	Large Eddy Simulations (LES).....	29
2.3.3	Averaged Navier-Stokes .....	29
3	The BHR2 turbulence model .....	35
3.1	Unmodelled and modelled equations.....	35
3.1.1	Reynolds stress model.....	36
3.1.2	Turbulent flux of internal energy.....	39
3.1.3	Turbulent mass flux .....	40
3.1.4	Turbulence kinetic energy.....	41
3.1.5	Turbulence mass flux velocity .....	44
3.1.6	Density-Specific Volume Correlation.....	47
3.1.7	Turbulence length scale .....	51
3.2	The final BHR2 turbulence model.....	52
3.3	Coefficients: defaults and their origins (in a nutshell).....	54
3.4	Initialization of turbulence quantities .....	55
3.5	RANS in RAGE.....	56
4	BHR2 model comparison to physical and computational experiments .....	56
4.1	Homogeneous isotropic decay: “grid turbulence” .....	58
4.2	Variable-density homogeneous isotropic turbulence.....	60
4.3	Kelvin-Helmholtz .....	61

4.3.1	Analysis of time evolution of the free shear layer .....	62
4.3.2	Comparison to data .....	68
4.4	Rayleigh-Taylor turbulence .....	71
4.4.1	Initialization of Rayleigh-Taylor flows in RAGE .....	71
4.4.2	Cabot and Cook RT DNS .....	76
4.4.2.1	Method and simulation details .....	77
4.4.2.2	RAGE simulation results .....	78
4.4.3	Low Atwood gas channel experiments .....	88
4.4.3.1	Description of experiment.....	88
4.4.3.2	Simulation details.....	90
4.4.3.3	Comparison of results between experiment and BHR2 .....	91
4.4.4	Rocket Rig experiments .....	95
4.4.4.1	Description of experiment.....	95
4.4.4.2	Simulation details.....	98
4.4.4.3	BHR2 simulation results .....	99
4.4.5	Linear Electric Motor (LEM) experiments .....	102
4.4.5.1	Description of experiment.....	102
4.4.5.2	Comparison of computational to experimental results .....	103
4.4.6	Self-Similar analysis for low Atwood RT .....	104
4.4.7	Effects of varying model coefficients .....	119
4.4.7.1	Effect of varying $\sigma_e$ .....	121
4.4.7.2	Effect of varying $\sigma_c$ .....	123
4.4.7.3	Effect of varying $\sigma_b$ .....	125
4.4.7.4	Effects of varying $C_4$ , $C_{a1}$ , $C_2$ and $C_b$ .....	126
4.5	Homogeneous variable-density turbulence.....	129
4.5.1	Method and simulation details .....	129
4.5.2	Results comparing BHR and BHR-2 .....	131
5	Summary and conclusions .....	135
6	Future directions .....	136
	Nomenclature.....	136
	References.....	138

## List of Figures

Figure 1.	Kelvin-Helmholtz instability driven turbulence on the planet Saturn, formed at the interaction of two bands of the atmosphere [2].	10
Figure 2.	Turbulence created by Rayleigh-Taylor instabilities evident in the <u>Crab Nebula</u> [6].	11
Figure 3.	Evolution of Kelvin-Helmholtz roll-up at an interface [19].	21
Figure 4.	Pictorial of growth of a Rayleigh-Taylor mixing layer [24].	23
Figure 5.	Density plot of the direct numerical simulation of a Rayleigh-Taylor mixing layer [25]. Red indicates the heavy fluid and blue indicates the light fluid.	24
Figure 6.	Pictorial of turbulence forming from a Richtmyer-Meshkov instability.	25
Figure 7.	The evolution of shocked and reshocked gas curtain at initial time (picture enlarged), 600 $\mu$ s, 700 $\mu$ s, 800 $\mu$ s and 900 $\mu$ s [29]. Reproduced with permission of K. Prestridge.	26
Figure 8.	Demonstration of differences in detail for Rayleigh-Taylor simulations using solution methods of various complexity and computational time [25, 30, 31].	28
Figure 9.	Illustration of the behavior of $b$ in a representation of subgrid turbulence dynamics.	48
Figure 10.	Comparison of analytic expression and BHR-2/RAGE results for homogeneous isotropic decay ( $S$ ).	60
Figure 11.	Comparison of analytic expression and BHR-2/RAGE results for homogeneous isotropic decay ( $K$ ).	60
Figure 12.	Picture of experimental free shear layer generated at Caltech University [74].	62
Figure 13.	Variation of non-dimensional $K$ with time for various initial length scales at a given resolution. The curves for 100 and 1000 are incomplete due to the mixing width reaching the edge of the domain earlier in time.	63
Figure 14.	Enlargement of the late-time region showing the variation of non-dimensional $K$ with time for various initial length scales at a given resolution.	64
Figure 15.	Variation of $\frac{dK^*/dT}{K_{final}^*}$ as a function of time.	64
Figure 16.	Variation for $\frac{dK^*/dT}{K_{final}^*}$ as a function of late-time.	65
Figure 17.	$K^*$ shown on logarithmic scale demonstrating large variation in the evolution of $K^*$ for different $S_0$ .	66
Figure 18.	The effect of mesh resolution on early-time behaviour for a small initial length scale, $S_0 = 1$ , is shown for $K^*$ plotted on a logarithmic scale.	66
Figure 19.	Effect on early time behavior of turbulence kinetic energy, $K^*$ , over a range of mesh refinements for large $S_0$ (1000).	68

Figure 20. Variation of non-dimensionalized turbulent kinetic energy, $K^*$ and growth rate, $\alpha$ , with model coefficient $C_1$ .....	69
Figure 21. Non-dimensionalization of the velocity profile of a RT mixing layer, comparing the data of Bell and Mehta [72] in red with the simulated results using BHR2 in RAGE in black. ....	70
Figure 22. Non-dimensionalization of turbulence kinetic energy across a RT mixing layer, comparing the data of Bell & Mehta [72] in red with the simulated results using BHR2 in RAGE in black.....	70
Figure 23. Non-dimensionalization of $S$ for a RT mixing layer from simulations using BHR2 in RAGE. No data was available. ....	71
Figure 24. Growth rate, $\alpha$ , as a function of the background temperature for an RT simulation using BHR2 in RAGE.....	73
Figure 25. Density versus position at various times for an Atwood number of 1.0e-4 using BHR2 in RAGE. Note, the variations observed here are of the order of 1.0e-5.....	74
Figure 26. Pressure versus position at times 0 and 1 second for an Atwood number of 0.9 using BHR2 in RAGE. ....	74
Figure 27. DNS of Rayleigh-Taylor mixing layer in the fully turbulent regime [25]......	77
Figure 28. Initial density profile for Rayleigh-Taylor DNS.....	78
Figure 29. Initial pressure profile for Rayleigh-Taylor DNS.....	79
Figure 30. Density profiles for Rayleigh-Taylor mixing layer in self-similar regime for DNS (solid) and BHR2 (dashed).....	80
Figure 31. Turbulence kinetic energy for Rayleigh-Taylor mixing layer in self-similar regime for DNS (solid) and BHR2 (dashed). ....	81
Figure 32. Mass flux velocity for Rayleigh-Taylor mixing layer in self-similar regime for DNS (solid) and BHR2 (dashed).....	82
Figure 33. Density-specific volume correlation for Rayleigh-Taylor mixing layer in self-similar regime for DNS (solid) and BHR2 (dashed). ....	82
Figure 34. A comparison of terms in the evolution equation for $b$ for Rayleigh-Taylor DNS (solid) and RAGE/BHR2 (dashed) simulations. ....	84
Figure 35. A comparison of terms in the evolution equation for turbulence kinetic energy, $K$ , for Rayleigh-Taylor DNS (solid) and RAGE/BHR2 (dashed) simulations. ....	86
Figure 36. A comparison of terms in the evolution equation for mass flux velocity, $a_z$ , for Rayleigh-Taylor DNS (solid) and RAGE/BHR2 (dashed) simulations. ....	88
Figure 37. Illustration of Texas A&M University RT gas channel experiment [79]......	89
Figure 38. Photograph of Texas A&M University RT gas channel experiment [80]......	90
Figure 39. Mix fractions for Texas A&M University RT gas channel experiments [80]......	90
Figure 40. A comparison of experimental results and RAGE simulations using BHR2: Scaled mean density as a function of location across the mixing layer. Location is non-dimensionalized by total mixing width. ....	92

Figure 41. A comparison of experimental results and RAGE simulations using BHR2: Scaled turbulent kinetic energy as a function of location across the mixing layer. Location is non-dimensionalized by total mixing width .....	92
Figure 42. A comparison of experimental results and RAGE simulations using BHR2: Scaled mass flux velocity as a function of location across the mixing layer. Location is non-dimensionalized by total mixing width.....	93
Figure 43. A comparison of experimental results and RAGE simulations using BHR2: Density-specific volume correlation as a function of location across the mixing layer. Location is non-dimensionalized by total mixing width.....	93
Figure 44. Growth rate as a function of Atwood number for the Texas A&M RT experiments [42]. .....	94
Figure 45. The "rocket rig" experimental apparatus [16].....	96
Figure 46. Tank in rocket rig experiment [16]. Provided by D. Youngs.....	97
Figure 47. Pictures of Rayleigh-Taylor mixing layers from rocket rig experiment [16].....	97
Figure 48. Data from rocket rig experiment. Reproduced from [16].....	98
Figure 49. Experimental and calculated mixing widths using BHR and BHR2 for the accel-decel coast experiment. ....	99
Figure 50. Calculated values of $b$ using BHR and BHR2 for the accel-decel-coast experiment.....	100
Figure 51. Total mix width as a function of time for the rocket rig "accel-decel-coast" experiment [15, 16, 17]. Red and blues lines are from RAGE simulations using BHR2 with the modified species equation. ....	102
Figure 52. Growth rate as a function of Atwood number for LEM [76], gas channel [42] and rocket rig [17] experiments compared with BHR2 results calculated using RAGE and RTI3D. The dashed lines are from RAGE calculations; solid lines are from RTI3D calculations. Circles, diamonds and triangles represent the LEM, gas channel and rocket rig data, respectively.....	104
Figure 53. Self-similar form for the turbulent length scale, $S$ . The green line indicates the nominal shape of the of the variable, the red, blue and black lines are the shapes at $t = 0.1, 5.0$ and $7.0$ s, respectively.....	112
Figure 54. Non-dimensional density profile. The green line indicates the nominal shape of the of the variable, the red, blue and black lines are the shapes at $t = 0.1, 5.0$ and $7.0$ s, respectively.....	112
Figure 55. Non-dimensional mass flux velocity profiles. The green line indicates the nominal shape of the of the variable, the red, blue and black lines are the shapes at $t = 0.1, 5.0$ and $7.0$ s, respectively.....	113
Figure 56. Non-dimensional turbulent kinetic energy profiles. The green line indicates the nominal shape of the of the variable, the red, blue and black lines are the shapes at $t = 0.1, 5.0$ and $7.0$ s, respectively.....	113
Figure 57. Non-dimensional "b" profiles. The green line indicates the nominal shape of the of the variable, the red, blue and black lines are the shapes at $t = 0.1, 5.0$ and $7.0$ s, respectively.....	114

Figure 58. Variation in $\alpha$ , $\alpha_k$ , $\alpha_s$ and $\alpha_c$ as a function of time exhibit self-similar behavior.....	115
Figure 59. Alpha versus time for RAGE and RTI3D. Dashed lines are RTI3D simulations; solid lines are from RAGE simulations.....	116
Figure 60. Non-dimensionalization of the individual terms in the evolution equation for $b$ . Black and blue lines indicate $t = 5$ and $t = 7$ seconds.....	117
Figure 61. Non-dimensionalization of the individual terms in the turbulent kinetic energy equation, $K$ . Black and blue lines indicate $t = 5$ and $t = 7$ seconds. ....	117
Figure 62. Non-dimensionalization of individual terms in evolution equation for mass flux velocity, $a$ . Black and blue lines indicate $t = 5$ and $t = 7$ seconds. ....	118
Figure 63. Non-dimensionalization of individual terms in evolution equation for turbulent length scale, $S$ . Plot is scaled such that it does not show full extent of diffusion terms. Black and blue lines indicate $t = 5$ and $t = 7$ seconds. ....	118
Figure 64. Non-dimensionalization of individual terms in evolution equation for turbulent length scale, $S$ . Plot shows full effect of diffusion. Black and blue lines indicate $t = 5$ and $t = 7$ seconds. ....	119
Figure 65. Profile of non-dimensionalized turbulent length scale, $S/S_{max}$ , as a function of $\sigma_e$ across the mixing layer. ....	122
Figure 66. Density profile, $\rho$ , as a function of $\sigma_e$ across the mixing layer.....	122
Figure 67. Growth rate of mixing layer, $\alpha$ , as a function of $\sigma_e$ .....	123
Figure 68. Growth rate of mixing layer, $\alpha$ , as a function of $\sigma_c$ .....	124
Figure 69. Density profile, $\rho$ , as a function of $\sigma_c$ across the mixing layer.....	124
Figure 70. Profile of non-dimensionalized density-specific volume correlation, $b/b_{max}$ , as a function of $\sigma_c$ across the mixing layer. ....	125
Figure 71. Growth rate of mixing layer, $\alpha$ , as a function of $\sigma_b$ .....	126
Figure 72. Growth rate of mixing layer, $\alpha$ , as a function of $C_4$ . ....	127
Figure 73. Growth rate of mixing layer, $\alpha$ , as a function of $C_{al}$ . ....	127
Figure 74. Growth rate of mixing layer, $\alpha$ , as a function of $C_2$ . ....	128
Figure 75. Growth rate of mixing layer, $\alpha$ , as a function of $C_{b2}$ . ....	128
Figure 76. HVDT density plot: (a) Initial time, (b) peak turbulent kinetic energy and (c) late time. Reproduced from [33].....	130
Figure 77. Turbulent kinetic energy, $K$ , mass flux velocity, $a_y$ , and density-specific volume correlation, $b$ , results for DNS of homogeneous variable-density turbulence.....	132
Figure 78. Turbulent kinetic energy, mass flux velocity and density-specific volume correlation results for DNS of homogeneous variable-density turbulence for an Atwood number of 0.25 compared with results using the first generation BHR model. ....	133
Figure 79. Turbulent kinetic energy, mass flux velocity and density-specific volume correlation results for DNS of homogeneous variable-density turbulence with an Atwood number of 0.05 compared with results using BHR2.....	134

- Figure 80. Turbulent kinetic energy, mass flux velocity and density-specific volume correlation results for DNS of homogeneous variable-density turbulence with an Atwood number of 0.25 compared with results using BHR2..... 134
- Figure 81. Turbulent kinetic energy, mass flux velocity and density-specific volume correlation results for DNS of homogeneous variable-density turbulence with an Atwood number of 0.5 compared with results using BHR2 ..... 135

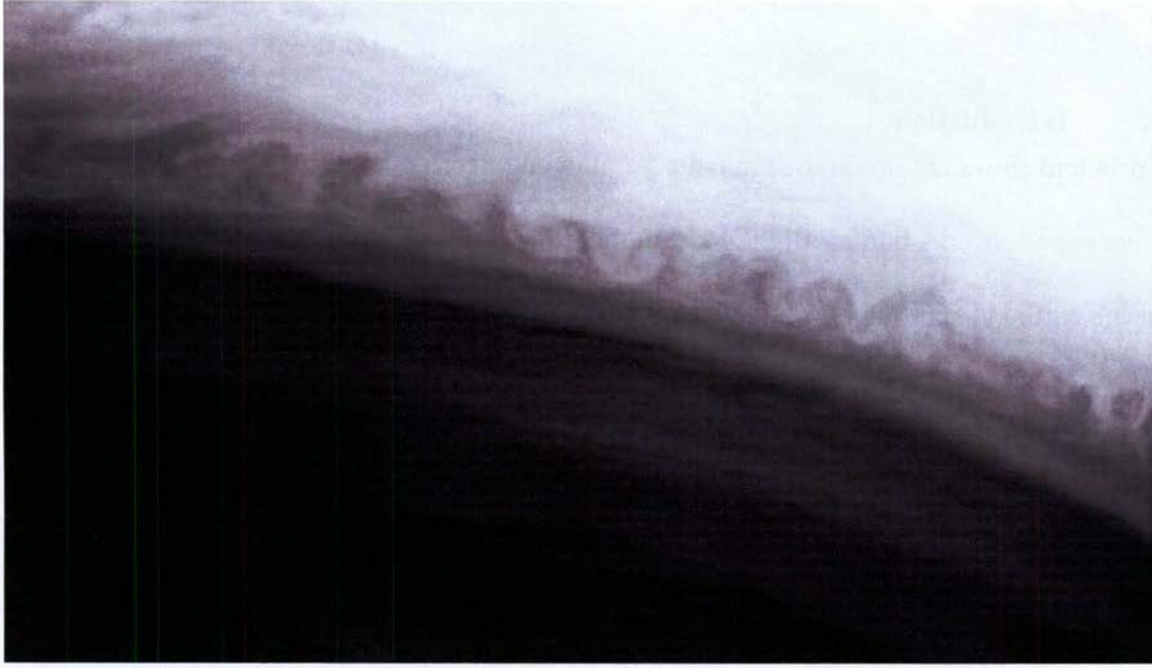
## *List of Tables*

Table 1. Coefficients defined for use in the BHR2 model.....	54
Table 2. For the high Atwood number of 0.9, growth rate results are compared for the RAGE and RTI3D codes.....	76
Table 3. Asymptotic growth rates as calculated from DNS and BHR2 simulations.....	79
Table 4. Example problem.....	107
Table 5. Model coefficients.....	110
Table 6. Model coefficients.....	110

## **1. Introduction**

Turbulent flows are ubiquitous in nature and in engineering applications. Many of us have experienced a bumpy flight and can therefore attest to turbulence in the atmosphere of the earth [1]. Turbulent mixing layers also can be observed in the skies of other planets, as shown in Figure 1, where different bands of the atmosphere interact.

Mixing layers due to turbulence develop in rivers and ocean currents where the water flows at different velocities or may have significant density variations due to differences in salinity and/or temperature [3]. As well as forming between the layers of water, these mixing layers can form at the surface, where turbulence is generated by the difference in velocities of the wind and the water. Mixing behaviour in our oceans and the atmosphere, as well as turbulent interactions between the two, largely control the weather we experience, sometimes moderating it, sometimes leading to catastrophic events, such as hurricanes and blizzards [4].



**Figure 1. Kelvin-Helmholtz instability driven turbulence on the planet Saturn, formed at the interaction of two bands of the atmosphere [2].**

On a different scale, turbulent motion is thought to be present in the dynamic behaviour of stars [5], where it can control the motion of matter in stellar flows. For example, it can be generated by gravity acting on two fluids of different densities, such as seen in the turbulent “fingers” observed for the Crab Nebula in Figure 2. According to [7], though turbulent effects lead to star formation and large-scale structure, it “remains one of the major unsolved problems in astrophysics.”



**Figure 2.** Turbulence created by Rayleigh-Taylor instabilities evident in the [Crab Nebula](#) [6].

The effects of turbulence are observed even in something as seemingly simple as the flight of a golf ball or the adding of creamer to your morning cup of coffee. Despite the fact that turbulence appears to pervade our daily lives, from the simple pleasures to the way we get around to whether we pack an umbrella for the day, a conclusive definition of turbulence has yet to be agreed upon by researchers.

According to [8], “Turbulent fluid motion is an irregular condition of flow in which the various quantities show a random variation with time and space coordinates, so that statistically distinct average values can be discerned.” An important feature is the ability to transport and mix fluid more effectively than laminar flows. Other identifying characteristics of turbulent flows include randomness, nonlinearity, diffusivity, large Reynolds numbers, three-dimensional vorticity fluctuations, dissipation, continuum behaviour and the fact that turbulent flows are *flows*, i.e., not a property of a fluid, but a feature of the flow [9, 10, 11].

One of the underlying issues with precisely defining turbulence is the scale at which one is observing the flow. At the smallest scales, called the Kolmogorov scales, viscosity dominates; if this were the observer’s frame of reference, all flows would be considered non-turbulent, or at least not require a turbulence model. In this report, however, we assume there will be significant energy containing eddies smaller than the observation frame, i.e., smaller than the grid resolution of our computer simulation, and therefore a turbulence model is required. Also, the flows we investigate have a high Reynolds number, and the comparisons are made to statistically averaged values.

With this in mind, in the Background section we will present some of the parameters used in characterizing and defining turbulent flows, such as the Reynolds number, followed by a brief introduction to turbulence as generated by Kelvin-Helmholtz, Rayleigh-Taylor and Richtmyer-Meshkov instabilities. Also, a short overview of methods used for solving/simulating turbulence is presented with emphasis on the averaged Navier-Stokes equations. In Section 3, the BHR2 turbulence model will be described. Model results are compared to physical and computational results in Section 4

for a variety of flow regimes, but primarily focussing on Rayleigh-Taylor flows. Included in this section, self-similarity analysis and the model coefficients are discussed. In the final section, we summarize the work to date, outstanding issues and plans for future model improvements and validation.

## 2. Background

### 2.1 Parameters for characterizing turbulence

Generally, turbulence is characterized by various time, length and velocity scales, as well as a series of non-dimensional numbers. The turbulence scales that will be discussed below are associated with eddies, which compose turbulent flows. The eddy defies precise definition but, according to [11], it is a turbulent motion localized within a region and it is at least coherent over that region. Eddies come in many sizes. The large eddies are described as “energy-containing”, and their energy is transferred to smaller eddies. Traditionally, it was believed that this process continues as energy is transferred successively to yet smaller and smaller eddies, in a cascading effect, until finally the energy is converted to internal energy by viscous dissipation [9]. A more contemporary viewpoint is that the large eddies interact with each other and form much smaller eddies, thus non-locally transferring energy in a manner that, again, causes eddies to become so small that viscous dissipation converts the kinetic energy to internal energy [11].

“Turbulence consists of a *continuous* spectrum of scales ranging from largest to smallest, as opposed to a *discrete* set of scales” [12]. Time, length and velocity scales associated with eddies are important in defining turbulence. In general, the turbulence velocity scale,  $u_t$ , is assumed approximately equal to  $K^{1/2}$ , where  $K$  is the mean kinetic

energy due to turbulence. The turbulence length scale, denoted by  $l_t$  here<sup>1</sup>, can describe the size of the large energy-containing eddies in a turbulent flow. The turbulent time scale, or eddy “turnover time”,  $t_t$ , can be determined by  $l_t / u_t$ . The turbulence kinetic energy is concentrated in these large energy-containing eddies of the flow. Because these eddies dominate the influence of the turbulence on the mean flow, the scales  $l_t$ ,  $u_t$  and  $t_t$  often are used to characterize the large-scale eddies.

At the other end of the energy spectrum are the Kolmogorov scales [13]. At this level, viscosity dominates the motions of the scales, which depend on the rate of dissipation of the turbulence kinetic energy,  $\varepsilon$ , and the kinematic viscosity,  $\nu$ . The Kolmogorov length, time and velocity scales are defined as  $\eta \equiv (\nu^3 / \varepsilon)^{1/4}$ ,  $\tau \equiv (\nu / \varepsilon)^{1/2}$  and  $v \equiv (\nu \varepsilon)^{1/4}$ , respectively.

There are also several dimensionless parameters used in describing turbulence. These include the Reynolds number and Mach number. The Atwood number and Schmidt number are also used, more specifically for describing variable-density flows. The Reynolds number is defined as the ratio of inertial forces to viscous forces, and therefore quantifies the relative importance of these forces for given flow conditions. From this definition it can be shown that the bulk Reynolds number  $R = UL / \nu$ , where  $U$  and  $L$  are a characteristic velocity and length of the flow, respectively (e.g., growth rate and width of the mixing layer in Rayleigh-Taylor turbulence). While other definitions can be used they all should denote dynamic quantities and not just geometrical length scales. The Reynolds number often is used to characterize whether a flow is laminar, turbulent or

---

<sup>1</sup> In the BHR2 mix model, the turbulent length scale is denoted by “S” to distinguish it from  $l_t$ . We define  $S \equiv K^{3/2} / \varepsilon$ , where  $\varepsilon = -dK / dt$  is the dissipation rate of the turbulent kinetic energy,  $K$ . It is proportional to  $l_t$ .

in transition between the two. In laminar flows, viscous forces dominate and so the Reynolds number is lower; turbulent flows occur at higher Reynolds numbers where inertial forces are dominant. In our modelling, we typically don't concern ourselves with low Reynolds number turbulence, as it may be solved directly. In the unsteady cases for which we are concerned, in addition to the Reynolds number, other considerations include initial conditions and timing.

The “turbulence Reynolds number”,  $R_t$ , can be defined as

$$R_t = \frac{u_t l_t}{\nu} = \frac{l_t^2 / \nu}{l_t / u_t}, \quad (1.1)$$

in which  $\nu$  is the kinematic viscosity. The turbulence Reynolds number gives the ratio of the viscous time scale to the turbulent convective time scale. If we define the scales in terms of turbulence kinetic energy,  $K$ , then  $R_t = K^2 / (\varepsilon \nu)$ , in which  $\varepsilon = u_t^3 / l_t$  is the dissipation rate of the turbulence kinetic energy<sup>2</sup>. Here, the rate of energy dissipation from the large scales due to the cascade process is equated to the rate at which kinetic energy is finally dissipated into heat. This is a common practice. As can be seen in the equation above, when  $R_t$  is large, the inertial forces dominate over the viscous forces. In other words, the effects of the viscous forces are relatively small, and the inertial forces are the primary mechanism acting to transfer the energy to the smaller scales. When the scale is of a size such that the viscous forces are comparable to the inertial forces, the energy is dissipated, i.e., converted to internal energy. For our modelling, we assume that the flow is fully turbulent and, therefore,  $R_t$  is large.

---

<sup>2</sup> With BHR2, we use the formulation,  $R_t = \frac{\sqrt{KS}}{\nu}$ , for the turbulence Reynolds number.

The Mach number is a dimensionless value useful for studying fluid flows in which compressibility is a significant factor. It is defined as  $M = U / c$ , in which  $U$  is the fluid velocity and  $c$  is the speed of sound in the fluid medium. The Mach number is typically used for determining when flow conditions are subsonic, transonic, supersonic or hypersonic. The turbulence Mach number, likewise, also gives a measure of compressibility effects. It is given as,  $M_t = \sqrt{2K} / \bar{c}$ , where  $K$  is the turbulence kinetic energy and  $\bar{c}$  is the mean speed of sound. It provides an estimate of compressibility effects due to fluctuating motion that is distinct from the mean velocity field [14]. The fluctuating motion in the fastest eddies can create shocklets before the bulk fluid reaches a Mach value high enough to send a shock through the flow field. For our modelling, we assume that the turbulence Mach number is small.

At this point, it may be useful to delineate between *compressed* turbulence and *compressible* turbulence. If one refers to compressed turbulence, this usually means compressing or expanding a turbulent fluid through external forces, e.g., the motion of a piston in an engine cylinder or a shock wave. Compressible turbulence refers to a turbulent flow with a high turbulence Mach number, such that individual fluctuations can create sonic conditions. This situation can result in small “shocklets” found throughout the flow [14]. The value of the turbulence Mach number indicates the likelihood of this occurring. Note that these two different processes can have very different outcomes: compressible turbulent shear layers show a greatly reduced growth rate and turbulent kinetic energy, while compressed turbulence in general shows enhanced turbulent kinetic energy.

The Schmidt number,  $Sc = \mu / (\rho D) = v / D$ , relates viscous, or momentum, diffusion to mass diffusion. Here,  $D$  is the coefficient of mass diffusivity,  $\rho$  is density,  $\mu$  is dynamic viscosity and  $v$  is kinematic viscosity. In general, we confine ourselves to  $Sc \sim O(1)$ , although in some instances, like the AWE immiscible Rocket Rig experiments [15, 16, 17], the flow is well beyond  $Sc = 1$ . The turbulent Schmidt number,  $Sc_t = v_t / D_t$ , represents the ratio of turbulent momentum diffusivity (“eddy viscosity”) to turbulent mass diffusivity. This is an indication of the transport or diffusion effects that occur due to eddy motion. This value is on the order of unity for miscible flows, which is the type of flows we address with BHR2. In the model, turbulence Schmidt number effects are represented by the model coefficient  $\sigma_c$ .

The Prandtl number,  $Pr = v / \kappa$ , in which  $\kappa$  is the coefficient of thermal conductivity, is the ratio of momentum diffusivity to heat diffusivity. Similarly, the turbulence Prandtl number can be defined as  $Pr_t = v_t / \kappa_t$ , which gives the ratio of the turbulent momentum diffusivity to the turbulent heat diffusivity. We assume a value on the order of one. In the BHR2 model, turbulence Prandtl number effects are represented by the model coefficient  $\sigma_{SIE}$ . Note, unlike the Reynolds and Mach numbers, which are a function of the flow, the Schmidt and Prandtl numbers are a function of the fluid properties and do not denote changes in the physics regimes.

In addition to the parameters listed above, variable-density flows typically are characterized by the non-dimensional Atwood number,

$$A \equiv \frac{\rho_1 - \rho_2}{\rho_1 + \rho_2}. \quad (1.2)$$

Generally, the Atwood number is used rather than the density ratio  $\rho_1 / \rho_2$ , because it naturally falls out of the linear stability analysis performed for Rayleigh-Taylor and Richtmyer-Meshkov turbulence. Additionally, mixing widths and growth rates of the turbulent flows scale with Atwood number. Under late-time self-similar conditions, it can be shown that the total mix width,  $h$ , of a Rayleigh-Taylor layer grows quadratically in time such that,

$$h = \alpha A g t^2, \quad (1.3)$$

where  $\alpha$  is a “growth constant”. This is a simplification of the Ristorcelli and Clark [18] formulation,

$$h = h_0 + 2\sqrt{\alpha A g h_0} t + \alpha A g t^2, \quad (1.4)$$

where  $h_0$  is the initial width of the mixing layer. For late-time self-similar growth, the first two terms in the right-hand side of Eqn. (1.4) are negligible compared to the third term. This is considered a reasonable assumption when comparing to experiments due to the amount of uncertainty associated with measurement of the mix width. The subject of universal late-time behaviour of the RT mix width is an ongoing research area.

There are several definitions used for calculating the mix width from experiments and simulations. The chosen definition can depend on the method of data extraction from the experiment, the preference of the person doing the analysis, the type of simulation code (e.g., compressible vs. incompressible) or some combination of all three. The width can be based on an integral value, the density, the species mass concentration, the volume fraction and so on. The lower and upper thresholds for, say, calculating the width from the density may range from 1% to 99%, 3% to 97%, 5% to 95%, etc. In this report, we typically calculate the width based on 5% and 95% of the free stream density, such that

$h = y(\rho_L + 0.95\Delta\rho) - y(\rho_L + 0.05\Delta\rho)$ , where  $\rho_L$  is the density of the lighter material and  $\Delta\rho$  is the difference in densities between the heavy and light materials.

In summary, the most useful scaling for describing the turbulent flows we are examining with the BHR2 model are as follows:

- Atwood number, to describe the potential for significant density variation effects,
- Reynolds number, an (incomplete) description of the likelihood of turbulent flow,
- Mach number (or Euler number), to describe the amount of density variation in bulk flow due to shocks and
- Turbulent Mach number, to describe the effect of compressibility of the large eddy motions.

## 2.2 *Classes of turbulence*

Turbulent flows originate from hydrodynamic instabilities. Instabilities arise from an imbalance between stabilizing and destabilizing forces in fluid motion, i.e., incipient instabilities are not counteracted at a fast enough rate by stabilizing forces acting on the fluid motion and the instability grows. A simple online search for recent articles on hydrodynamic instabilities will be enough to confirm that this is not a dead field and thousands of references are written each year. In this short introduction, we only briefly present instabilities that are driven by shear and buoyancy forces, namely Kelvin-Helmholtz and Rayleigh-Taylor, respectively, plus a short description of the shocked Richtmyer-Meshkov instability.

### 2.2.1 *Kelvin-Helmholtz*

Shear driven instabilities, called Kelvin-Helmholtz (KH) instabilities, are a common source for generating turbulence. The KH instability occurs due to a velocity difference

or shearing at an interface between two fluids flowing parallel to each other or within the same fluid, as shown in Figure 3. In (a) there are two parallel (infinite) streams flowing at different velocities,  $U_1$  and  $U_2$  with densities  $\rho_1$  and  $\rho_2$ , respectively. The faster stream is on top. The boundary between the two layers corresponds to the “shearing layer” where there is a sharp difference in the fluid velocity. In the shearing layer, the vorticity is approximately uniform and outside of the layer it is equal to zero. If an external perturbation creates an oscillation in the layer (b), this leads to higher pressure in the concave portions of the layer than in the convex portions. The amplitude of the oscillation will then grow (c), such that the upper portion of the oscillation is carried by the upper stream and the lower part is carried by the bottom stream (d). This leads to the “roll-up” effect (e) that is associated with Kelvin-Helmholtz type flows. As an example, KH “rollup” can be observed in the interaction between bands of air in the atmosphere flowing at different velocities (see Figure 1).

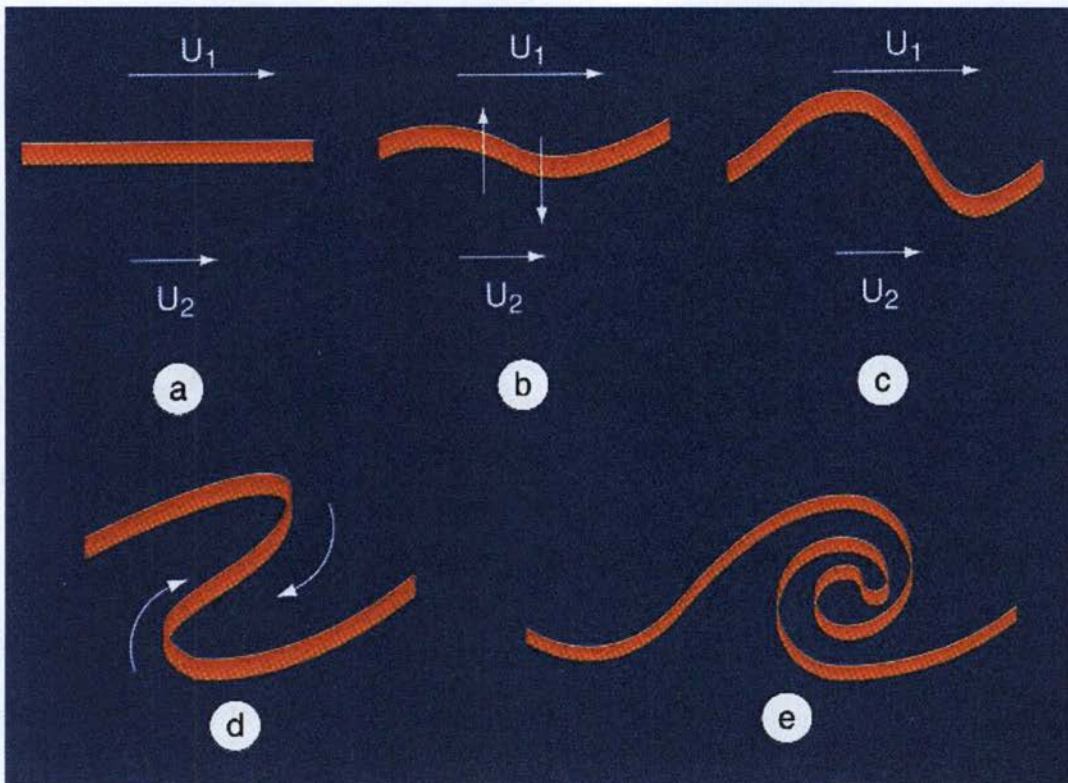


Figure 3. Evolution of Kelvin-Helmholtz roll-up at an interface [19].

The stability of this relatively simple flow can be examined by considering the basic flow of two parallel streams of fluid at different densities and flowing at different velocities. Two-dimensional linear stability analysis can be performed to examine the response of a system to small disturbances. Linear stability refers to the case when the ratio of the amplitude to the wavelength is much smaller than unity and therefore the non-linear terms in the equations can be neglected [20]. If the basic (laminar) solution to the flow is  $Q_0$ , we can add a disturbance  $Q'$  such that  $Q_0 + Q'$  is a solution of the governing equations. The disturbance can be given as  $Q' = Ae^{ik(x-ct)} = Ae^{ikx+st}$  where in 2-D the wave number is  $k \equiv 2\pi / \lambda$  and  $s$  is the propagation speed of the wave. In 3-D,  $Q' = Ae^{i(kx+ly)+st}$ , in which total wavelength is  $\tilde{k} = \sqrt{k^2 + l^2}$ . Fourier analysis can be

performed on the initial perturbation and the disturbance equation can be solved as an eigenvalue problem. Here, we provide the concluding result of this analysis for a simplified system, in this case, a system that excludes surface tension, viscosity and mass diffusion. The details can be found in [20, 21]. Following their derivations, the growth rate,  $s$ , of waves at the interface is given by,

$$s = -ik \frac{\rho_1 U_1 + \rho_2 U_2}{\rho_1 + \rho_2} \pm \left[ k^2 \rho_1 \rho_2 \left( \frac{U_1 - U_2}{\rho_1 + \rho_2} \right)^2 - \tilde{k} g \frac{\rho_1 - \rho_2}{\rho_1 + \rho_2} \right]^{1/2}, \quad (1.5)$$

where  $\rho_1$  and  $\rho_2$  are the fluid densities,  $U_1$  and  $U_2$  are the corresponding fluid velocities,  $g$  is (gravitational) acceleration normal to the flow and  $\tilde{k}$  is the total wave number. If  $s > 0$ , the mode (or wave) is growing, i.e., it is unstable; if  $s < 0$ , the mode is shrinking or stable; if  $s = 0$ , the mode is neutrally stable. If  $U_1 \neq U_2$ , there is always a large enough  $\tilde{k}$  that satisfies the requirement for instability. Note that the above analysis is also applicable to Rayleigh-Taylor flows, which are discussed in the next sections.

### 2.2.3 Rayleigh-Taylor

Instabilities also may occur simply due to density differences between fluids. These variable-density effects introduce additional driving and/or stabilizing forces. Rayleigh-Taylor (RT) instabilities occur due to a mismatch between the pressure gradient and the density gradient between two different density fluids [22, 23]. That is, an interface between fluids of different densities is Rayleigh-Taylor unstable if  $\nabla p \bullet \nabla \rho < 0$ , where  $\nabla p$  is the pressure gradient and  $\nabla \rho$  is the density gradient. The basic mechanism that amplifies or causes the perturbations to grow is the baroclinic generation of vorticity

which is given by  $\frac{1}{\rho^2} \nabla p \times \nabla \rho$ .

The RT instability is commonly buoyancy driven. A classic example is a heavy fluid sitting atop a light fluid in the presence of gravitational acceleration, studied by Taylor in 1950 [23]. The mixing layer starts first as small amplitude perturbations, which initially grow exponentially with time (see Figure 4).

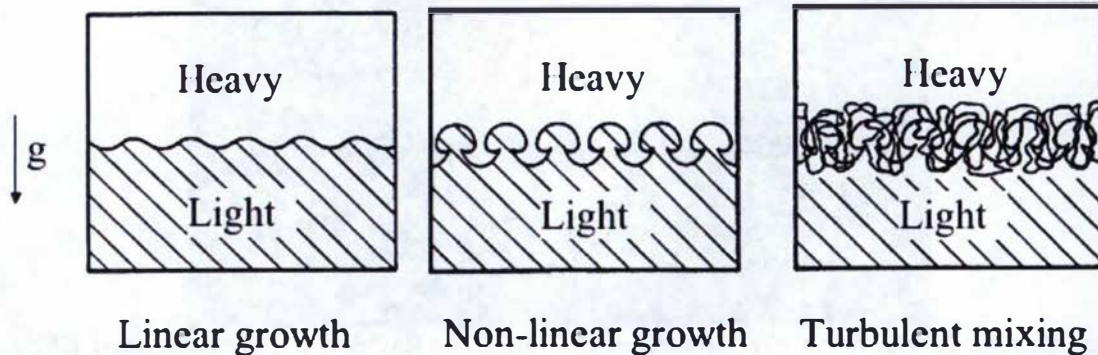


**Figure 4.** Pictorial of growth of a Rayleigh-Taylor mixing layer [24].

The layer then develops nonlinearly as “bubbles” and “spikes” form from the light and heavy fluids, respectively. Eventually, the two fluids within the layer become chaotic and are well-mixed, i.e., turbulent (see Figure 5). This process continues as long as the pressure gradient-density gradient mismatch exists. Here, as with most issues surrounding hydrodynamic instabilities, transition and turbulent flows, one must be careful with terminology. The linear growth rate (for a single mode) refers to the ability to linearize the equations, which have the solution of exponential growth. The non-linear phase has growth proportional to time, i.e., it is linear; the turbulent phase, by definition not single mod, has growth proportional to time squared.

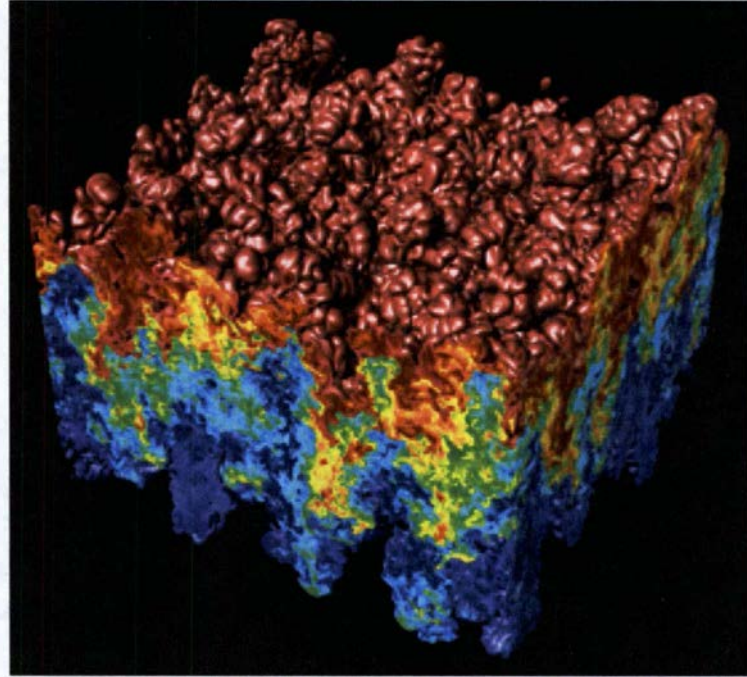


**Figure 5.** Density plot of the direct numerical simulation of a Rayleigh-Taylor mixing layer [25]. Red indicates the heavy fluid and blue indicates the light fluid.

We also can use the results of the 2-D linear stability analysis performed for Kelvin-Helmholtz instability above to examine the growth rate of the Rayleigh-Taylor mixing layer. If  $U_1 = U_2 = 0$ , the growth rate in Eqn. (1.5) reduces to,

$$s = \pm \left( g \tilde{k} \frac{\rho_2 - \rho_1}{\rho_2 + \rho_1} \right)^{1/2} = \pm (g \tilde{k} A)^{1/2}, \quad (1.6)$$

where  $A$  is the Atwood number given in Eqn. (1.2) above. For normal gravity,  $g$ , if  $\rho_1 < \rho_2$ , indicating the light fluid is atop the heavy fluid, then the growth rate,  $s$ , is a complex number and the configuration is stable. If a vertical downward acceleration can be applied, “reversing” gravity such that  $g < 0$ , then the growth rate is real and the

configuration is unstable.<sup>3</sup> This analysis can be extended to include surface tension and viscosity [26], as well as an initial density gradient [26, 27, 28].

### 2.2.3 Richtmyer-Meshkov

Perhaps the least understood and studied of the three instabilities presented here is the Richtmyer-Meshkov (RM) instability. The RM instability is shock- or impulse-driven and, like RT instabilities, it occurs due to a mismatch between the pressure and density gradients ( $\nabla p \bullet \nabla \rho < 0$ ). The instability forms when a shock is accelerated through the perturbed interface between two different density fluids (see Figures 6 and 7).

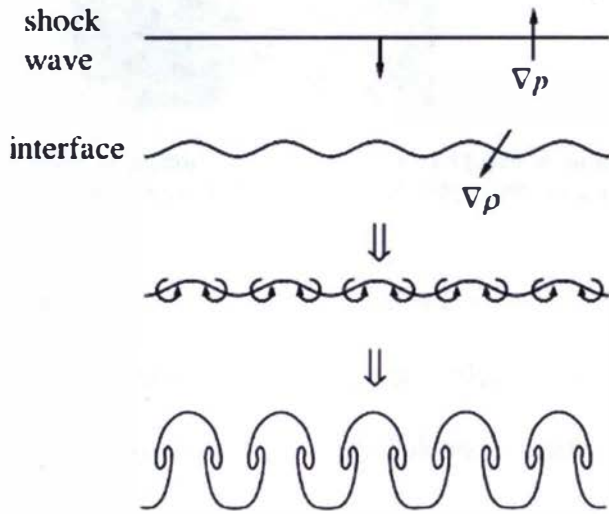


**Figure 6.** Pictorial of turbulence forming from a Richtmyer-Meshkov instability.

---

<sup>3</sup> In the results section, the “Rocket Rig” experiment [17] is presented demonstrating effects of transitioning from RT stable to unstable to stable again, albeit in a turbulent regime.

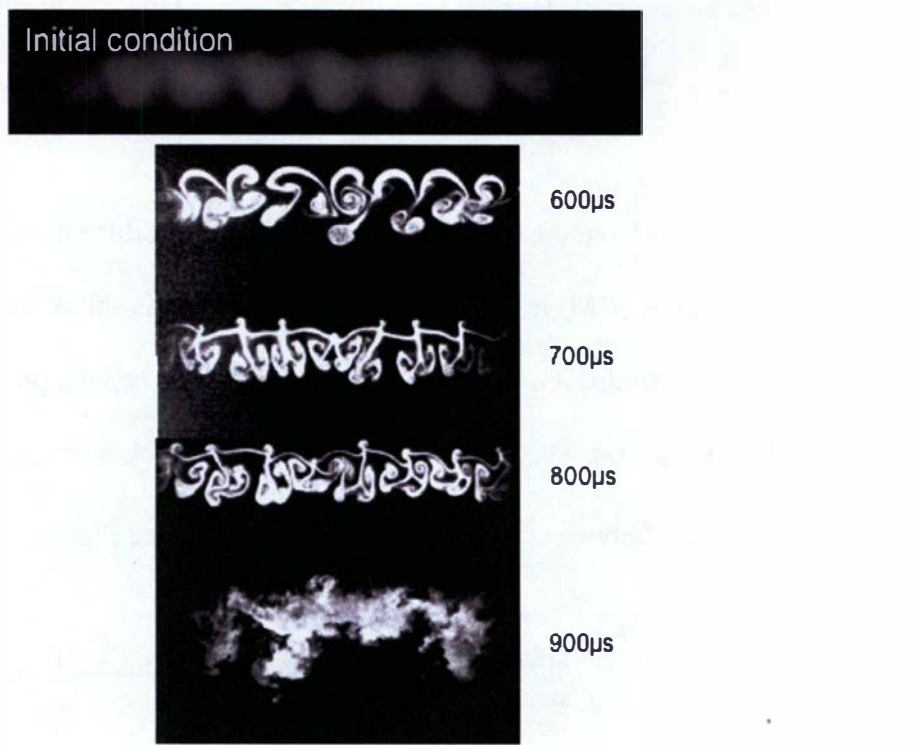


**Figure 7.** The evolution of shocked and reshocked gas curtain at initial time (picture enlarged), 600  $\mu$ s, 700  $\mu$ s, 800  $\mu$ s and 900  $\mu$ s [29]. Reproduced with permission of K. Prestridge.

Like Rayleigh-Taylor, the basic mechanism for the amplification of these perturbations is due to baroclinic generation of vorticity as the result of a pressure gradient-density gradient mismatch. As with RT, initial growth of the perturbations leads to the formation of bubbles and spikes. Unlike RT, the perturbations will grow regardless of the sign of  $\nabla p \bullet \nabla \rho$ . Unless more force is applied to continue to drive the turbulence, e.g., reshocking of the interface, the turbulence will decay away after some time. The width of the mixing layer may continue to increase due to latent turbulent transport effects. Modelling and simulation of RM turbulence will not be presented here, but it will be included in subsequent studies.

### **2.3 Methods for solving turbulent fluid flows: DNS, LES, RANS**

Although many variations have been developed, there are essentially three general approaches for solving a turbulent flow: direct numerical simulations (DNS), large eddy simulations (LES) and simulations solving the averaged Navier-Stokes equations (RANS). The latter can be performed using an ensemble-averaged (“multi-species”) approach or a volume-averaged (“multi-fluid”) approach<sup>4</sup>. DNS, LES and RANS are described briefly below. The three cases represent solutions that decrease in computational time, but increase in model complexity, respectively. In Figure 8, the pictures show calculated density results across a Rayleigh-Taylor mixing layer using the different approaches. On the left-hand side, one can see detailed features of the mixing fluids, discerning the shapes of the bubbles and spikes in the flow; the flow *looks* more complicated. For DNS, the conservation equations are solved for the full range of length and time scales, thus the equations are less complex but the simulations are computationally and, often prohibitively, expensive. The middle picture shows LES of the same flow, but for only the top half of the mixing layer. For the LES, in which the small-scale features of the flow field are filtered, we see only the larger-scale features of the flow. In this case, though the flow looks less complicated, the modelling makes the equations to be solved more complex. The LES are less computationally expensive than the DNS, though modelled equations for subgrid effects may be necessary. Finally, on the right-hand side of the figure, the density profile of a RANS simulation for the same flow is shown. Here, the flow variables are averaged across each plane slice of the mixing

---

<sup>4</sup> In the multi-species approach, a single conservation of mass, momentum and energy equation, combined with a multiple species conservation equation, is solved; for the multi-fluids approach, a conservation of mass, momentum and energy equation is solved for each fluid or species.

layer, creating the smooth profile. The averaging and additional modelling in the RANS equations make them the most complex, but they are the least computationally expensive.

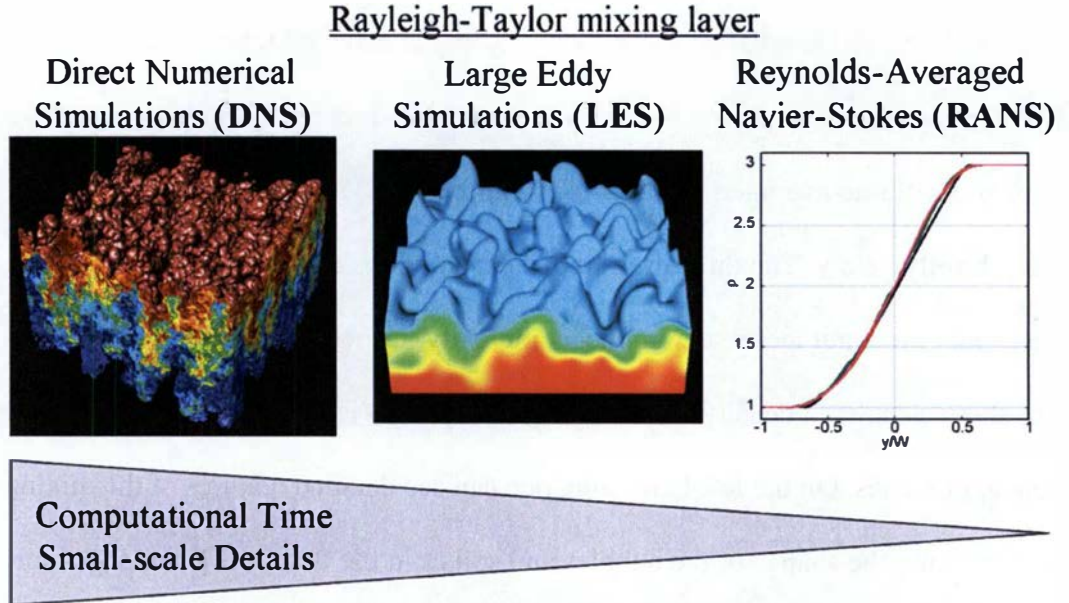


**Figure 8. Demonstration of differences in detail for Rayleigh-Taylor simulations using solution methods of various complexity and computational time [25, 30, 31].**

### 2.3.1 Direct numerical simulations (DNS)

A direct numerical simulation (DNS) is a calculation in computational fluid dynamics in which the Navier-Stokes equations are numerically solved without any turbulence modelling [32]. This means that the full range of spatial and temporal scales of the turbulence must be resolved. All the spatial scales of the turbulence must be resolved in the computational mesh, from the smallest dissipative scales (Kolmogorov microscales) to beyond the integral scale  $L$ , which is associated with the motions containing most of the kinetic energy. DNS is computationally expensive, and requires extensive time and resources. It is typically only used for solving the simplest of flows, e.g., see [25, 32, 33]. Note, for the purpose of model validation, we treat DNS results as data. Due to the vast scope of information that can be extracted from the DNS, it is used for deeper analysis of

the modelled terms in the BHR2 model. This approach to model analysis is one of the distinguishing characteristics of this work.

### 2.3.2 Large Eddy Simulations (LES)

A common deduction of Kolmogorov's famous theory of self-similarity [13] is large eddies of the flow are dependent on the flow geometry, while smaller eddies are self-similar and have a universal character. For this reason, it became a practice to solve only for the large eddies explicitly and model the effect of the smaller and more universal eddies on the larger ones. Thus, in LES the large-scale motions of the flow are calculated, while the effect of the smaller universal scales (the so called sub-grid scales) are modelled. As computer resources become more advanced, LES is also becoming more commonplace. In the validation of the BHR2 model through investigating RT, we do not use LES due to the availability of DNS data; however, in validation for Richtmyer-Meshkov flows, the intention is to include LES as “data”, in particular the work of Hill and Pullen [34].

### 2.3.3 Averaged Navier-Stokes

The last, and currently the most common, approach to simulating turbulent flows in miscible fluids is performed by solving for the *mean* motion of the flow. This is achieved by averaging the Navier-Stokes equations. As stated previously, the averaging can take the form of ensemble averaging or volume averaging, using a multi-species or a multi-fluid approach. Below, the ensemble multi-species RANS approach is presented. A more detailed derivation of the RANS equations can be found, e.g., in [35].

The issue of using either the multi-fluid or multi-species models for the class of experimental configurations examined here is an interesting question. Each turbulence

model has its own set of advantages and disadvantages, and the type of model used in evaluating a flow is determined by the intent of the user. For our purpose, the multi-species approach was chosen based on its ability to most easily capture the physics of turbulent *miscible* mixing layers. We simplify the evidence by noting that within the turbulence communities, outside of those involved with Rayleigh-Taylor or Richtmyer-Meshkov, the choice of model type has been obvious. For miscible mixing, the use of the multi-species approach dominates, as evidenced in the combustion community (see, e.g., [36]). In the two-phase flow arena, i.e., immiscible turbulent mixing, multi-fluid models primarily are used, e.g., see [37]. In [38], a comparison of the two approaches is presented and the manner in which various terms can be related from the two approaches is discussed.

As will be noted below, there are historical methods for solving the very general multi-species approach. We believe that ours, in some manner, currently represents the simplest, but still captures the physics of the flows of interest. More will be stated on this topic in the section on future directions.

In a nutshell, the method used in developing the BHR2 model can be described as,

1. Ensemble average the Navier-Stokes equations<sup>5</sup>.
2. Decide which terms to model explicitly, which terms to model phenomenologically and which to neglect.
3. Use experimental data to specify model coefficients.
4. Use additional experimental data to validate the choices made in the previous step.

---

<sup>5</sup> In this case, we are referring to conservation of mass, momentum and energy.

We begin with the equations governing fluid motion. The derivation of the Navier-Stokes equations can be found in any intermediate or advanced level fluid mechanics text, e.g., in [10]. Note, these descriptions typically will start with the Lagrangian conservation laws, e.g.,  $\mathbf{F} = m\mathbf{a}$ , and then convert them to an Eulerian framework. One also can start from the molecular viewpoint (Boltzman equations) and derive the same result [38, 39].

The conservation of mass is given by

$$\frac{\partial \rho}{\partial t} + \frac{\partial \rho u_n}{\partial x_n} = 0. \quad (1.7)$$

Conservation of momentum is

$$\frac{\partial \rho u_i}{\partial t} + \frac{\partial \rho u_i u_n}{\partial x_n} = \rho F_i + \frac{\partial \sigma_{in}}{\partial x_n}, \quad (1.8)$$

where

$$\sigma_{in} = -P\delta_{in} + \tau_{in}, \quad (1.9)$$

$F_i$  represents body forces, in this case gravity, and assuming a Newtonian fluid and neglecting bulk viscosity,

$$\tau_{in} = \mu \left( \frac{\partial u_i}{\partial x_n} + \frac{\partial u_n}{\partial x_i} - \frac{2}{3} \delta_{in} \frac{\partial u_j}{\partial x_j} \right). \quad (1.10)$$

The conservation of energy, assuming Fourier's law of heat transfer applies, is

$$\frac{\partial \rho I}{\partial t} + \frac{\partial \rho I u_n}{\partial x_n} = \tau_{in} \frac{\partial u_i}{\partial x_n} + \frac{\partial}{\partial x_n} \left( k \frac{\partial T}{\partial x_n} \right). \quad (1.11)$$

Assuming Fickian diffusion, the conservation of species is

$$\frac{\partial \rho c^k}{\partial t} + \frac{\partial \rho c^k u_n}{\partial x_n} = \frac{\partial}{\partial x_n} \left( \rho D \frac{\partial c^k}{\partial x_n} \right). \quad (1.12)$$

See the Nomenclature section for a description of all the variables, but keep in mind that each variable presented is a function of both space and time. These are the equations typically used in DNS.

In order to calculate turbulent flows, the fluid equations are reformulated to solve for averaged quantities. After the averaging process has been performed, the solution to the new system of equations gives the mean values of the variables. This method of averaging and solving for mean quantities has been an integral part of solving for turbulent flows for many decades, e.g., see [38, 40].

Ensemble averaging refers to averaging performed over many experiments to obtain mean values. Ensemble averaging can be equated to time and space averages through the ergodic hypothesis [41]. Note, the averaging process used for reporting the data from experiments we show later in the Results section ranges from time averaging for the gas channel experiments [42] to space averaging in the DNS results [25].

The instantaneous value can be defined as

$$X = \bar{X} + X', \quad (1.13)$$

where  $X$  represents any dynamic or thermodynamic variable and for which the bar denotes the uniformly weighted ensemble averaged component of the variable and the prime indicates the fluctuating component.

A combination of uniformly weighted averaging (Reynolds decomposition), as shown above, and mass weighted averaging (Favre decomposition), given by

$$X = \tilde{X} + X'', \quad (1.14)$$

in which

$$\tilde{X} = \frac{\overline{\rho X}}{\overline{\rho}}, \quad (1.15)$$

is performed on the Navier-Stokes equations. For the Favre averaging, the tilda indicates the mass-weighted component of the variable and the double prime denotes the mass-weighted fluctuation about  $\bar{x}$ . This averaging procedure is described in more detail, e.g., in [35, 38, 39].

The RANS equations produced from the averaging process and corresponding to Eqns. (1.7)-(1.12) become [38],

$$\frac{\partial \bar{\rho}}{\partial t} + \frac{\partial \bar{\rho} \tilde{u}_n}{\partial x_n} = 0, \quad (1.16)$$

$$\frac{\partial \bar{\rho} \tilde{u}_i}{\partial t} + \frac{\partial \bar{\rho} \tilde{u}_i \tilde{u}_n}{\partial x_n} = - \frac{\partial \bar{p}}{\partial x_n} + \frac{\partial}{\partial x_n} \left( \bar{\tau}_{in} - \overline{\rho u_i' u_n''} \right) + \bar{\rho} g_i, \quad (1.17)$$

where

$$\bar{\tau}_{in} = \mu \left( \frac{\partial \tilde{u}_i}{\partial x_n} + \frac{\partial \tilde{u}_n}{\partial x_i} - \frac{2}{3} \delta_{in} \frac{\partial \tilde{u}_j}{\partial x_j} \right) + \mu \left( \frac{\partial \bar{u}_i''}{\partial x_n} + \frac{\partial \bar{u}_n''}{\partial x_i} - \frac{2}{3} \delta_{in} \frac{\partial \bar{u}_j''}{\partial x_j} \right), \quad (1.18)$$

$$\begin{aligned} \frac{\partial \bar{\rho} \tilde{I}}{\partial t} + \frac{\partial \bar{\rho} \tilde{I} \tilde{u}_n}{\partial x_n} &= \bar{p} \frac{\partial}{\partial x_n} \left( \tilde{u}_n - \bar{u}_n'' \right) - \overline{p' \frac{\partial u_n'}{\partial x_n}} + \bar{\tau}_{nm} \frac{\partial \tilde{u}_n}{\partial x_m}, \\ &\quad + \overline{\tau'_{nm} \frac{\partial u_n'}{\partial x_m}} + \frac{\partial}{\partial x_n} \left( \kappa \frac{\partial \bar{T}}{\partial x_n} \right) - \frac{\partial}{\partial x_n} \overline{\rho I'' u_n''} \end{aligned} \quad (1.19)$$

and

$$\frac{\partial \bar{\rho} \tilde{c}^k}{\partial t} + \frac{\partial \bar{\rho} \tilde{c}^k \tilde{u}_n}{\partial x_n} = \frac{\partial}{\partial x_n} \left( \bar{\rho} D \frac{\partial \tilde{c}^k}{\partial x_n} \right) - \frac{\partial}{\partial x_n} \overline{\rho u_n'' c^{k''}} + \frac{\partial}{\partial x_n} \overline{\rho D \frac{\partial}{\partial x_n} c^{k''}}. \quad (1.20)$$

This leads to more unknowns than equations. Some of the higher order correlation terms are assumed negligible, while others must be modelled in order to close the system of equations.

If we assume that the transport of mass, momentum and energy due to molecular effects are small on average compared to turbulence effects, then the above equations reduce to:

$$\frac{\partial \bar{\rho}}{\partial t} + \frac{\partial \bar{\rho} \tilde{u}_n}{\partial x_n} = 0, \quad (1.21)$$

$$\frac{\partial \bar{\rho} \tilde{u}_i}{\partial t} + \frac{\partial \bar{\rho} \tilde{u}_i \tilde{u}_n}{\partial x_n} = -\frac{\partial \bar{p}}{\partial x_n} + \frac{\partial}{\partial x_n} \left( -\overline{\rho u_i'' u_n''} \right) + \bar{\rho}_i g_i, \quad (1.22)$$

$$\frac{\partial \bar{\rho} \tilde{I}}{\partial t} + \frac{\partial \bar{\rho} \tilde{I} \tilde{u}_n}{\partial x_n} = \bar{p} \frac{\partial}{\partial x_n} \left( \tilde{u}_n - \overline{u_n''} \right) - \frac{\partial}{\partial x_n} \overline{\rho I'' u_n''}, \quad (1.23)$$

and

$$\frac{\partial \bar{\rho} \tilde{c}^k}{\partial t} + \frac{\partial \bar{\rho} \tilde{c}^k \tilde{u}_n}{\partial x_n} = -\frac{\partial}{\partial x_n} \overline{\rho u_n'' c^{k''}}. \quad (1.24)$$

The terms requiring a phenomenological model are then the apparent stress or Reynolds stress tensor,

$$R_{in} = -\overline{\rho u_i'' u_n''}, \quad (1.25)$$

the species mass flux, or “drift”, velocity,

$$a_i^k = -\overline{\rho u_i'' c^{k''}}, \quad (1.26)$$

and the turbulent flux of the internal energy, sometimes called the turbulent “heat flux”,

$$S_n = -\overline{\rho I'' u_n''}. \quad (1.27)$$

These terms are described in more detail in the following section.

### **3. The BHR2 turbulence model**

BHR2 is a multi-species turbulence model developed to address the physics of multi-material (variable-density) compressible turbulent flows in miscible fluids and used to close the set of equations for the Reynolds stress, the species flux and the turbulent flux of the internal energy.<sup>6</sup> The basic formulation was first published in 1993 in [38], but extensive validation across a variety of experiments has been performed only recently. Our current BHR2 formulation still contains some simplification from this original work, namely, we use an algebraic closure for the Reynolds stress and a gradient approximation for the turbulent heat flux. Other models have been developed to address the same physics issues prior to and following the first publication of BHR in 1993. As the BHR2 model is discussed below, models of historical interest will be briefly presented where they are relevant.

On a side note, one of the many applications that will not be presented in the historical details is the modelling of compressible single-phase turbulence. In this type of flow, density variations are created typically by shocking the material. An excellent reference for this class of flows is readily available in [14]. Many of the modelling issues of compressible single-phase turbulence are relevant to the study of multi-material mixing and, thus, they are of interest to our specific thrust of research.

#### ***3.1 Unmodelled and modelled equations***

In the following sections, we present the unmodelled form of the equations and introduce the current modelled form. The first variable to be considered is the evolution of the

---

<sup>6</sup> The constraint of miscibility is sometimes removed in certain experimental configurations but the overall intent remains.

Reynolds stress term followed by a brief discussion of the turbulent flux of the internal energy and the species mass flux.

### 3.1.1 Reynolds stress model

As discussed earlier, the derivation of the averaged Navier-Stokes equations leads to new terms, which must be modelled. These include an apparent Reynolds stress tensor,

$$R_{in} = -\overline{\rho u_i' u_n''}. \quad (1.28)$$

Here, we introduce the unmodelled evolution of the Reynolds stress followed by the model used in RAGE. An evolution equation for the Reynolds stress tensor can be derived from conservation of momentum and is given as,

$$\begin{aligned} \frac{\partial R_{ij}}{\partial t} + \frac{\partial R_{ij}\tilde{u}_n}{\partial x_n} &= -\frac{\partial R_{nij}}{\partial x_n} - R_{in} \frac{\partial \tilde{u}_j}{\partial x_n} - R_{jn} \frac{\partial \tilde{u}_i}{\partial x_n} \\ &+ \sum \left\{ \left( \frac{\partial \bar{P}}{\partial x_j} - \frac{\partial}{\partial x_n} \bar{\tau}_{nj} \right) - \frac{\partial}{\partial x_n} \overline{u' \left( \delta_{nj} P' - \tau'_{nj} \right)} + \overline{P' \frac{\partial u'_i}{\partial x_j}} - \overline{\frac{\partial u'_i}{\partial x_n} \tau'_{nj}} \right\}. \end{aligned} \quad (1.29)$$

The manner in which the Reynolds stress is actually evaluated varies widely in the literature and modelling the full evolution is part of our future efforts [43]. Historically, the Boussinesq approximation [11] for single phase flows has been used as a standard method to model the Reynolds stress. This method constitutes what we refer to as “BHR” or sometimes “BHR1” and is described in [42]. One of the more recent works by Dimonte and Tipton [44] uses the heuristic,  $R_{ij} = C_p \delta_{ij} \rho K$ , but this model suffers from the inability to capture shear flows. Gregoire et al. [45] used the full Reynolds stress evolution for modelling of RM flows. A middle path was chosen for our current turbulence model. The Ristorcelli approximation [46] gives an algebraic form for  $R_{ij}$ ,

which is both realizable and valid for variable-density flows. This model is given as follows,

$$R_{ij} = 2 / 3 \bar{\rho} K \delta_{ij} - \frac{4}{3} \bar{\rho} K \frac{C_s}{R} S_{ij} - 2 \bar{\rho} K \frac{C_A}{R} A_{ij}, \quad (1.30)$$

where

$$S_{ij} = \frac{1}{2} \frac{S}{\sqrt{K}} \left[ \tilde{U}_{i,j} + \tilde{U}_{j,i} - \frac{2}{3} \tilde{U}_{k,k} \delta_{ij} \right] \quad (1.31)$$

and

$$A_{ij} = \frac{S}{2 \bar{\rho} K^{3/2}} \left[ a_i \frac{\partial P}{\partial x_j} + a_j \frac{\partial P}{\partial x_i} - \frac{2}{3} a_k \frac{\partial P}{\partial x_k} \delta_{ij} \right]. \quad (1.32)$$

Note, if  $C_A = 0$  and  $R = 1$ , the equation reduces to the standard Boussinesq approximation. Otherwise,

$$\begin{aligned} R = & \frac{1}{2} \left( |A| - 1 + \frac{1}{2} C^{\text{newp}} + C_s |S_1| \right) + \frac{1}{4} \left\{ \left( |A| - 1 + \frac{1}{2} C^{\text{newp}} + C_s |S_1| \right)^2 \right. \\ & \left. + 2 \left[ \frac{2}{3} C_s S^2 - C_A AS + \frac{C_s S_1}{2} \left( A - 1 + \frac{1}{2} C^{\text{newp}} \right) \right] \right\}^{1/2}, \end{aligned} \quad (1.33)$$

where

$$A = \frac{S a_k \frac{\partial P}{\partial x_k}}{\bar{\rho} K^{3/2}}, \quad (1.34)$$

$$AS = A_{ij} S_{ij}, \quad (1.35)$$

$$S^2 = S_{ij} S_{ij}, \quad (1.36)$$

and

$$S_1 = \text{sign} [S_{nn,\max}] \sqrt{\frac{2}{3}} S^2. \quad (1.37)$$

To maintain the historical nomenclature of this Reynolds stress model,  $AS$  and  $S^2$  are defined as shown above. This is the only section of this report that uses these definitions. Everywhere else  $S$  represents the turbulent length scale and  $A$  represents the Atwood number as they were defined earlier in the report.

Returning to the Reynolds stress approximation,  $C_s$  and  $C_A$  are model coefficients to be determined empirically. The variable  $C^{nexp} = 2 + 1.6F^{nexp}$ , in which  $nexp$  is a model coefficient and

$$F = 1 - \frac{a}{2} b_{kk}^2 + \frac{27}{3} b_{kk}^3, \quad (1.38)$$

where

$$b_{kk}^2 = b_{nk} b_{kn}, \quad (1.39)$$

$$b_{kk}^3 = b_{nk} b_{kn}^2 \quad (1.40)$$

and

$$b_{ij} = \frac{R_{ij}}{R_{nn}} - \frac{1}{3} \delta_{ij}. \quad (1.41)$$

This last term is the Reynolds stress anisotropy tensor.

This Boussinesq-like model now takes into account the principal production terms of  $K$  in variable-density flows, namely,  $\partial P / \partial x_n$ . Unfortunately, the numerical implementation of the term containing  $C_A$  leads to instabilities in the results of some flows at very late times. Two of the key constraints on our modelling efforts are robustness and stability; therefore, with some exceptions,  $C_A$  was set to zero for the majority of this study. It is hoped that future research will lessen or eliminate this problem. In the meantime, because the issue has only been observed at late times and at

high resolutions, users may choose to set the model coefficient,  $C_A$ , to its specified value of 0.5.

For calculation of the Reynolds stress in Eqn. (1.30), in addition to the mean velocity and pressure gradients, values for the turbulent kinetic energy,  $K$ , and the mass flux velocity,  $\mathbf{a}$ , are required. Modelling of these terms is presented after introducing closures for the turbulent fluxes of species and internal energy.

### 3.1.2 Turbulent flux of internal energy

Next, the method for evaluating the turbulent flux of the internal energy,  $S_i$ , is given. This term is defined as,

$$S_i = -\overline{\rho I'' u_i''}. \quad (1.42)$$

An evolution equation can be derived from the internal energy, momentum and mass equations. In [38] it is given as,

$$\begin{aligned} \frac{\partial S_i}{\partial t} + \frac{\partial S_i \tilde{u}_n}{\partial x_n} = & -R_{in} \frac{\partial \tilde{I}}{\partial x_n} - S_n \frac{\partial \tilde{u}_i}{\partial x_n} - \frac{\partial}{\partial x_n} \overline{\rho u_n'' u_i'' T''} - \overline{I''} \frac{\partial \bar{\sigma}_{ni}}{\partial x_n} + \left( a_i \bar{\sigma}_{nm} - \overline{u_i' \sigma_{nm}} \right) \frac{\partial \bar{u}_m}{\partial x_n} \\ & + \overline{\frac{\partial \sigma'_{ni}}{\partial x_n} I'} - a_i \bar{\rho} \epsilon + \overline{u_i' \frac{\partial u_n'}{\partial x_m} \tau_{nm}} - a_i \frac{\partial}{\partial x_n} \left( \kappa \frac{\partial \bar{T}}{\partial x_n} \right) - \overline{u_i' \frac{\partial}{\partial x_n} \left( \kappa \frac{\partial T'}{\partial x_n} \right)}. \end{aligned} \quad (1.43)$$

We have little experience with this equation and  $S_i$  is modelled simply as a gradient diffusion process in the energy equation:

$$\frac{\partial \left( -\overline{\rho I'' u_i''} \right)}{\partial x_n} = \frac{\partial}{\partial x_n} \left( \frac{\bar{\rho} v_t}{\sigma_{SIE}} \frac{\partial \bar{I}}{\partial x_n} \right), \quad (1.44)$$

in which  $v_t = C_\mu S \sqrt{K}$ . The gradient diffusion approximation is discussed in detail in a later section. Future work is planned to explore the differences between the use of a

gradient approximation and a full evolution equation. No known references that model the full equation are available.

### 3.1.3 Turbulence mass flux

The last quantity required from the ensemble averaging process of the Navier-Stokes equations is the turbulence species mass flux,

$$a_i^k = -\overline{\rho u_i'' c^{k''}}. \quad (1.45)$$

An evolution equation has been derived from the momentum and mass equations. In an undocumented report by [47], the evolution of the turbulent species mass flux is given as,

$$\frac{\partial \bar{\rho} a_i^k}{\partial t} + \frac{\partial \bar{\rho} a_i^k \tilde{u}_n}{\partial x_n} = R_{in} \frac{\partial \tilde{c}^k}{\partial x_n} - a_n^k \frac{\partial \tilde{u}_i}{\partial x_n} + \overline{\frac{\partial \rho u_i'' u_i'' c^{k''}}{\partial x_n}} - b^k \frac{\partial \bar{\sigma}_{in}}{\partial x_n} - c^{k''} \frac{\partial \bar{\sigma}'_{in}}{\partial x_n} - \overline{u_i'' D^{k'}}, \quad (1.46)$$

where

$$a_i = \sum_k \frac{a_i''}{\rho^k} = \frac{\overline{\rho' u'}}{\bar{\rho}}.$$

We also have had little experience with this equation, and it is modelled simply as a gradient diffusion process in the same manner as the turbulent energy flux equation:

$$\frac{\partial \left( \overline{\rho u_i'' c^{k''}} \right)}{\partial x_n} = \frac{\partial}{\partial x_n} \left( \frac{\bar{\rho} v_t}{\sigma_c} \frac{\partial \tilde{c}^k}{\partial x_n} \right) \quad (1.47)$$

Substituting Eqn. (1.47) into Eqn. (1.24) gives the modelled evolution equation for the transport of species as,

$$\frac{\partial \bar{\rho} \tilde{c}^k}{\partial t} + \frac{\partial \bar{\rho} \tilde{c}^k \tilde{u}_n}{\partial x_n} = \frac{\partial}{\partial x_n} \left( \frac{\bar{\rho} v_t}{\sigma_c} \frac{\partial \tilde{c}^k}{\partial x_n} \right). \quad (1.48)$$

As with the internal energy equation, a turbulent viscosity is needed. A modelled form of equation (1.46) has been implemented and awaits validation.

From the algebraic closure of the Reynolds stress and the gradient diffusion approximations for the turbulent heat flux and the turbulent species mass flux, evolution equations for the turbulence kinetic energy,  $K$ , the turbulence mass flux velocity,  $\mathbf{a}$ , the turbulence length scale,  $S$ , and, although not yet evident, the density-specific volume correlation,  $b$ , are required for the BHR2 model. The dependence of the variable  $b$  will be demonstrated below, and is the focus of this report. The evolution equations for  $K$ ,  $\mathbf{a}$ , and  $b$  can be derived from the conservation of mass and momentum equations (see [38] for details). The equation for  $S$  is developed analogous to the  $K$  equation, with the assumption that the production and dissipation of  $K$  and  $S$  are proportional.

In general, for a single-phase incompressible fluid, there is a need for  $K \sim \overline{u'u'}$  using this kind of closure method. For the case of variable-density fluids, the density fluctuation also needs modelling and, thus, some form of  $\overline{\rho'u'}$  and  $\overline{\rho'\rho'}$  are needed. We chose  $\overline{\rho'(1/\rho')}$  due to its natural occurrence in the  $\mathbf{a}$  equation. See Gregoire et al. [45] for a different approach.

### 3.1.4 Turbulence kinetic energy

As presented earlier, the turbulence kinetic energy is defined as half the trace of the Reynolds stress tensor:

$$K = \frac{R_{nn}}{2\bar{\rho}} = \frac{\overline{\rho u_n'' u_n''}}{2\bar{\rho}}. \quad (1.49)$$

It gives the mean kinetic energy of the fluctuating velocity field, i.e., the mean energy in the velocity fluctuations that occur due to turbulence. An evolution equation for the

turbulence kinetic energy is derived directly from conservation of mass and momentum [14, 38] and the formulation we use is given as,

$$\frac{\partial \bar{P} K}{\partial t} + \frac{\partial \bar{P} K \tilde{u}_n}{\partial x_n} = a_n \underbrace{\left( \frac{\partial \bar{P}}{\partial x_n} - \frac{\partial \bar{\tau}_{in}}{\partial x_n} \right)}_{\text{buoyancy production}} - R_{in} \underbrace{\frac{\partial \tilde{u}_i}{\partial x_n}}_{\text{shear production}} - \underbrace{\frac{1}{2} \frac{\partial}{\partial x_n} (\rho \tilde{u}_i \tilde{u}_i' \tilde{u}_n'')}_{\text{turbulent transport (diffusion)}} \\ - \underbrace{\frac{\partial \overline{P' u'_i}}{\partial x_i}}_{\text{power of fluctuating pressure in fluctuating motions}} + \underbrace{\overline{P' \frac{\partial u'_i}{\partial x_i}}}_{\text{pressure-dilatation correlation}} - \underbrace{\overline{\tau'_{in} \frac{\partial u'_i}{\partial x_i}}}_{\substack{\text{turbulent dissipation} \\ \text{Should be } x_k}} + \underbrace{\frac{\partial \overline{\tau'_{in} u'_i}}{\partial x_n}}_{\substack{\text{power of fluctuating viscous forces in} \\ \text{fluctuating motion} \\ (\text{viscous diffusion})}}, \quad (1.50)$$

where, again,  $a_n$  is the mass flux velocity and  $R_{in}$  is the Reynolds stress tensor. We have labelled the physical effects of the components, if they are known [14, 48].

If one desired, each new term that is created by deriving the evolution equations shown above also can be derived. This leads to a perpetuating effect in which more new terms are created and closing the system of equations without a model is unlikely. In BHR2, the major production terms in Eqn. (1.50) are solved exactly, while the remaining terms are either neglected or modelled as diffusion and dissipation.

The commonly used gradient diffusion hypothesis [9, 14] is applied to the turbulent transport terms such that,

$$\frac{\partial}{\partial x} (\overline{u' X'}) \approx \frac{\partial}{\partial x} \left( \frac{\rho v_t}{\sigma} \frac{\partial \bar{X}}{\partial x} \right), \quad (1.51)$$

where  $\bar{X}$  is the turbulent transport term of interest. The dissipation terms are modelled as a function of the turbulent time scale such that,

$$\text{dissipation} \propto X \tau_t = X \frac{\sqrt{K}}{S}, \quad (1.52)$$

where  $\tau_t = \sqrt{K} / S$ .

Note, the terms “diffusion” and “transport” often are used interchangeably.

Diffusion is in reference to the type of modelling used – the model *behaves* like a molecular diffusion process (see [9]). However, the process does not occur due to molecular diffusion, but rather “transport” of properties by the large-scale structures.

Additionally, the terms “dissipation”, “decay” and “drag” frequently are used to discuss similar behaviour. Dissipation refers to the modelling of the transfer down the energy spectrum. Decay is the end result of this process. Drag is in reference to the drag term seen in buoyancy-drag models [44]. In BHR2, the dissipation acts like the drag term in buoyancy-drag models. The use of this term makes some sense in describing the dissipation of  $a$ , but not so much for  $K$  and certainly not for  $b$ .

With these two simple expressions in Eqns. (1.51) and (1.52), we model the turbulent transport (diffusion) as,

$$-\frac{1}{2} \frac{\partial}{\partial x_n} (\rho u_i' u_i' u_n'') = \frac{\partial}{\partial x_n} \left( \frac{\rho v_t}{\sigma_k} \frac{\partial K}{\partial x_n} \right), \quad (1.53)$$

and dissipation as,

$$\overline{\tau_{in}' \frac{\partial u_i'}{\partial x_i}} = \varepsilon \equiv \frac{K^{3/2}}{S}. \quad (1.54)$$

The expression  $\varepsilon \equiv K^{3/2} / S$  for the dissipation comes from the definition of the length scale,  $S$ .

The three terms not yet mentioned, the power of the fluctuating pressure and viscous forces and the pressure-dilation correlation, are neglected using scale analysis as in [50], i.e.,

$$\frac{\partial \overline{P' u'_i}}{\partial x_i} \sim 0, \quad \overline{P' \frac{\partial u'_i}{\partial x_i}} \sim 0 \quad \text{and} \quad \frac{\partial \overline{\tau_{in}' u'_i}}{\partial x_n} \sim 0.$$

Additionally, because viscous effects are much smaller than pressure effects, the shear

term,  $-a_n \frac{\partial \bar{\tau}_{in}}{\partial x_n}$ , which contributes to buoyancy production, is neglected. The above

procedure is used throughout and is validated mainly through term-by-term comparison with results from DNS.

Finally, the modelled equation becomes,

$$\frac{\partial \bar{\rho} K}{\partial t} + \frac{\partial \bar{\rho} K \tilde{u}_n}{\partial x_n} = a_n \frac{\partial \bar{P}}{\partial x_n} - R_{in} \frac{\partial \tilde{u}_i}{\partial x_n} + \frac{\partial}{\partial x_n} \left( \frac{\bar{\rho} v_t}{\sigma_k} \frac{\partial K}{\partial x_n} \right) - \bar{\rho} \frac{K^{3/2}}{S}, \quad (1.55)$$

where  $v_t = C_\mu S \sqrt{K}$  is the “turbulent viscosity”,  $C_\mu$  and  $\sigma_k$  are model coefficients and  $S$  is the turbulence length scale.

### 3.1.5 Turbulence mass flux velocity

The turbulence mass flux is the mean of the fluctuation of the Favre-averaged velocity:

$$a_i = \frac{\overline{\rho' u'_i}}{\bar{\rho}} = -\overline{u''_i}. \quad (1.56)$$

In addition to its role in the energy equation, the mass flux velocity drives the principal buoyancy production of the turbulent kinetic energy, as seen in Eqn. (1.55).

The evolution equation for the mass flux velocity also is derived from conservation of mass and momentum (see [14] and [38]). This gives,

$$\begin{aligned} \frac{\partial \bar{\rho} a_i}{\partial t} + \underbrace{\frac{\partial \bar{\rho} a_i \tilde{u}_n}{\partial x_n}}_{\text{advection}} &= -\bar{\rho} a_n \underbrace{\left( \frac{\partial \tilde{u}_i - a_i}{\partial x_n} \right)}_{\text{production}} + \underbrace{\left( \frac{\overline{\rho' u'_i u'_n} - R_{in}}{\bar{\rho}} \right)}_{\text{production}} \frac{\partial \bar{\rho}}{\partial x_n} + \underbrace{\bar{\rho} \frac{\partial a_i a_n}{\partial x_n}}_{\text{transport?}} - \underbrace{\bar{\rho} u'_i \frac{\partial u'_n}{\partial x_n}}_{\text{diffusion?}} - \underbrace{\frac{\partial \overline{\rho' u'_i u'_n}}{\partial x_n}}_{\text{diffusion?}} \\ &\quad + b \underbrace{\left( \frac{\partial \bar{P}}{\partial x_i} - \frac{\partial \bar{\tau}_{in}}{\partial x_n} \right)}_{\text{buoyancy production}} + \underbrace{\bar{\rho} \left( \frac{1}{\bar{\rho}} \right)' \frac{\partial P'}{\partial x_i} - \bar{\rho} \left( \frac{1}{\bar{\rho}} \right)' \frac{\partial \tau'_{in}}{\partial x_n}}_{\text{destruction/dissipation}}, \end{aligned} \quad (1.57)$$

where  $b = -\overline{\rho'(1/\rho)'}'$ , i.e., the “density-specific volume correlation.” We see in Eqn. (1.57) the dependence of buoyancy production on  $b$ , similar to the relationship of  $\mathbf{a}$  to the production in  $K$  in Eqn. (1.50), and thus the need for modelling  $b$  as described earlier.

As seen in Eqn. (1.50), the mass flux velocity drives the principal production term due to buoyancy in the evolution of the turbulence kinetic energy. It must be modelled accurately in order to produce the right value of  $K$  for the right reasons. The first models specifically aimed at buoyancy effects in variable-density flows were principally applied to combustion problems. These early modelling approaches used the gradient transport approximation for the turbulent mass flux velocity vector,  $\mathbf{a}$ :

$$\overline{\rho'u'} = v_t \frac{\partial \rho}{\partial y}. \quad (1.58)$$

To the best of our knowledge, the earliest use of this approximation for either RT or RM turbulence is in the dissertation of Andrews [24] and even earlier in the combustion community, 1977 [51]. Extensive experiments throughout the 1980s showed that this approximation was not valid in many cases, including premixed flames and many regions of non-reactive binary jets. See [14] and [36] for a more complete discussion of its limitations. Still, the use of the gradient approximation continues, although in limited flow regimes [44,52].

Perhaps the first to realize the limitations of the gradient diffusion approximation and, therefore, the need for an evolution of the turbulence mass flux was [53]. The modelled forms for either the mass flux velocity,  $\mathbf{a}$ , or in combustion the  $\rho'T'$  term, share a similar form to the BHR2 model presented in this report (see [45, 54]). However, some

details are different, including potential variations in the exact form of the unmodelled equation for  $\mathbf{a}$ . Although the evolution of the turbulence mass flux has been used in the combustion community since 1979, to the best of our knowledge, it has only recently been used in other fields. We believe our group at Los Alamos National Laboratory is the first to apply this method to Rayleigh-Taylor flows and Gregoire et al. [45] has recently used the evolution of the mass flux for Richtmyer-Meshkov flows.

As with the evolution of turbulence kinetic energy, for the evolution of the mass flux velocity in BHR2, the exact production terms are maintained while the remaining terms are neglected or modelled as diffusion and dissipation. This gives transport (diffusion) and dissipation as,

$$-\frac{\partial \overline{\rho' u'_i u'_n}}{\partial x_n} = \frac{\partial}{\partial x_n} \left( \frac{v_t}{\bar{\rho} \sigma_a} \frac{\partial a_i}{\partial x_n} \right) \quad (1.59)$$

and

$$\overline{\bar{\rho} \left( \frac{1}{\rho} \right)' \frac{\partial \tau'_{in}}{\partial x_n}} = C_{al} \bar{\rho} a_i \frac{K^{1/2}}{S}, \quad (1.60)$$

respectively. Again, the shear portion of the buoyancy production is neglected,

$$-b \frac{\partial \bar{\tau}_{in}}{\partial x_n} \sim 0,$$

as well as,

$$\overline{\bar{\rho} u'_i \frac{\partial u'_n}{\partial x_n}} \sim 0 \text{ and } \overline{\bar{\rho} \left( \frac{1}{\rho} \right)' \frac{\partial P'}{\partial x_i}} \sim 0.$$

Because  $R_{in} \gg \overline{\rho' u'_i u'_n}$ , the  $\overline{\rho' u'_i u'_n} / \bar{\rho}$  production term is also neglected. Finally, this gives the following equation for  $\mathbf{a}$ :

$$\begin{aligned} \frac{\partial \bar{\rho} a_i}{\partial t} + \frac{\partial \bar{\rho} a_i \tilde{u}_n}{\partial x_n} &= b \frac{\partial \bar{P}}{\partial x_n} - \frac{R_{in}}{\bar{\rho}} \frac{\partial \bar{\rho}}{\partial x_n} - \bar{\rho} a_n \frac{\partial (\tilde{u}_i - a_i)}{\partial x_n} + \bar{\rho} \frac{\partial a_i a_n}{\partial x_n} \\ &+ \frac{\partial}{\partial x_n} \left( \frac{v_t}{\bar{\rho} \sigma_a} \frac{\partial a_i}{\partial x_n} \right) - C_{al} \bar{\rho} a_i \frac{K^{1/2}}{S}, \end{aligned} \quad (1.61)$$

in which  $C_{al}$  and  $\sigma_a$  are model coefficients.

### 3.1.6 Density-specific volume correlation

By definition, the density-specific volume correlation,  $b$ , is the mean of the product of density and specific volume fluctuations,

$$b = -\overline{\rho' \left( \frac{1}{\rho} \right)'} = -\overline{\rho' v'}. \quad (1.62)$$

It is a principal driver for the production of  $\mathbf{a}$ , and it is useful to think of it as a measure of the degree of mix in a multi-fluid system. An evolution equation for  $b$  can be derived directly from the continuity equation, as demonstrated in [38]. The form of the  $b$  equation given by [38] was reformulated by R. Ristorcelli [55] to give,

$$\frac{\partial \bar{\rho} b}{\partial t} + \underbrace{\frac{\partial \bar{\rho} b \tilde{u}_n}{\partial x_n}}_{\text{advection}} = \underbrace{2 \bar{\rho} a_n \frac{\partial b}{\partial x_n}}_{\text{production}} - \underbrace{2(b+1)a_n \frac{\partial \bar{\rho}}{\partial x_n}}_{\text{production}} + \bar{\rho} \frac{\partial}{\partial x_n} \underbrace{\left[ \frac{\rho' \left( \frac{1}{\rho} \right)' u_n'}{\bar{\rho}} \right]}_{\text{turbulent transport (diffusion)}} + \underbrace{2 \bar{\rho} \left( \frac{1}{\rho} \right)' \frac{\partial u_n'}{\partial x_n}}_{\text{destruction/dissipation}}. \quad (1.63)$$

To provide the reader with a more physical feel for  $b$ , consider the pictures in Figure 9. In the figure,  $\rho_1$  and  $\rho_2$  are the densities of two fluids and  $c_1$  and  $c_2$  are the corresponding species concentrations. Note, these pictures are meant to be a representation of sub-grid turbulence dynamics. In Figure 9(a), there are two fluids of

different densities with a completely atomically diffuse interface between them. For demonstration purposes, the following discussion is presented in terms of planar averaging, but recall that this can be related to ensemble averaging through the ergodic hypothesis. Continuing, if planar averaging (blue dashed lines) is performed parallel to the interface, because there are no density fluctuations along an individual plane, the value of  $b$  is zero. In other words, everywhere along a plane, the fluids are one hundred percent molecularly mixed.

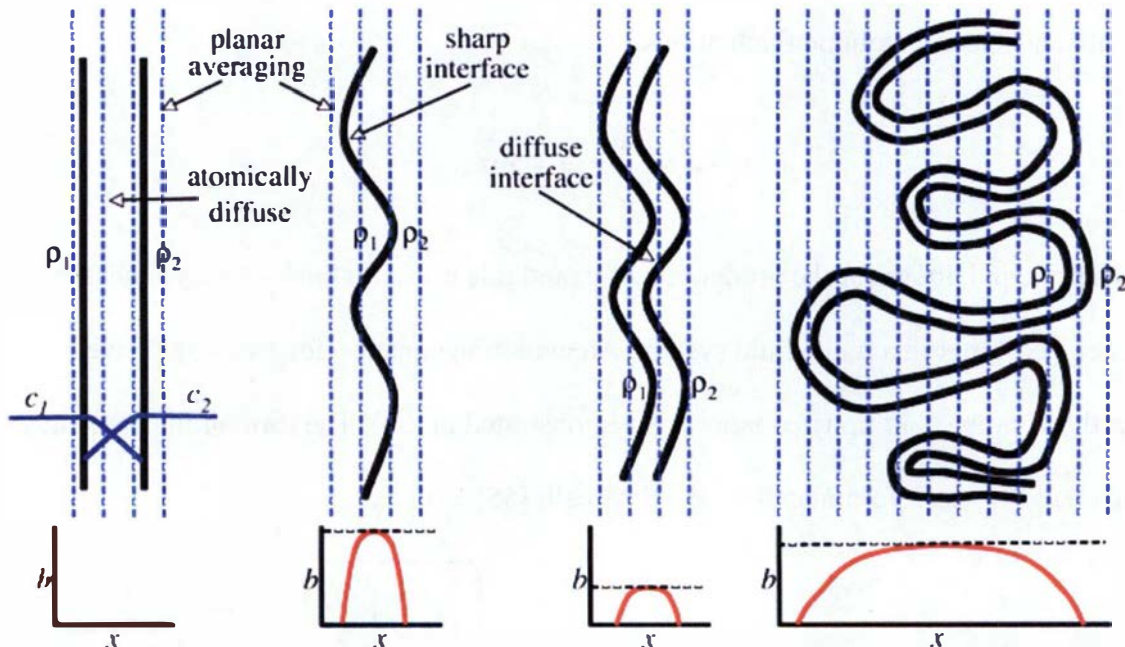


**Figure 9. Illustration of the behavior of  $b$  in a representation of subgrid turbulence dynamics.**

In Figure 9(b), again there are two fluids of different densities, but now the fluids are divided by a sharp, perturbed interface, such as one would see between immiscible fluids. In this case, the maximum possible density fluctuations occur across this interface and, therefore,  $b$  is at the maximum or immiscible value. The corresponding degree of molecular mix at the interface is zero. Now, say the interface grows such that we have a

perturbed mixing layer at the interface as shown in (c). This can occur in miscible fluids if some time is allowed to pass in which diffusion between the fluids takes place, i.e., growth occurs due to molecular diffusion. Also, in the case of either miscible or immiscible fluids, a drive applied to the interface, e.g., a shock, can cause the fluid interface to grow hydrodynamically. When the planar averaging is performed, the density fluctuations will be smaller than for the previous case in (b) and, consequently, the value of  $b$  will be lower. In the final illustration in (d), additional drive has been applied to the interface, e.g., a reshock, such that the mixing layer grows. In this case, “fresh” or pure fluid is being drawn into the mixing layer. This leads to an increase in the density fluctuations relative to case (c), resulting in an increase in the value of  $b$  and, correspondingly, a decrease in the degree of molecular mix.

In modelling variable-density flows, the density-specific volume correlation,  $b$ , makes a significant contribution to the production of  $\mathbf{a}$  and, therefore, it is important to accurately model the physical effects of  $b$ . Overall, one can see that  $b$  drives production of the mass flux velocity,  $\mathbf{a}$ . Likewise,  $\mathbf{a}$  drives production of  $K$ , which goes to the turbulent viscosity as well as the energy equation, i.e.,  $K$  drives the turbulent mixing process. When we model variable-density flows, it is vital to allow  $b$  to evolve correctly to reflect the effect of the change in density fluctuations on the mixing of the fluids. The importance of capturing these effects will be demonstrated in the results section.

Spalding [56] developed one of the earliest multi-species models that included a concentration fluctuation while investigating round turbulent free jets. In addition to the conservation of mass equation, irrespective of species, and a conservation of mass equation for the injected fluid, this model consisted of evolution equations for turbulent

kinetic energy and concentration-fluctuation squared. The concentration-fluctuation term is similar to the density-specific volume term solved in BHR2. However, unlike BHR2, in Spalding's model this term is passive and the other turbulent quantities are not a function of the concentration-fluctuation term. Also note, the Spalding model does not include a term to account for buoyancy. The species equation is still the one we use today.

Evolution of the density fluctuation,  $b$ , and coupling it to the evolution of the mass flux velocity,  $\mathbf{a}$ , has been investigated to a much lesser extent than the turbulence kinetic energy and the mass flux velocity. Evolution equations appear to have been simultaneously developed by Taulbee et al. [57] in 1991 and Besnard et al. [38] over the period from 1985 through 1993. As with the evolution equation for the mass flux velocity, the different models have similar forms, regardless of which definition of  $b$  is represented,  $b \equiv -\overline{\rho'(1/\rho)'} = -\overline{\rho'v'}$ ,  $B \equiv -\overline{\rho'\rho'}/\bar{\rho}^2$  or  $TT'$ . Again, one can refer to Chaissang et al., Chen et al. and Gregoire et al. [14, 45, 54]. We have chosen, perhaps uniquely, to evolve  $b = -\overline{\rho'(1/\rho)'}$ , simply because it is a term that naturally falls out as one of the principal production terms in the evolution of the mass flux velocity,  $\mathbf{a}$ . The "B" is more commonly seen in the literature and treated as approximately equal to " $b$ ". Its usage has been preferred, perhaps, because it is bounded between  $0 \leq B \leq 1$ , whereas there is no upper bound to  $b$  such that  $0 \leq b \leq \infty$ . Also,  $(\rho')^2$  is more closely related to  $(c')^2$ , the fluctuation in the species concentration. However, using  $B$  as an approximation for  $b$  does not account for higher order terms, which have been shown to be important [33].

As with the evolution of the turbulence kinetic energy and the mass flux velocity in BHR2, the exact production terms are maintained while the remaining terms are modelled as diffusion and dissipation. Note, that for the  $b$  equation, no terms are neglected. The diffusion is modelled as,

$$-\bar{\rho} \frac{\partial}{\partial x_n} \left( \overline{\left( \frac{\rho'}{\bar{\rho}} \right)' u_n'} \right) = \bar{\rho}^2 \frac{\partial}{\partial x_n} \left( \frac{v_t}{\bar{\rho} \sigma_b} \frac{\partial b}{\partial x_n} \right), \quad (1.64)$$

and the dissipation is given as,

$$2\bar{\rho} \left( \frac{1}{\bar{\rho}} \right)' \frac{\partial u_n'}{\partial x_n} = -C_b \bar{\rho} \frac{K^{1/2}}{S} b. \quad (1.65)$$

This gives the final evolution of  $b$  used in the BHR2 model:

$$\frac{\partial \bar{b}}{\partial t} + \frac{\partial \bar{b} \tilde{u}_n}{\partial x_n} = 2\bar{\rho} a_n \frac{\partial b}{\partial x_n} - 2(b+1)a_n \frac{\partial \bar{\rho}}{\partial x_n} + \bar{\rho}^2 \frac{\partial}{\partial x_n} \left( \frac{v_t}{\bar{\rho} \sigma_b} \frac{\partial b}{\partial x_n} \right) - C_b \bar{\rho} \frac{K^{1/2}}{S} b, \quad (1.66)$$

in which  $C_b$  and  $\sigma_b$  are model coefficients.

### 3.1.7 Turbulence length scale

By definition, the turbulence length scale is

$$S \equiv \frac{K^{3/2}}{\varepsilon}, \quad (1.67)$$

where  $\varepsilon$  is the turbulence kinetic energy dissipation rate. The evolution equation for  $S$  is developed analogous to the  $K$  equation with the assumption that the production and dissipation of  $K$  and  $S$  are proportional:

$$\frac{1}{K} \frac{dK}{dt} \Big|_P \propto \frac{1}{S} \frac{dS}{dt} \Big|_P \quad (1.68)$$

or

$$\frac{1}{K} \frac{d\rho K}{dt} \propto \frac{1}{S} \frac{d\rho S}{dt}. \quad (1.69)$$

As an exception, the diffusion/transport of  $S$  is modelled as  $\frac{\partial}{\partial x} \left( \frac{\rho v_t}{\sigma_s} \frac{\partial S}{\partial x} \right)$  rather than

$\frac{S}{K} \frac{\partial}{\partial x} \left( \frac{\rho v_t}{\sigma_s} \frac{\partial K}{\partial x} \right)$ , i.e., the transport is dependent on  $\frac{\partial S}{\partial x}$  and not  $\frac{\partial K}{\partial x}$ . An evolution

equation for  $S$  can then be written as,

$$\begin{aligned} \frac{\partial \bar{\rho} S}{\partial t} + \frac{\partial \bar{\rho} S \tilde{u}_n}{\partial x_n} &= \frac{S}{K} \left[ \left( \frac{3}{2} - C_4 \right) a_n \frac{\partial \bar{\rho}}{\partial x_n} - \left( \frac{3}{2} - C_1 \right) R_{in} \frac{\partial \bar{\rho}}{\partial x_n} \right] \\ &\quad - C_3 \bar{\rho} S \frac{\partial \tilde{u}_n}{\partial x_n} + \frac{\partial}{\partial x_n} \left( \frac{\bar{\rho} v_t}{\sigma_\epsilon} \frac{\partial S}{\partial x_n} \right) - \left( \frac{3}{2} - C_2 \right) \bar{\rho} K^{1/2}, \end{aligned} \quad (1.70)$$

where  $C_1, C_2, C_3, C_4$  and  $\sigma_\epsilon$  are model coefficients.

### 3.2 The final BHR2 turbulence model

In summary, the final BHR2 model as implemented in the RAGE hydrocode [58] is given

as,

$$\frac{\partial \bar{\rho} K}{\partial t} + \frac{\partial \bar{\rho} K \tilde{u}_n}{\partial x_n} = a_n \frac{\partial \bar{P}}{\partial x_n} - R_{in} \frac{\partial \bar{\rho}}{\partial x_n} + \frac{\partial}{\partial x_n} \left( \frac{\bar{\rho} v_t}{\sigma_k} \frac{\partial K}{\partial x_n} \right) - \bar{\rho} \frac{K^{3/2}}{S}, \quad (1.71)$$

$$\begin{aligned} \frac{\partial \bar{\rho} a_i}{\partial t} + \frac{\partial \bar{\rho} a_i \tilde{u}_n}{\partial x_n} &= b \frac{\partial \bar{P}}{\partial x_n} - \frac{R_{in}}{\bar{\rho}} \frac{\partial \bar{\rho}}{\partial x_n} - \bar{\rho} a_n \frac{\partial (\tilde{u}_i - a_i)}{\partial x_n} + \bar{\rho} \frac{\partial a_i a_n}{\partial x_n} \\ &\quad + \frac{\partial}{\partial x_n} \left( \frac{v_t}{\bar{\rho} \sigma_a} \frac{\partial a_i}{\partial x_n} \right) - C_{a1} \bar{\rho} a_i \frac{K^{1/2}}{S}, \end{aligned} \quad (1.72)$$

$$\frac{\partial \bar{\rho} b}{\partial t} + \frac{\partial \bar{\rho} b \tilde{u}_n}{\partial x_n} = 2 \bar{\rho} a_n \frac{\partial b}{\partial x_n} - 2(b+1) a_n \frac{\partial \bar{\rho}}{\partial x_n} + \bar{\rho}^2 \frac{\partial}{\partial x_n} \left( \frac{v_t}{\bar{\rho} \sigma_b} \frac{\partial b}{\partial x_n} \right) - C_b \bar{\rho} \frac{K^{1/2}}{S} b, \quad (1.73)$$

$$\frac{\partial \bar{\rho}S}{\partial t} + \frac{\partial \bar{\rho}S\tilde{u}_n}{\partial x_n} = \frac{S}{K} \left[ \left( \frac{3}{2} - C_4 \right) a_n \frac{\partial \bar{p}}{\partial x_n} - \left( \frac{3}{2} - C_1 \right) R_{in} \frac{\partial \bar{\rho}}{\partial x_n} \right] \quad \text{ui ???}$$

$$-C_3 \bar{\rho} S \frac{\partial \tilde{u}_n}{\partial x_n} + \frac{\partial}{\partial x_n} \left( \frac{\bar{\rho} v_t}{\sigma_\epsilon} \frac{\partial S}{\partial x_n} \right) - \left( \frac{3}{2} - C_2 \right) \bar{\rho} K^{1/2} \quad (1.74)$$

and

$$\frac{\partial \bar{\rho} \tilde{c}^k}{\partial t} + \frac{\partial \bar{\rho} \tilde{c}^k \tilde{u}_n}{\partial x_n} = \frac{\partial}{\partial x_n} \left( \frac{\bar{\rho} v_t}{\sigma_c} \frac{\partial \tilde{c}^k}{\partial x_n} \right), \quad (1.75)$$

along with the conservation of mass, momentum and energy and the Ristorcelli Reynolds stress model [46] described earlier.

The evolution equations of  $K$ ,  $\mathbf{a}$ ,  $b$  and  $S$  give the rate of change of the variable as equivalent to production plus diffusion and dissipation of the quantity. The model coefficients are given in the next section and have been set using a variety of mostly incompressible flow experiments, some of which will be described in the Results section.

If one were interested in the amount of molecular mix between fluids, a molecular mix variable,  $\theta$ , can be related to  $b$  such that,

$$\theta \sim 1 - \frac{b}{b_{max}}, \quad (1.76)$$

where  $b_{max}$  is obtained by reducing  $b$  to the two-fluid analytic solution as demonstrated in [59],

$$b_{max} = -1 + \sum_m \frac{a_m}{\rho_m} \sum_n a_n \rho_n. \quad (1.77)$$

This derivation follows in principal, though not in detail, the pioneering work of Dankwertz [60].

### 3.3 Coefficients: defaults and their origins (in a nutshell)

As stated above, the coefficients in the BHR2 model have been set based on a variety of experiments. The coefficients that are used for the model for low and high Atwood number RT flows and for 1-D shocks are given in Table 1 along with their origins. Note, some of the values are historical and they were specified using the original BHR model implementation [61]. Additional discussion of coefficient specification is presented in the results section under self-similar analysis for low Atwood Rayleigh-Taylor flows.

Table 1. Coefficients defined for use in the BHR2 model.

Coefficients	Variable Equation	High Atwood RT DNS [25]	Low Atwood RT Channel Experiments [42]	1-D Shock Tube [62]	Origin
$C_1$	$S$	1.44	1.44	1.44	Free shear layer growth
$C_2$	$S$	1.92	1.92	1.92	Isotropic decay rate
$C_4$	$S$	1.05	0.75	0.75	RT experiments (iteration)
$C_{al}$	$a$	6.0	6.0	6.0	RT experiments (iteration)
$\sigma_\varepsilon$	$S$	0.1	0.1	0.1	Top-hat S distribution for RT
$\sigma_c$	$c^k$	0.6	0.6	0.6	Global (historical value set based on optimization with RT)
$\sigma_b$	$b$	3.0	3.0	3.0	RT DNS (iteration)
$C_b$	$b$	2.5	2.5	0.25	RT, RM (iteration)
$C_3$	$S$	0.0	0.0	0.0	Unstudied
$\sigma_k, \sigma_a$	$K, a$	1.0	1.0	1.0	Unstudied

### 3.4 Initialization of turbulence quantities

Initialization of turbulence quantities is not a trivial task, nor is it an exact science at this point<sup>7</sup>. Typically, we initialize the turbulence kinetic energy as  $K = 0.01 * U^2$  where,

- Kelvin-Helmholtz  $U^2 = (U_2 - U_1)^2$
- Rayleigh-Taylor  $U^2 = AgS_0$
- Richtmyer-Meshkov  $U^2 = A|u|^2$

The mass flux velocity,  $\mathbf{a}$ , is initialized to zero everywhere. The initial density-specific volume correlation,  $b$ , is set to zero everywhere except at the fluid interface. There we assume an initially sharp interface, and it is calculated as the immiscible two-fluid value for the cells on either side of the interface. If a small value is specified, e.g., some percentage of the two-fluid value,  $b$  decreases too quickly and does not recover or recovers very slowly. Due to numerical issues, it was necessary to set a minimum cut-off value for  $b$ . In the code, if  $b$  becomes a small number, it is set to zero. For most simulations, a value of  $b_{CUTOFF} = 1e-6$  was sufficient; for low Atwood numbers, a smaller value was required ( $1e-16$ ). Finally, the initial length scale,  $S_0$ , is set to a fraction of the mean amplitude of the perturbation at the interface corresponding to the most unstable mode, or to some fraction of the cell size if no other information is available. If there was a departure from this procedure for setting of the initial conditions, it is specified in the Results section with the corresponding flow.

As will be shown for the self-similar flows, like the Rayleigh-Taylor DNS and experimental results presented in this report, the initial conditions do not affect the late-time results, which are of interest in validation of the model. The conditions only determine the amount of time it takes to achieve the self-similarity.

---

<sup>7</sup> An investigation into initial conditions in turbulence currently is being pursued by Andrews [63].

### **3.5 RANS in RAGE**

The RANS method is applied in RAGE [58], the computational code used for the majority of the simulations performed for this study<sup>8</sup>. It is a multi-dimensional, multi-material, massively parallel compressible Eulerian radiation-hydrodynamics code. It was developed for solving the Euler equations coupled with a radiation diffusion equation to be applied to high-deformation flow problems. A second-order-accurate Godunov scheme is used to solve the hydrodynamics in which mixed cells are assumed to be in pressure and temperature equilibrium with separate material and radiation temperatures. An adaptive mesh refinement algorithm, continuous in space and time, is used to follow interfaces, shocks and gradients in physical quantities. RAGE includes a dynamic turbulence model, BHR2, based on the derivations of Besnard et al. [38]. It was originally implemented by M. Steinkamp [61] as “BHR” and has been modified more recently by K. Stalsberg-Zarling, M. Steinkamp and R. Rauenzahn, giving the form we now call BHR2. RAGE hydrodynamics without turbulence effects is comprised of the Euler equations (inviscid Navier-Stokes), though options for viscosity are available. RAGE with turbulent mix consists of Eqns. (1.21)-(1.24) and the BHR2 model to close the system of equations. Note the total energy, which includes the internal energy, is transported (see RAGE manual [64] for more details).

## **4. BHR2 model comparison to physical and computational experiments**

The final goal of this work is to model and solve rapid, transient flows effectively. However, for setting model coefficients, we begin by using steady-state flows, including homogeneous isotropic turbulence (HIT), Kelvin-Helmholtz (KH) turbulence and

---

<sup>8</sup> Note, for this study, we are primarily investigating incompressible flows. Because RAGE is a compressible code, special consideration must be given to the initialization of the hydro. Additionally, issues sometimes arise in the simulation results. Comments to these effects are presented in the results sections where appropriate.

Rayleigh-Taylor (RT) turbulence under self-similar conditions. This eliminates some of the complexity of the flows, thus simplifying the analysis while maintaining other important properties. Richtmyer-Meshkov turbulence, also important to the flow problems of interest, has been explored in the past [34, 65-68] and will be the focus of future efforts towards verification and validation of the BHR models.

There are various categories of variable-density flows. Following [14], we first separate variable-density flows into constant mass and constant volume flows. In the former, the density changes due to volume changes while the mass remains constant; in the latter, the mass of the fluid varies while the volume remains constant.

For constant mass flows, the volume may change due to geometrical effects, e.g., during the compression and expansion processes in an engine cylinder. Volume changes can occur due to Mach effects, such as in the high-speed flow around an aircraft. Also, there are dilatational or contraction effects, in which the fluid expands or constricts due to heating and cooling, i.e., thermal effects. This often leads to buoyancy effects, e.g., “fall overturn” in the cooling of a lake surface in the winter.

For constant volume flows, the mass can change due to spatially inhomogeneous composition or temperature. Variations in density occur due to mixing effects, for example, stirring creamer into your coffee. Chaissang [14] also notes that of the variable-density effects listed, with the exception of Mach effects, all can occur in low speed flows.

Comparisons of results obtained using BHR2 in RAGE have been made with fundamental experiments<sup>9</sup> that fall under the category of constant volume flows. The following sections will include model validation and/or coefficient specification using

---

<sup>9</sup> Here, we use the term “experiments” loosely to also include DNS and LES results.

results from this type of variable-density flows. They include homogeneous isotropic decay, followed by Kelvin-Helmholtz experiments, a variety of Rayleigh-Taylor results, including both DNS and traditional experiments and, finally, DNS for homogeneous variable density Rayleigh-Taylor turbulence. For variable-density flows that can be categorized under the constant mass flows, particularly for Mach effects, further validation of the model will be presented in a later report. This will include Richtmyer-Meshkov turbulence, e.g., the 1-D shock tube experiments of Poggi [69] and Vetter and Sturtevant [62], and the 1-D shock tube LES of Caltech [34].

#### **4.1 Homogeneous isotropic decay: “grid turbulence”**

The following is a short description of the decay process for homogeneous isotropic turbulence, also known as “grid turbulence”. We follow the analysis of Steinkamp in [59], but tailor it to our specific model. For a general description of the problem see, for example, Mohamed and Larue [70] or Pope [11]. Grid turbulence describes the decay of turbulence in a single-phase fluid. The turbulence is homogeneous and isotropic with no production. In this case, the BHR2 equations reduce to simply,

$$\frac{dK}{dt} = -\frac{K^{3/2}}{S} \quad (1.78)$$

and

$$\frac{dS}{dt} = -(3/2 - C_2)\sqrt{K}. \quad (1.79)$$

This set of equations has the following solution:

$$K = K_0(1 + t / t_0)^{-n} \quad (1.80)$$

$$S = S_0(1 + t / t_0)^{1-n/2}. \quad (1.81)$$

Now substituting Eqns. (1.80) and (1.81) into Eqn. (1.78), an expression for  $t_0$  can be obtained:

$$t_0 = \frac{nS_0}{\sqrt{K_0}}. \quad (1.82)$$

Substituting Eqn. (1.82), as well as Eqns. (1.80) and (1.81), into Eqn. (1.79) gives the following expression for  $C_2$ :

$$C_2 = \frac{n+1}{n}. \quad (1.83)$$

This problem then is simplified to picking the appropriate decay coefficient,  $n$ . In our current model, we have kept with the standard of -1.09, i.e.,  $C_2 = 1.92$ . This is consistent with the historic value used in the  $K$ - $\varepsilon$  model from the original Comte-Bellot and Corsin [71] finding. Mohamed and Larue [70] suggest that a more universal value of  $n = 1.3$ , corresponding to  $C_2 = 1.77$ , should be used. The value of this coefficient will be part of future studies to explore the effect these differences will have on global data matches.

It should be noted that homogeneous, isotropic turbulence describes the condition at the far field of the RT problem, where there is no knowledge of the mixing layer. We start with the stated initial conditions but the free stream is undergoing homogeneous, isotropic decay and is evolving, albeit slightly, in time. We still observe self-similarity in the mixing layer, but the flow changes outside of the edges of the layer.

This sample problem, though, does allow for a verification of a portion of the model. Shown in Figures 10 and 11 is a comparison of the solution of Eqns. (1.78) and (1.79) to BHR2 in RAGE calculations, which have been initialized with  $K_0 = 0.05$  and  $S_0 = 0.1$ . Excellent agreement is observed between the analytic and code results.

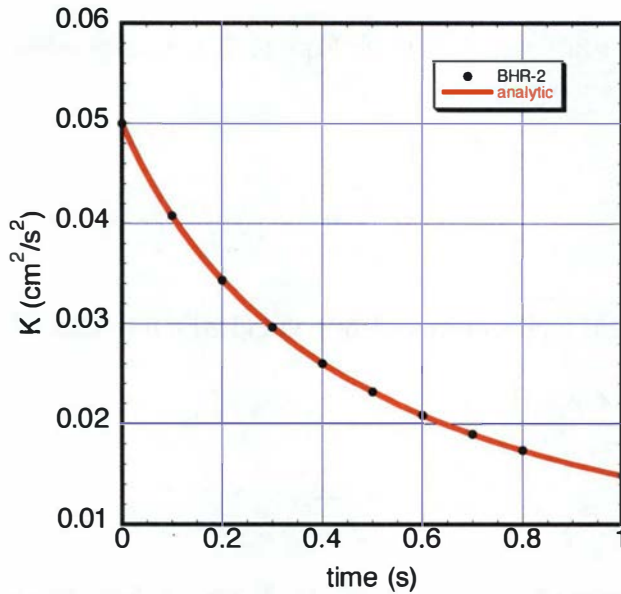


Figure 10. Comparison of analytic expression and BHR-2/RAGE results for homogeneous isotropic decay ( $S$ ).

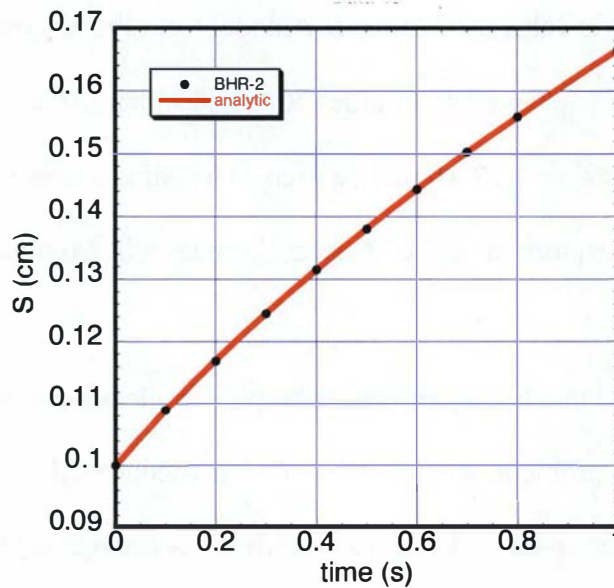


Figure 11. Comparison of analytic expression and BHR-2/RAGE results for homogeneous isotropic decay ( $K$ ).

#### 4.2 Variable-density homogeneous isotropic turbulence

Like grid turbulence, the BHR2 model equations can be reduced for the case of variable-density homogeneous isotropic turbulence. We obtain the same solutions for the

turbulence kinetic energy and length scale shown above. For the density-specific volume correlation, similar analysis gives,

$$\frac{\partial b}{\partial t} = -C_b \frac{\sqrt{K}}{S} b. \quad (1.84)$$

This equation has the solution:

$$b = b_0 \left( 1 + \frac{t}{t_0} \right)^{-C_b n}. \quad (1.85)$$

The mass flux velocity equation can be reduced in a similar fashion and gives,

$$\frac{\partial \mathbf{a}}{\partial t} = -C_{al} \frac{\sqrt{K}}{S} \mathbf{a}. \quad (1.86)$$

This equation has the solution:

$$\mathbf{a} = \mathbf{a}_0 \left( 1 + \frac{t}{t_0} \right)^{-C_{al} n}. \quad (1.87)$$

The model predicts the solutions given in Eqns. (1.85) and (1.87). Both  $b$  and  $\mathbf{a}$  follow the solution of  $K$ , but with different constants. As mentioned previously, there is a lack of available data and the coefficients  $C_b$  and  $C_{al}$  cannot be specified as simply as  $C_2$  was for grid turbulence.

#### 4.3 Kelvin-Helmholtz

The validation work for free shear layer mixing was based principally on the experimental works of Bell and Mehta [72] and the DNS of Rogers and Moser [73]. Also included are summaries from Pope [11]. The free shear layer generally is achieved experimentally through a spatially varying but steady in time configuration, as shown in Figure 12. Contrarily, typical DNS of free shear layers vary temporally with no mean variation spatially, except in the direction of growth of the layer. Our calculations are of

a temporally growing layer and we use both data sets for comparison as a means of demonstrating some of the expected variations between experiments. One experimental measurement that is different, and which we don't claim to match, is the centreline variation, defined as the 0.5 velocity difference, for the spatial layer.

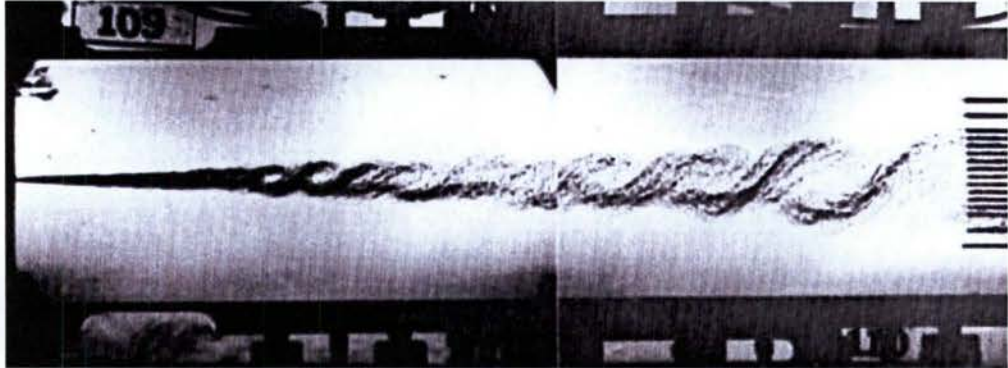


**Figure 12. Picture of experimental free shear layer generated at Caltech University [74].**

#### 4.3.1 Analysis of time evolution of the free shear layer

In the investigation of temporally growing layers, we first examine the time evolution of the free shear layer. While a variety of quantities may be considered, because it is representative of the flow, we examine the non-dimensional turbulence kinetic energy,  $K^* = K / (U_1 - U_2)^2$ , where  $U_1$  and  $U_2$  are the stream velocities. This value is plotted in Figure 13 as a function of non-dimensionalized time,  $T = t / |L / (U_1 - U_2)|$ , for various initializations of  $S$ , the turbulence length scale. We non-dimensionalize  $S$  by dividing it by  $S_0 = 0.1\Delta x$ , the method prescribed earlier in Section 0 for a general case. Given sufficient time, over a very large range of  $S_0$ , the model collapses to the same value. These behaviours of the final steady-state values appear to be independent of initial conditions in both the KH and RT cases.

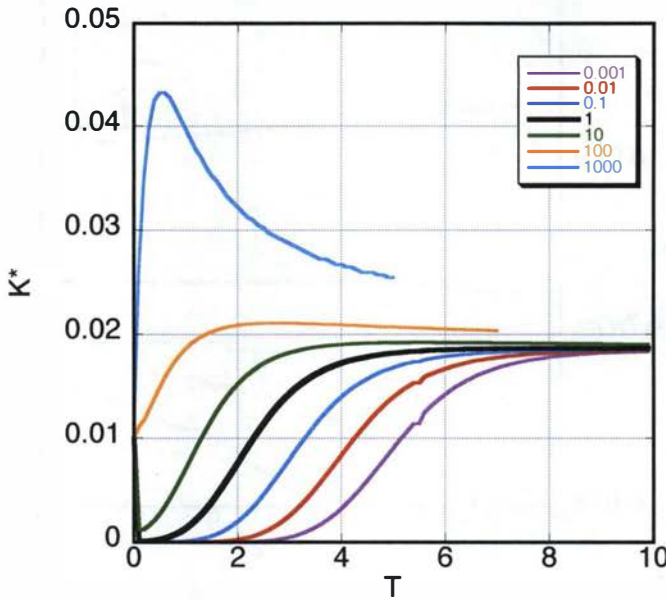


**Figure 13.** Variation of non-dimensional  $K$  with time for various initial length scales at a given resolution. The curves for 100 and 1000 are incomplete due to the mixing width reaching the edge of the domain earlier in time.

This observation must be qualified. An expansion of the late time regime is shown in Figure 14. None of the curves coincide exactly, but the curves for  $S_0 = 0.1$  and  $S_0 = 1.0$  are within 1% of each other. The remaining curves trend toward consistent values. Despite the relatively small differences, even the curves for  $S_0 = 0.1$  and  $S_0 = 1.0$  are not completely time-independent. This can be seen by examining the curves for  $\frac{dK^*/dT}{K_{final}^*}$ , in Figure 15 for the full time range and in Figure 16 for the expanded region corresponding to Figure 15.

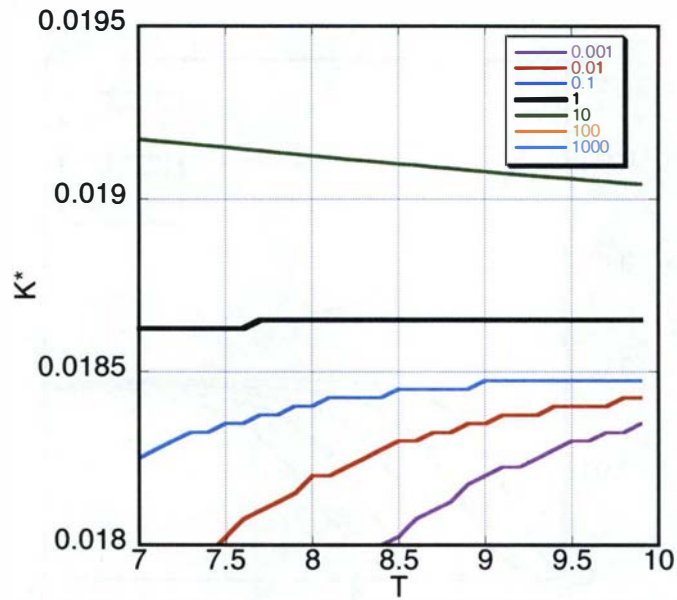


**Figure 14.** Enlarge of the late-time region showing the variation of non-dimensional  $K^*$  with time for various initial length scales at a given resolution.

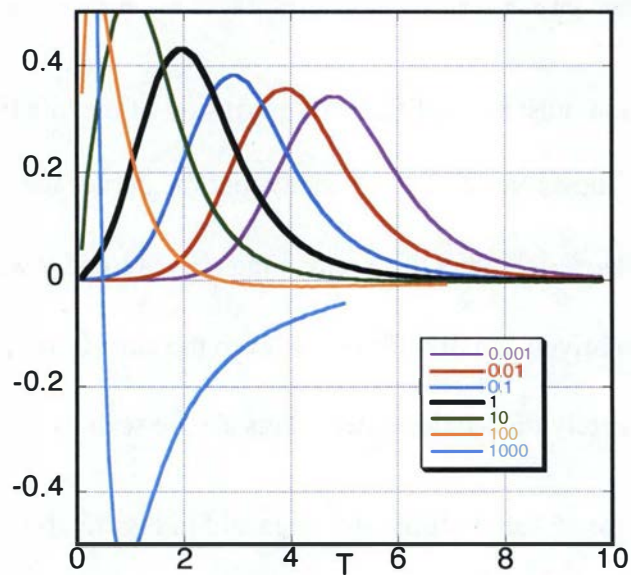


**Figure 15.** Variation of  $\frac{dK^*}{dT} / K^*_{final}$  as a function of time.

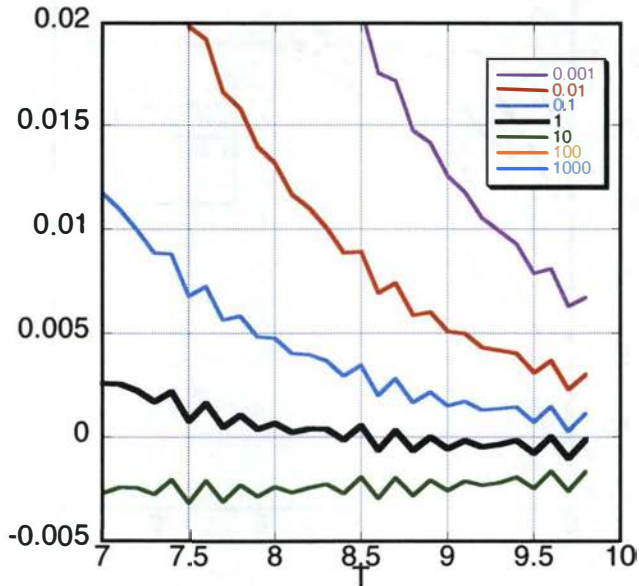


**Figure 16.** Variation for  $\frac{dK^*}{dT} / K^*_{final}$  as a function of late-time.

The model evolution of  $K^*$  at early time is shown in Figure 17 using a log scale. One can see that the value of  $K^*$  does not go to zero, but can remain small for a long time. The trends also appear independent of the choice of  $K_0$ , as shown in Figure 18, which presents results for a  $K_0 = 1.0E4$  (versus the standard  $4.0e6$  for our case).

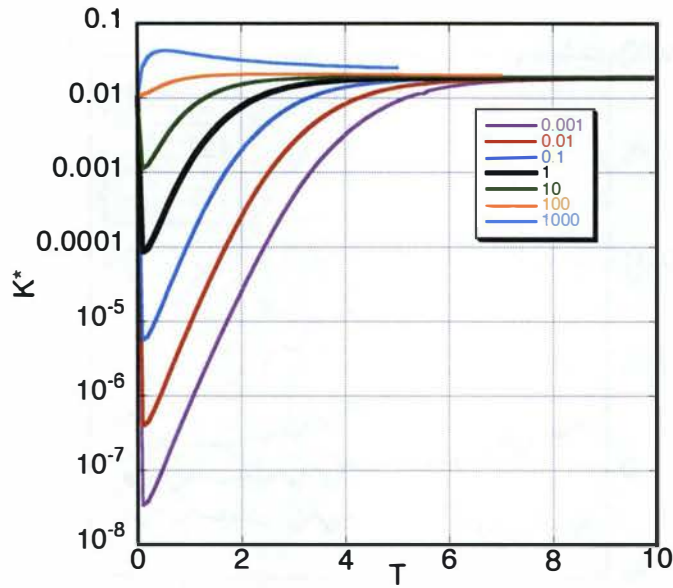


**Figure 17.**  $K^*$  shown on logarithmic scale demonstrating large variation in the evolution of  $K^*$  for different  $S_0$ .

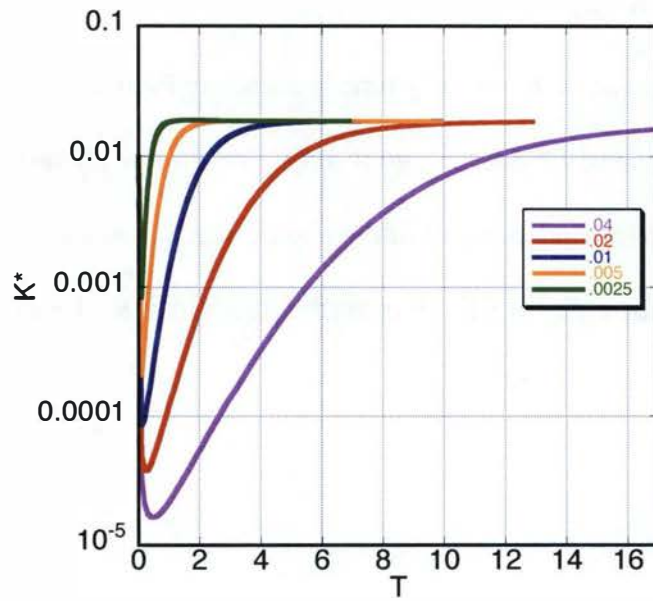


**Figure 18.** The effect of mesh resolution on early-time behaviour for a small initial length scale,  $S_0 = 1$ , is shown for  $K^*$  plotted on a logarithmic scale.

The intention of describing these behaviours is to illustrate the need for caution when examining early-time evolution of the turbulent flow. Though the late-time behaviour of the mixing layer is reasonably independent of the initial conditions and grid

resolution, the same is not true for early-time behaviour. This is discussed in more detail below.

The variation in early-time model behaviour is dependent not only on the manner in which the model is initialized, but also on the mesh resolution used for calculating the flow. In Figure 19, results for the standard settings as given above are shown for different grid refinements,  $\Delta x / (L / 2)$ , where  $L$  is a characteristic length scale. The same final steady-state condition is reached regardless of cell size; the speed at which this value is reached is not independent of the cell size. This dependence on the initial values can be seen in Figure 19, which is plotted through late-time. The results collapse or converge in early time, showing how the problem evolves and not just the final state.

The early-time evolution of unsteady models, such as we are using here, is a complex behaviour that balances the numerical diffusion, the initial transport, production and dissipation of the turbulence. These are functions of cell size, the velocity gradients that drive the physics and the manner in which one initializes the problem, affecting the production and dissipation. The material presented here is incomplete. This discussion merely illustrates the need to understand the problem that is being solved and the behaviour at the desired result time. For example, in any of the above cases if one was looking at  $T = 100$  versus  $T = 1000$ , the difference in the flow behaviour is relatively insignificant; if one is looking at  $T = 1$  versus  $T = 0.1$ , then the precise problem, i.e., the physical initial values for  $K$  and  $S$  and the resolution requirements are paramount.

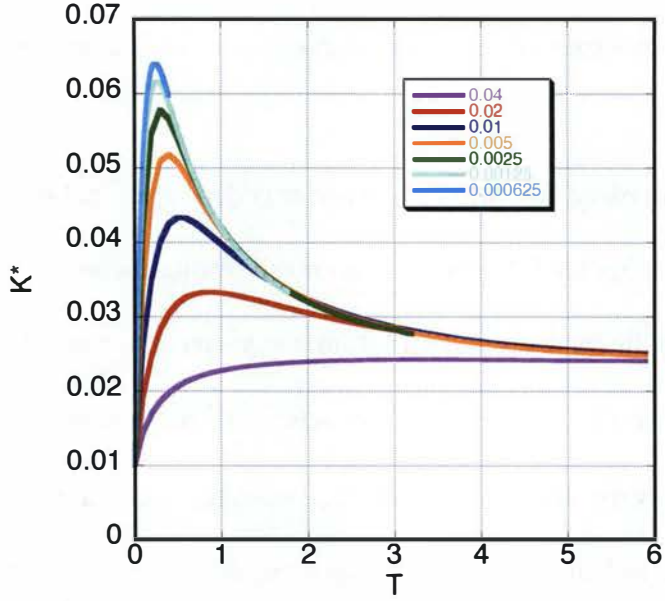


**Figure 19.** Effect on early time behavior of turbulence kinetic energy,  $K^*$ , over a range of mesh refinements for large  $S_0$  (1000).

#### 4.3.2 Comparison to data

Two types of data are used for comparison to the model, namely, the steady-state non-dimensional growth rate of the mixing layer,  $\alpha$  (defined in detail later), and the non-dimensional turbulence kinetic energy,  $K^*$ , as was discussed in the opening section. These parameters are primarily driven by the model coefficient  $C_1$ , and they vary with the coefficient in the manner shown in Figure 20. The growth rates experimentally vary from 0.06 to 0.11 [11], which results in a range from 1.0 to 1.44 for  $C_1$ ; 1.44 is the standard value used in  $K - \varepsilon$  models. The two “experiments” considered here both have a value of  $K_{max}$  near 0.03, which would correspond to  $C_1 = 1.1$  and a growth rate of 0.095. We continue to use the standard value of 1.44 at this time with the premise that we are applying the model across systems with long wavelength perturbations and, therefore, produce the minimum growth rates. This subject will be extended to the discussion of Raleigh-Taylor turbulence, but  $C_1$  may be adjusted if larger growth rates are warranted.

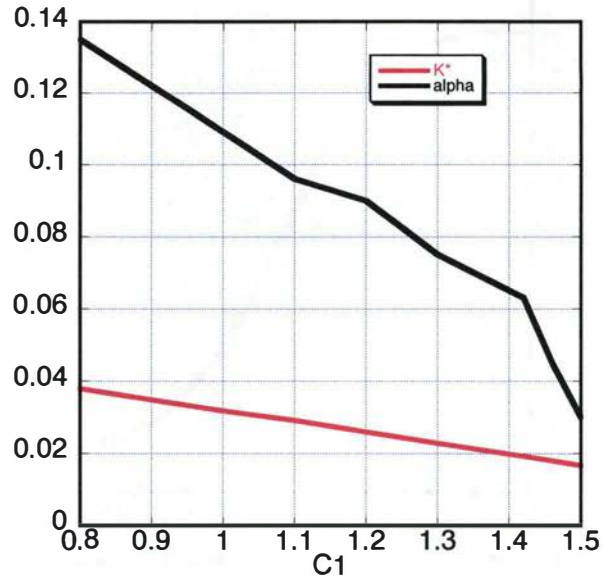


**Figure 20.** Variation of non-dimensionalized turbulent kinetic energy,  $K^*$  and growth rate,  $\alpha$ , with model coefficient  $C_1$ .

Beyond the integral quantities described above, also of interest are the shapes of the profiles for velocity and turbulent kinetic energy distributions, which are given in Figures 21 and 22. As can be seen, the match is quite good. For the sake of completeness the distribution of the turbulence length scale,  $S$ , is included in Figure 23. This profile tends to be top-hat and will be discussed in more detail in the RT section.

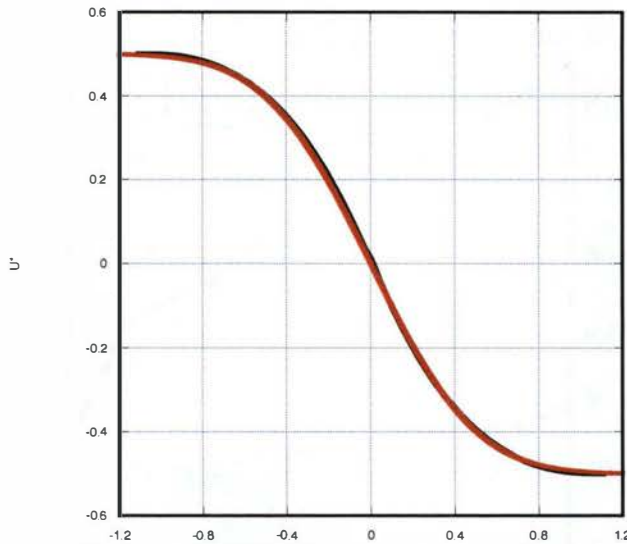


**Figure 21.** Non-dimensionalization of the velocity profile of a RT mixing layer, comparing the data of Bell and Mehta [72] in red with the simulated results using BHR2 in RAGE in black.

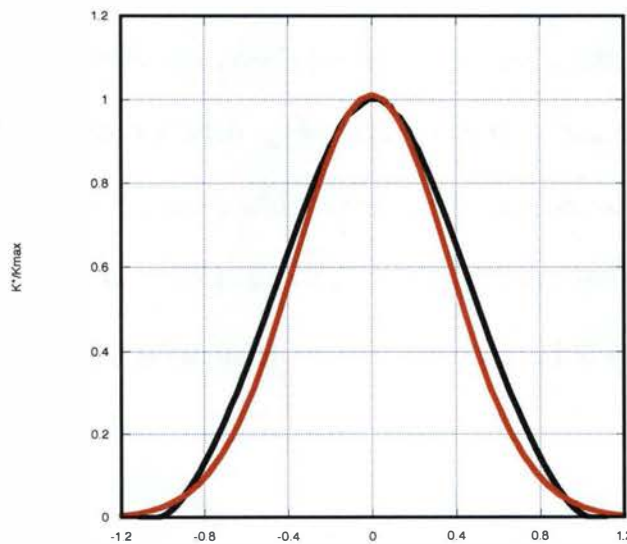


**Figure 22.** Non-dimensionalization of turbulence kinetic energy across a RT mixing layer, comparing the data of Bell & Mehta [72] in red with the simulated results using BHR2 in RAGE in black.

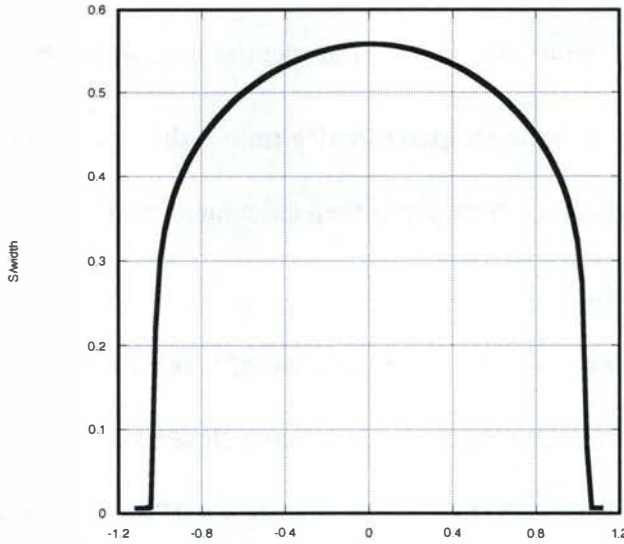


**Figure 23. Non-dimensionalization of  $S$  for a RT mixing layer from simulations using BHR2 in RAGE. No data was available.**

#### 4.4 Rayleigh-Taylor turbulence

As presented earlier in this report, Rayleigh-Taylor (RT) instabilities occur due to a mismatch between the pressure gradient and the density gradient between two different density fluids [22, 23]. An interface between fluids of different densities is Rayleigh-Taylor unstable if  $\nabla p \bullet \nabla \rho < 0$ . The basic mechanism that amplifies or causes the perturbations to grow is the baroclinic generation of vorticity which is given by

$$\frac{1}{\rho^2} \nabla p \times \nabla \rho.$$

##### 4.4.1 Initialization of Rayleigh-Taylor flows in RAGE

Because the simulation of a Rayleigh-Taylor mixing layer is an incompressible problem and RAGE was developed as a compressible code, the hydro initialization required special consideration when setting up the problem in order to prevent a shock from occurring. The specific internal energy in the two fluids must be equal such that

$$\rho_1 C_{v,1} = \rho_2 C_{v,2} = 10^4, \text{ where } \rho \text{ is density and } C_v \text{ is the specific heat of the fluid for a}$$

constant volume. The pressure interface then can be calculated as  $P = (\gamma - 1)\rho C_v T$ , where  $\gamma = C_p / C_v$  (polytropic index),  $C_p$  is the specific heat at constant pressure and  $T$  is temperature. The specified input temperature determines the temperature and the pressure at the interface. The hydrostatic pressure is then calculated from  $\Delta P = -\rho g \Delta x$ , where  $g$  is gravitational acceleration.

For this simulation, we chose a temperature of 5 keV (1 eV = 11,604 K) to alter the speed of sound such that the fluids would behave close to an incompressible manner. With a domain ranging from -200 to 200 cm, gravity  $g = 1000 \text{ cm/s}^2$  and  $\gamma = 1.4$ , this yields a Mach number of  $M \ll 0.1$ .

The effects of the temperature on simulation results were investigated by varying the temperature from 2 keV to 200 keV. The results at  $T = 5 \text{ keV}$  varied by  $\pm 10\%$  across this temperature range. Note, for the particulars specified in these simulations,  $T < 2 \text{ keV}$  produced noisy results;  $T > 200 \text{ keV}$  leads to long run times due to time-step control.

Finally, Figure 24 shows the effect of temperature variation on the late-time growth rate of the mixing layer. A temperature of  $T = 5 \text{ keV}$  was used throughout this study as a reasonable compromise between results with small temperature deviations and feasible simulation times.

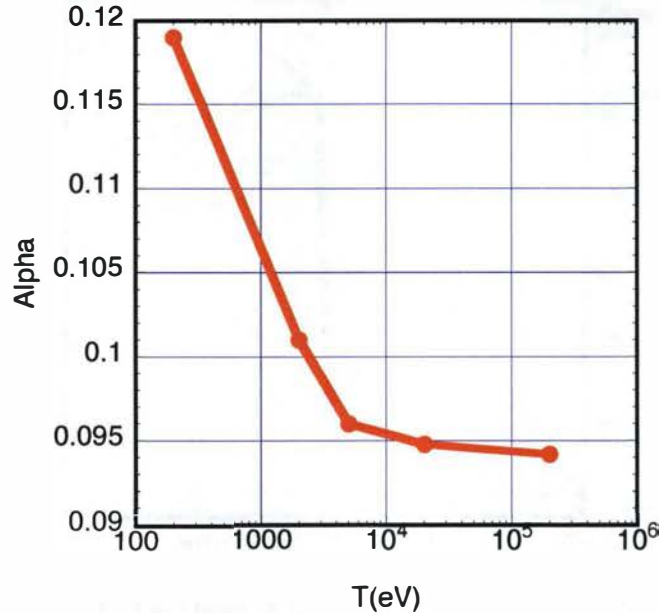


**Figure 24.** Growth rate,  $\alpha$ , as a function of the background temperature for an RT simulation using BHR2 in RAGE.

Additionally, problems associated with the use of a compressible code lead to erroneous results for RT flows at very low and high Atwood numbers. In Figure 25, density is plotted as a function of position at various times for an Atwood number of 1.0e-4. Though the density jump at the interface between the two fluids is captured, the density profiles within the pure fluids vary non-physically.

In Figure 26, a similar plot was generated for pressure for an Atwood number of 0.9. The profile of the pressure is captured correctly at initial time, but develops oscillations early in the simulation before self-similarity can be achieved.

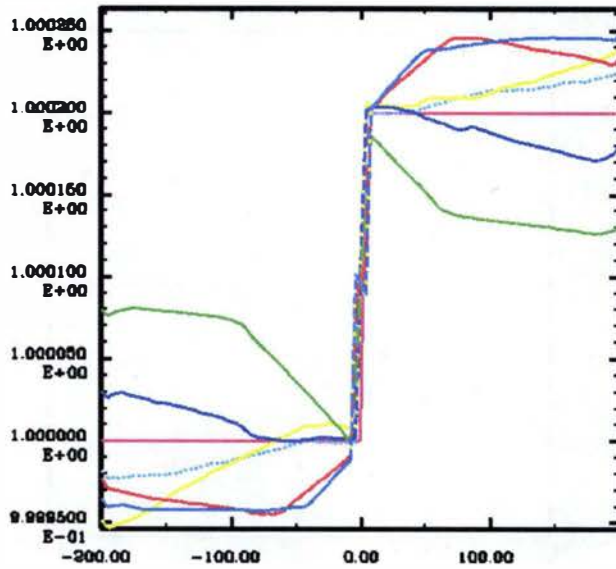


**Figure 25.** Density versus position at various times for an Atwood number of  $1.0\text{e-}4$  using BHR2 in RAGE. Note, the variations observed here are of the order of  $1.0\text{e-}5$ .

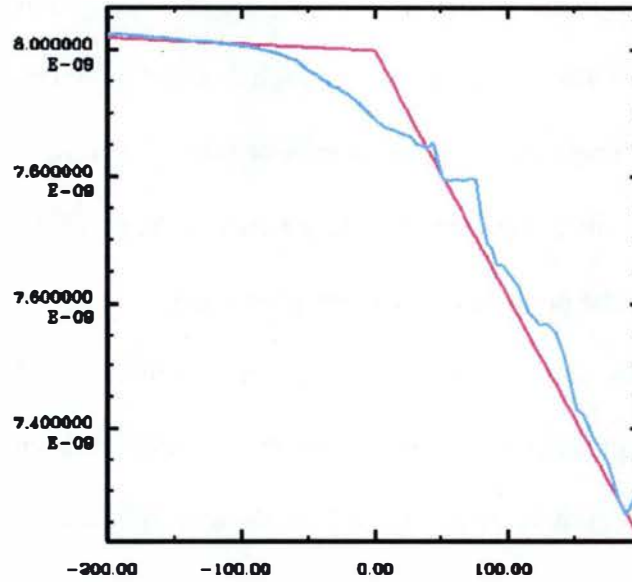


**Figure 26.** Pressure versus position at times 0 and 1 second for an Atwood number of 0.9 using BHR2 in RAGE.

In a tangent investigation to validate the model at both lower and higher Atwood numbers, BHR2 also was implemented and tested in an *incompressible* code, RTI3D, developed by Andrews [75]. A comparison was made of the asymptotic growth rates

associated with the mixing layer under self-similar conditions. We first define the following scalings:

$$h = \alpha A g t^2, \quad (1.88)$$

$$K_{\max} = \alpha_K (A g t)^2, \quad (1.89)$$

$$a_{\max} = \alpha_a (A g t), \quad (1.90)$$

and

$$b_{\max} = \text{constant}. \quad (1.91)$$

Conversely, the growth rates for the mixing width, peak turbulence kinetic energy and peak mass flux velocity are calculated as follows:

$$\alpha = \alpha_{\text{bubble}} + \alpha_{\text{spike}} = \frac{\Delta h_{\text{tot}}}{\Delta (A g t^2)}, \quad (1.92)$$

$$\alpha_K = \frac{\Delta K_{\max}}{\Delta (A g t)^2}, \quad (1.93)$$

and

$$\alpha_a = \frac{\Delta a_{\max}}{\Delta (A g t)}. \quad (1.94)$$

For the high Atwood number of 0.9, growth rate results from RAGE and the RTI3D code are compared in Table 2. The difference in results for the asymptotic growth rates of the mix width, peak turbulence kinetic energy and peak mass flux velocity vary from 3 to 8.5%. The difference in the maximum value of  $b$ , which is nearly constant under self-similar conditions, differs by 3.3%. Additional comparisons with experimental data for a high Atwood number will be shown in a later section for the LEM experiments [76].

**Table 2.** For the high Atwood number of 0.9, growth rate results are compared for the RAGE and RTI3D codes.

Variable	RAGE	RTI3D	% difference
$\alpha$	0.096	0.099	3.0
$\alpha_K$	0.0082	0.0075	8.5
$\alpha_a$	-0.00156	-0.00167	6.6
$b_{MAX}$	5.8e-4	6.0e-4	3.3

Returning to setup, the initial conditions for turbulence quantities also must be specified. The model was initialized with  $S_0 = 0.01$  cm and  $K_0 = 0.1$  cm<sup>2</sup>/s<sup>2</sup>. By default, the mass flux velocity,  $\mathbf{a}$ , is initialized to zero and  $b$  is calculated as the immiscible value at the interface and set to zero elsewhere. As previously noted in Section 3.4, for the self-similar RT flows in which we are interested in the late-time effects, these initial conditions only affect the time it takes to achieve self-similarity, but not the final result.

The BHR2 simulations were allowed to run until self-similar flow conditions were achieved. Results under these conditions were then compared with the DNS results.

#### 4.4.2 Cabot and Cook RT DNS

The growth of a Rayleigh-Taylor mixing layer was investigated by Cabot and Cook [25, 77, 78] using DNS and further analysed by Livescu et al. [48]. Their results then were used for calibrating BHR2 model coefficients and validation of the model, including a comparison of the individual terms of the  $K$ ,  $\mathbf{a}$  and  $b$  evolution equations that were obtained from the RAGE simulations. The details are presented below.

#### 4.4.2.1 Method and simulation details

Cabot and Cook solved governing equations for two incompressible, non-reacting, miscible fluids. They used a hybrid spectral-Pade scheme for spatial derivatives, combined with a pressure-projection method for the time derivatives. Please refer to [77, 78] for further details on the description and validation of this numerical algorithm.

The simulations were performed using a  $3072 \times 3072 \times N_z$  vertically expanding grid with periodic boundaries in the  $x$  and  $y$  directions. The initial  $N_z$  value was set to 256 and increased as the mixing layer increased in thickness (see Figure 27 for depiction of mixing layer). The flow began from a quiescent state in which a heavy fluid sat atop of a light fluid; the density ratio was 3/1 giving an Atwood number of 0.5. There was a thin perturbed diffuse interface separating the two fluids. The density gradient-pressure gradient mismatch in the system results in a Rayleigh-Taylor turbulence mixing layer.

This flow had a bulk Reynolds number of  $Re = \frac{hh'}{\nu} = 32,000$  and a turbulence Reynolds

number of  $Re = \frac{\tilde{K}^2}{\nu\varepsilon} = 4600$ , indicating that the mixing was fully turbulent.

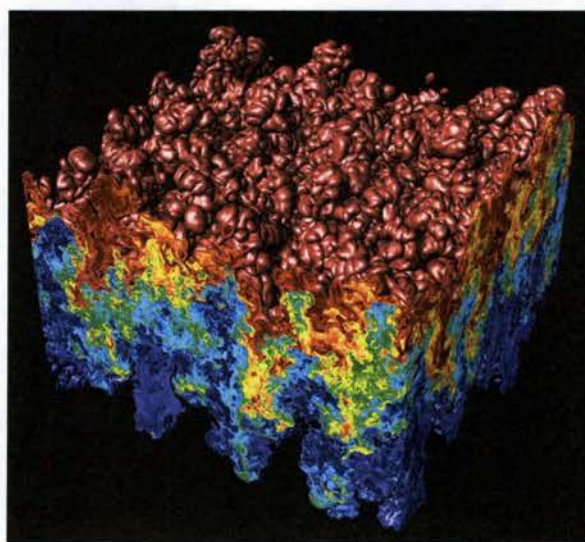


**Figure 27. DNS of Rayleigh-Taylor mixing layer in the fully turbulent regime [25].**

Results are presented next for BHR2 and the DNS comparing the turbulence variables, as well as the individual terms of the  $K$ ,  $\mathbf{a}$ , and  $b$  evolution equations.

#### 4.4.2.2 RAGE simulation results

A 2-D Rayleigh-Taylor simulation with the same density ratio of 3:1 was performed in RAGE using the BHR2 mix model. The grid zoning was set to two cells in the  $x$ -direction and 200 cells in the  $z$ -direction, which is in the direction of the growth of the mixing layer. The initial density and pressure profiles are shown in Figures 28 and 29, respectively. The  $x$ -axis in the figures indicates the location in the fluid across the width of the mixing layer; the light and heavy fluids are shown on the left and right sides of the plot, respectively.

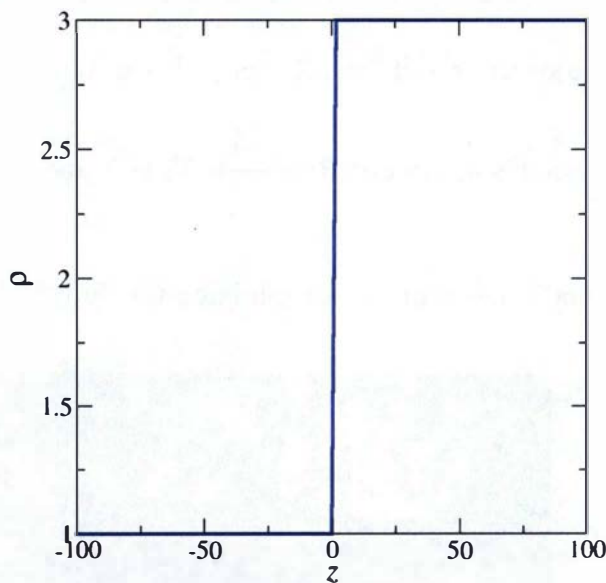
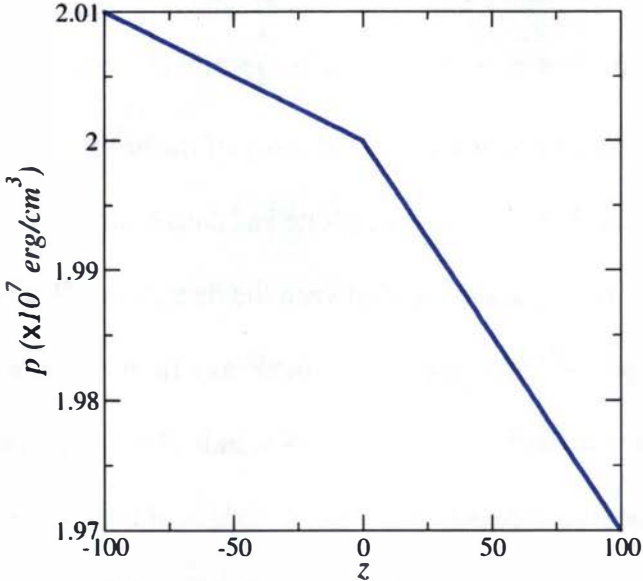


Figure 28. Initial density profile for Rayleigh-Taylor DNS.



**Figure 29. Initial pressure profile for Rayleigh-Taylor DNS.**

Calculated growth rates for the DNS and BHR2 are given in Table 3. Values from BHR2 are averaged over ten time-steps. The values for the growth rate of the mixing layer and the turbulent kinetic energy are within the error bounds and are a good match. The growth rate of the mass flux velocity for BHR2 is low compared to the DNS result. This may be an indication that better models are needed for the evolution of the mass flux velocity.

**Table 3. Asymptotic growth rates as calculated from DNS and BHR2 simulations.**

Alphas	DNS		BHR2	
	Mean	Error ( $\pm$ )	Mean	Error ( $\pm$ )
$\alpha$	0.035	0.005	0.0359	0.0007
$\alpha_k$	0.0024	0.0004	0.0026	0.0000
$\alpha_a$	0.0108	0.0007	0.0083	0.0008

Density profiles, turbulence kinetic energy, mass flux velocity and the density-specific volume correlation are shown in Figures 30 through 33, respectively. In all the

figures, the  $x$ -axis has been non-dimensionalized by the mixing width. The mixing width,  $h_{bubble+spike}$ , is defined here as  $z_{95} - z_5$ , where the  $z$  locations are the points where the mean density is equal to 5% and 95% of the initial density of the heavy fluid. The DNS values are plotted as solid lines; BHR2 values are plotted as dashed lines.

In Figure 30, a reasonable match between the density profiles is shown. The mixing layer on the spike side (the side where the heavy fluid has penetrated the light fluid) is slightly wider for BHR2 than for the DNS, indicating more mix on the light side. Additionally, the slope of the density profile at the edges of the mixing layer changes more gradually for the DNS. It may be that the model does not capture the edge effects due to diffusion adequately.

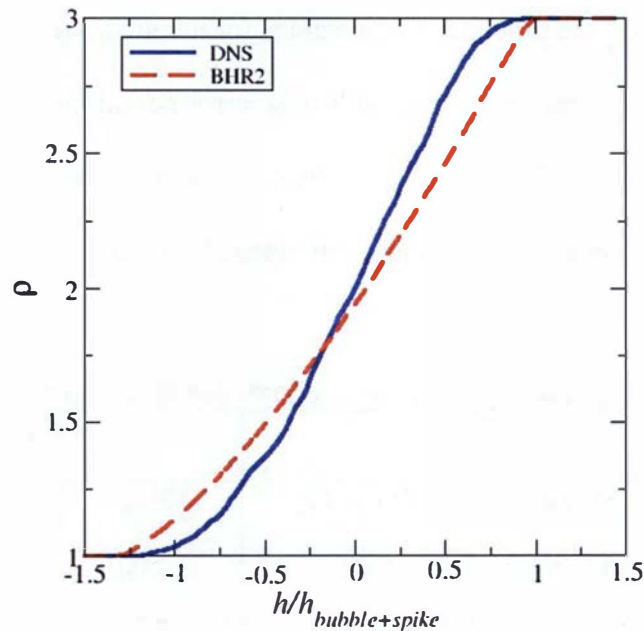


**Figure 30. Density profiles for Rayleigh-Taylor mixing layer in self-similar regime for DNS (solid) and BHR2 (dashed).**

A comparison of turbulence kinetic energies is shown in Figure 31. The turbulence kinetic energy has been non-dimensionalized by the maximum value of  $K$ . A

good match with the DNS was achieved and BHR2 has captured the shape of the profile. As previously indicated by the density profiles, greater mix, and thus a wider profile, can be observed in the figure.

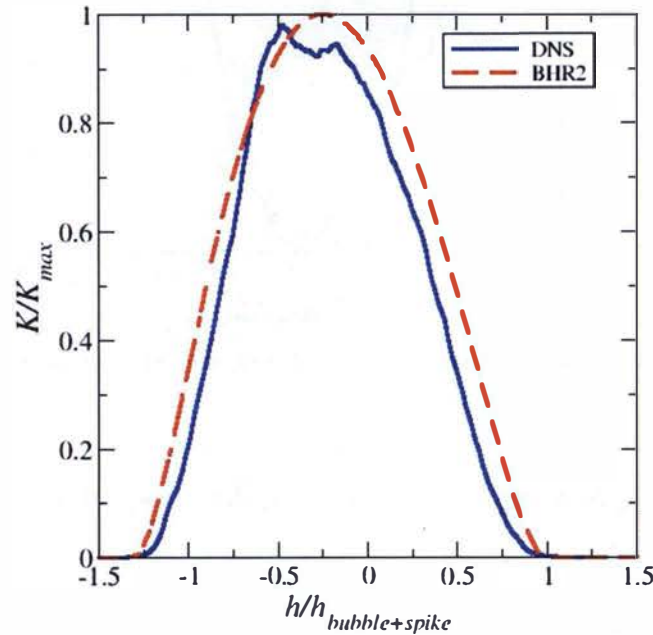


**Figure 31.** Turbulence kinetic energy for Rayleigh-Taylor mixing layer in self-similar regime for DNS (solid) and BHR2 (dashed).

The mass flux velocity is shown in Figure 32. Again, there is a good match between the DNS and BHR2. The mix model captures the shape of the curve well. A similar offset as for the previous variables is seen on the light side of the fluid.

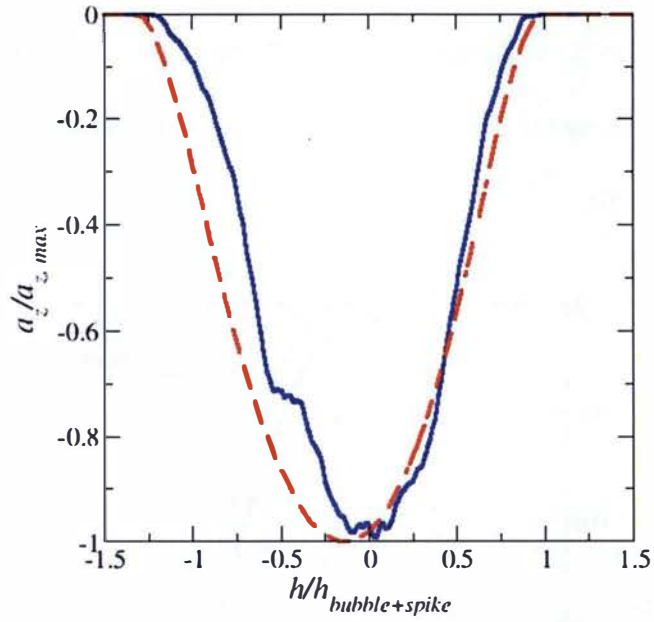


**Figure 32.** Mass flux velocity for Rayleigh-Taylor mixing layer in self-similar regime for DNS (solid) and BHR2 (dashed).

Finally, a very good match is shown for the density-specific volume correlation,  $b$ , plotted in Figure 33.

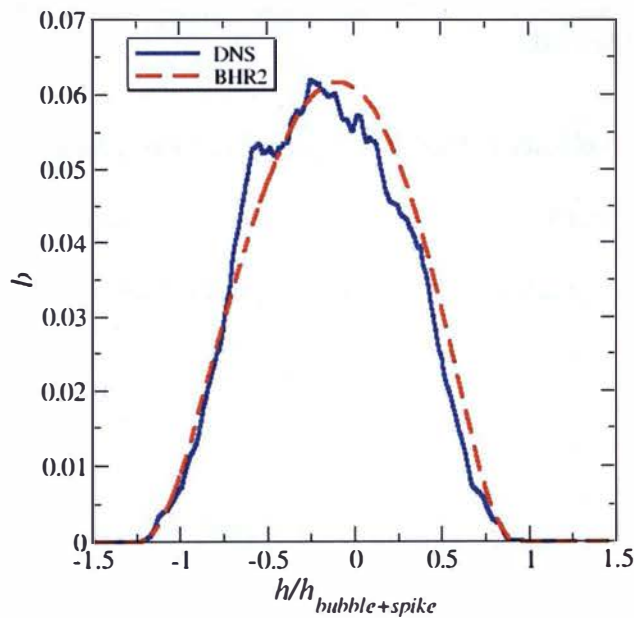


**Figure 33.** Density-specific volume correlation for Rayleigh-Taylor mixing layer in self-similar regime for DNS (solid) and BHR2 (dashed).

The magnitudes of the individual terms in the evolution equations for  $K$ ,  $\mathbf{a}$  and  $b$  for both the DNS and RAGE simulations are shown in Figures 34 though 36. The data presented for the DNS were extracted, calculated and smoothed using a moving average as the data became noisy at late times by Livescu et al. [48]. The terms from using BHR2 were calculated by the author from the RAGE simulation results. In both cases, the data was obtained at late time in the self-similar regime. The magnitude of the terms has been non-dimensionalized by the maximum value of the largest production term. The distance across the mixing layer was non-dimensionalized by the mix width. The values, from left to right, are across the mixing layer from the low-density side to the high-density side, respectively.

As the addition of the evolution of the density-specific volume correlation,  $b$ , was a primary focus of this investigation, it is presented first. The exact and modelled evolution of  $b$  are repeated below and labelled to indicate the individual advection, production, diffusion and dissipation terms that correspond to the plot in Figure 34. As a reminder, the advection and production are exact terms from the original derivation; the diffusion and dissipation are modelled. A very good match between the DNS and BHR2 results can be seen, particularly for the exact terms, as would be expected. The diffusion and dissipation terms are qualitatively correct and BHR2 does an excellent job of capturing the shapes of these terms. The magnitude of the diffusion is low and, contrarily, the values for the dissipation are high away from the edges of the mixing layer. This is an indication that there is still work to be done on the modelling of these terms, but the overall results are very promising.

$$\frac{\partial \bar{p}b}{\partial t} + \underbrace{\frac{\partial \bar{p}b \tilde{u}_n}{\partial x_n}}_{\text{Advection}} = \underbrace{2\bar{p}a_n \frac{\partial b}{\partial x_n}}_{\text{Production I}} - \underbrace{2(b+1)a_n \frac{\partial \bar{p}}{\partial x_n}}_{\text{Production II}} + \bar{p} \frac{\partial}{\partial x_n} \left[ \underbrace{\rho' \left( \frac{1}{\bar{p}} \right)' u_n'}_{\text{Turbulent transport (diffusion)}} \right] + \underbrace{2\bar{p} \left( \frac{1}{\bar{p}} \right)' \frac{\partial u_n'}{\partial x_n}}_{\text{Destruction/dissipation}}. \quad (1.95)$$

$$\frac{\partial \bar{p}b}{\partial t} + \underbrace{\frac{\partial \bar{p}b \tilde{u}_n}{\partial x_n}}_{\text{Advection}} = \underbrace{2\bar{p}a_n \frac{\partial b}{\partial x_n}}_{\text{Production I}} - \underbrace{2(b+1)a_n \frac{\partial \bar{p}}{\partial x_n}}_{\text{Production II}} + \underbrace{\bar{p}^2 \frac{\partial}{\partial x_n} \left( \frac{v_t}{\bar{p}\sigma_b} \frac{\partial b}{\partial x_n} \right)}_{\text{Diffusion}} - \underbrace{C_b \bar{p} \frac{K^{1/2}}{S}}_{\text{Dissipation}} \quad (1.96)$$

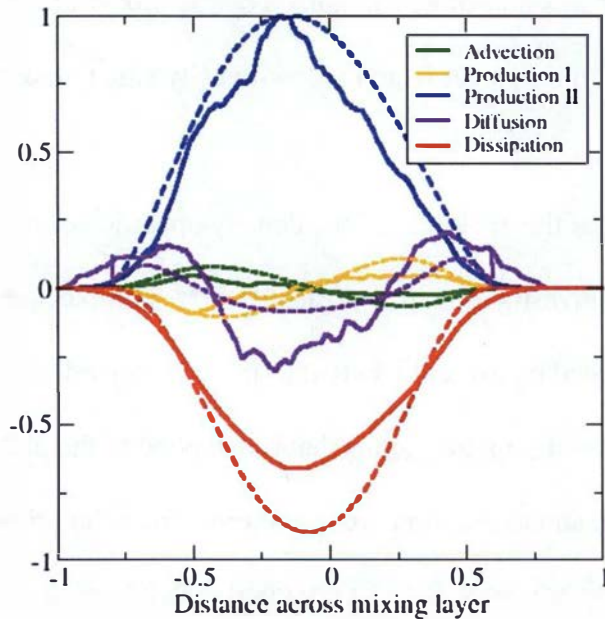


**Figure 34.** A comparison of terms in the evolution equation for  $b$  for Rayleigh-Taylor DNS (solid) and RAGE/BHR2 (dashed) simulations.

A detailed description of the terms has been previously presented by Livescu et al. in [33] for the DNS, but will be repeated briefly here for completeness. The advection and first production term lead to a redistribution of  $b$  from the heavy fluid side of the system to the light side and vice versa, respectively. The larger production term (Production II), driven by the product of the mass flux velocity and density gradient, is

shown in blue. This is the largest driver of the flow. The diffusion term in purple transports  $b$  away from the center of the mixed region and towards the edges of the layer by the large-scale structures. The dissipation term in red represents the destruction of  $b$  by molecular mixing. BHR2 additionally captures the asymmetry of the terms with respect to the centerline.

Next, the terms for the turbulence kinetic energy, or  $K$ , equation are delineated in the exact and modelled evolution equations and plotted in Figure 35. There is an excellent match between the DNS and BHR2 results. The locations of the peak values near the centerline for the larger production term, driven by the product of the mass flux and mean pressure gradient, and the dissipation term are well matched. For the diffusion term, the greater distribution of  $K$  to the heavy side is also captured. Synonymous to the advection and diffusion terms in the  $b$  equation, these similar terms in the  $K$  equation redistribute the turbulence kinetic energy within the mixing layer, from the heavy to the light side and from the interior to the edges of the layer, respectively. The shear production (Production II) transfers energy from the mean flow to turbulence on the light side and from the turbulence to the mean flow on the heavy side. The final term plotted here, the “anti-diffusion”, is not modelled separately in the BHR2 equations but it is encapsulated by the other diffusion term. It acts to transfer kinetic energy from the edges back into the interior of the mixing layer.

$$\frac{\partial \bar{P}K}{\partial t} + \frac{\partial \bar{P}K\tilde{u}_n}{\partial x_n} = \underbrace{a_n \left( \frac{\partial \bar{P}}{\partial x_n} - \frac{\partial \bar{\tau}_m}{\partial x_n} \right)}_{\text{Production I (buoyancy)}} - \underbrace{R_{in} \frac{\partial \tilde{u}_i}{\partial x_n}}_{\text{Production II (shear)}} - \underbrace{\frac{1}{2} \frac{\partial}{\partial x_n} (\rho u_i'' \tilde{u}_i'')}_{\text{Turbulent transport (diffusion)}}$$

$$-\underbrace{\frac{\partial \overline{P' u'_i}}{\partial x_i}}_{\text{Power of fluctuating pressure in fluctuating motions}} + \underbrace{\overline{P' \frac{\partial u'_i}{\partial x_i}}}_{\text{Pressure-dilatation correlation}} - \underbrace{\overline{\tau'_{ij} \frac{\partial u'_i}{\partial x_i}}}_{\text{Turbulent dissipation}} + \underbrace{\frac{\partial \overline{\tau'_{in} u'_i}}{\partial x_n}}_{\text{Power of fluctuating viscous forces in fluctuating motion (viscous dissipation)}} \quad (1.97)$$

$$\frac{\partial \overline{\rho K}}{\partial t} + \underbrace{\frac{\partial \overline{\rho K} \tilde{u}_n}{\partial x_n}}_{\text{Advection}} = \underbrace{a_n \frac{\partial \bar{P}}{\partial x_n}}_{\text{Production I}} - \underbrace{R_{in} \frac{\partial \tilde{u}_i}{\partial x_n}}_{\text{Production II}} - \underbrace{\frac{\partial}{\partial x_n} \left( \frac{\bar{\rho} v_t}{\sigma_s} \frac{\partial K}{\partial x_n} \right)}_{\text{Diffusion}} - \underbrace{\bar{\rho} \frac{K^{3/2}}{S}}_{\text{Dissipation}} \quad (1.98)$$

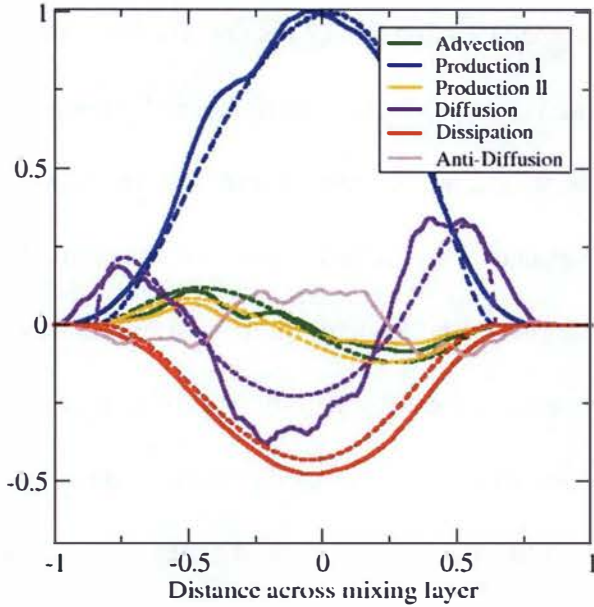


**Figure 35.** A comparison of terms in the evolution equation for turbulence kinetic energy,  $K$ , for Rayleigh-Taylor DNS (solid) and RAGE/BHR2 (dashed) simulations.

Finally, the terms for the mass flux velocity (*a*) equation are distinguished in the equations below and plotted in Figure 36. We see similar results as presented for the *b* and  $K$  equations above. Qualitatively, the shapes of the curves and the asymmetries are captured by the BHR2 model. The magnitudes of the diffusion and dissipation are somewhat out of balance and, as already noted, indicate a need to further investigate how these terms are modelled. This is being addressed through the development and

implementation of an evolution equation for the Reynolds stress tensor [43] in place of the Boussinesq approximation and/or the Ristorcelli model [46] described earlier in this report. Note that both the production terms in the equation are important to the total production of the mass flux velocity. It is common to model the mass flux velocity using a gradient diffusion approximation, which ignores the second production term. By including this term in the BHR2 model, we can do a better job of capturing the physics of the problem. As can be seen in the figure, the magnitude of this production term demonstrates that it is nearly as important as the buoyancy production and should not be treated as negligible.

$$\frac{\partial \bar{\rho} a_i}{\partial t} + \underbrace{\frac{\partial \bar{\rho} a_i \tilde{u}_n}{\partial x_n}}_{\text{Advection}} = \underbrace{-\bar{\rho} a_n \frac{\partial (\tilde{u}_i - a_i)}{\partial x_n}}_{\text{Production}} + \underbrace{\left( \frac{\cancel{\bar{\rho}' u'_i u'_n} - R_{in}}{\bar{\rho}} \right) \frac{\partial \bar{\rho}}{\partial x_n}}_{\text{Production II (shear)}} + \underbrace{\bar{\rho} \frac{\partial a_i a_n}{\partial x_n}}_{\text{Production III}} - \underbrace{\bar{\rho} u'_i \frac{\partial u'_n}{\partial x_n} - \frac{\partial \bar{\rho}' u'_i u'_n}{\partial x_n}}_{\text{Diffusion?}} \\ + b \underbrace{\left( \frac{\partial \bar{P}}{\partial x_i} - \frac{\partial \bar{\tau}_{in}}{\partial x_n} \right)}_{\text{Production I (buoyancy)}} + \underbrace{\bar{\rho} \left( \frac{1}{\rho} \right)' \frac{\partial P'}{\partial x_i} - \bar{\rho} \left( \frac{1}{\rho} \right)' \frac{\partial \tau'_{in}}{\partial x_n}}_{\text{Destruction/dissipation}}, \quad (1.99)$$

$$\frac{\partial \bar{\rho} a_i}{\partial t} + \underbrace{\frac{\partial \bar{\rho} a_i \tilde{u}_n}{\partial x_n}}_{\text{Advection}} = \underbrace{b \frac{\partial \bar{P}}{\partial x_n}}_{\text{Production I}} - \underbrace{\frac{R_{in}}{\bar{\rho}} \frac{\partial \bar{\rho}}{\partial x_n}}_{\text{Production II}} - \underbrace{\bar{\rho} a_n \frac{\partial (\tilde{u}_i - a_i)}{\partial x_n}}_{\text{Production (not plotted)}} + \underbrace{\bar{\rho} \frac{\partial a_i a_n}{\partial x_n}}_{\text{Production III}} \quad (1.100)$$

$$+ \underbrace{\frac{\partial}{\partial x_n} \left( \frac{v_t}{\bar{\rho} \sigma_a} \frac{\partial a_i}{\partial x_n} \right)}_{\text{Diffusion}} - \underbrace{C_{a1} \bar{\rho} a_i \frac{K^{1/2}}{S}}_{\text{Dissipation}}$$

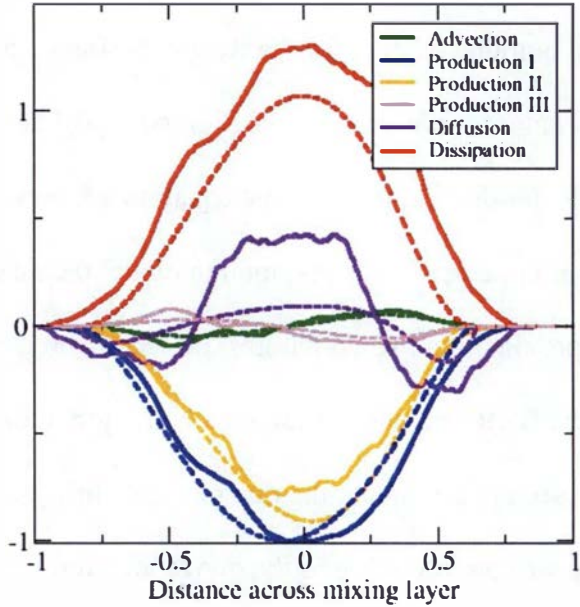


**Figure 36.** A comparison of terms in the evolution equation for mass flux velocity,  $a_z$ , for Rayleigh-Taylor DNS (solid) and RAGE/BHR2 (dashed) simulations.

#### 4.4.3 Low Atwood gas channel experiments

Next, a comparison of the BHR2 turbulence model results with the gas channel experiments of Banerjee et al. [42] is presented. These Rayleigh-Taylor experiments were performed in the air-helium gas channel facility at Texas A&M University. The experiments, combined with the DNS results presented above, provided direction for setting of the model coefficients through an iterative process, particularly  $C_4$  and  $C_b$  coefficients in the  $S$  and  $b$  equations. It was found that the value of  $C_b$  did not require retuning from the  $A = 0.5$  case, but that a different value of  $C_4$  was necessary for modelling the low Atwood number flow. This coefficient controls the growth rate of the mixing layer.

##### 4.4.3.1 Description of experiment

In these experiments, two gas streams of air and helium with an Atwood number of 0.04 are separated by a thin plate and flow parallel to each other (see Figure 37). When the

streams meet at the end of the plate, an unstable interface forms and buoyancy-driven mixing occurs as shown in Figures 38 and 39. This produces a spatially statistically steady (versus temporal) Rayleigh-Taylor flow, which allows for long periods of data collection in time. Banerjee et al. [42] were able to collect large statistical data sets to determine Reynolds stresses, mix profiles, velocity-density correlations and measures of molecular mixing; thus, they were able to obtain profiles for mean density, turbulence kinetic energy, mass flux velocity and the density-specific volume correlation. To the best of our knowledge, these are the first Rayleigh-Taylor experiments to capture and measure this type of information.

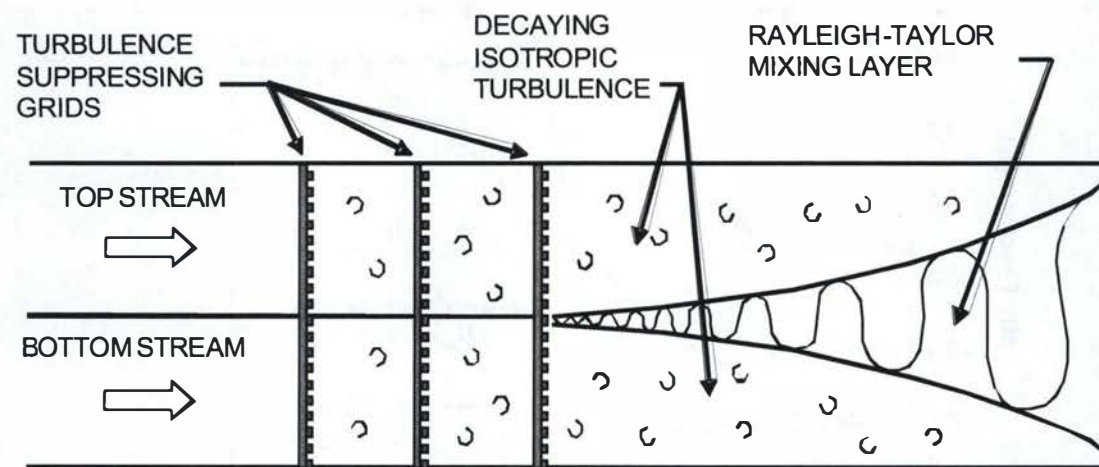


**Figure 37. Illustration of Texas A&M University RT gas channel experiment [79].**

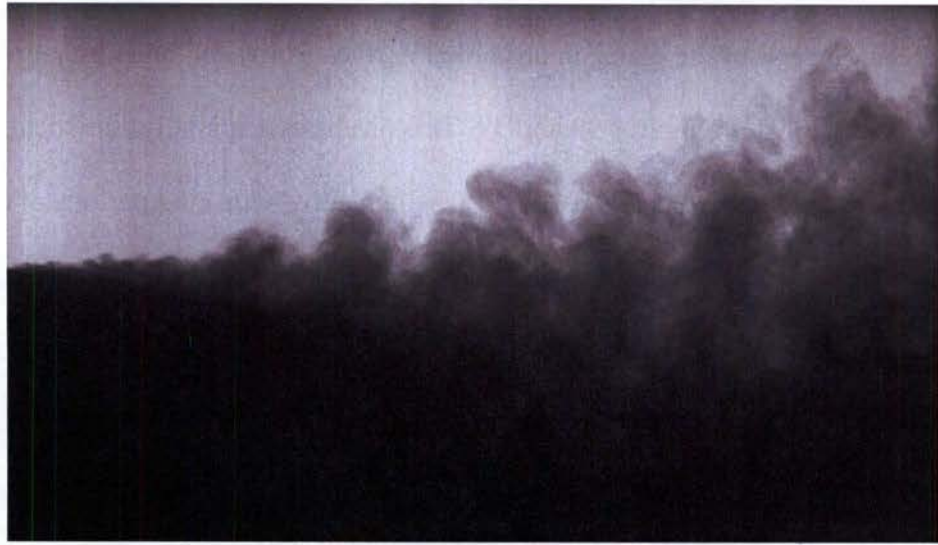


Figure 38. Photograph of Texas A&M University RT gas channel experiment [80].

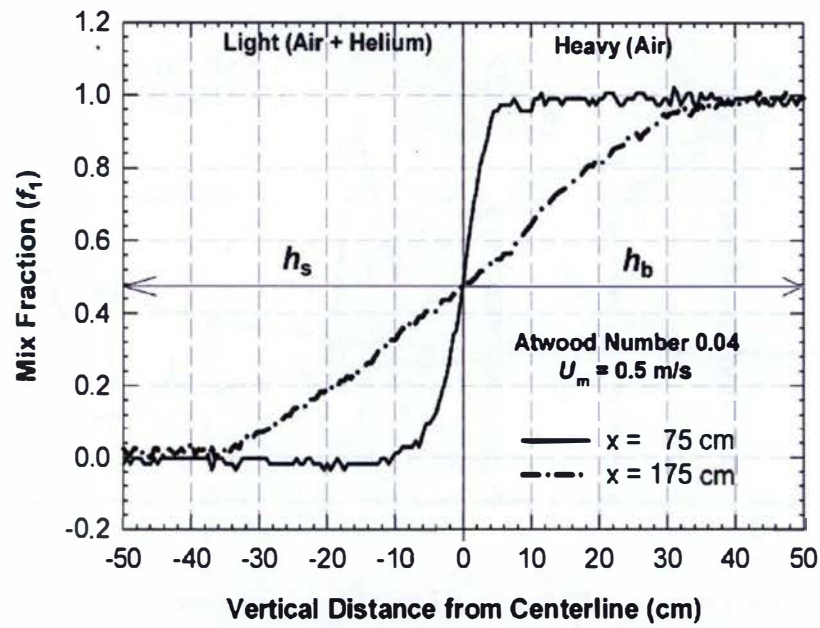


Figure 39. Mix fractions for Texas A&M University RT gas channel experiments [80].

#### 4.4.3.2      *Simulation details*

The simulations of the gas channel experiment were performed using a similar setup to the mid-range Atwood Rayleigh-Taylor simulations in RAGE presented in the previous section. Adjustments were made to the density to account for the lower Atwood number.

It also was necessary to increase the simulation time and domain size because the low Atwood flow took longer to reach self-similar conditions. With respect to cell size and temperature, the same hydro initialization was used. Likewise, the same values of  $K_0$  and  $S_0$  were used for initializing the turbulence model. One necessary adjustment was required with respect to  $b$ . Due to the smaller density fluctuations associated with this flow, the cutoff value was reduced to  $b_{CUTOFF} = 1e-16$ .

#### 4.4.3.3 *Comparison of results between experiment and BHR2*

Results from the experiment and BHR2 for scaled profiles of mean density, turbulent kinetic energy, mass flux velocity and density-specific volume correlation are shown in Figures 40 through 43. In Figure 40, there is excellent agreement between the data and simulated values of the density profile. In Figure 41, the turbulence kinetic energy exhibits a parabolic profile, peaking close to the centerline of the mixing layer. The RAGE simulation captures the profile fairly well, though the curve peaks lower than the experimental values and a narrower profile is produced. Likewise, for the mass flux in Figure 42, the model captures the parabolic profile fairly well, but the simulated values are low and produce a narrower profile than the experimental results. The comparison for the density-specific volume correlation is shown in Figure 43. The simulated values fall outside of the range of the experimental values, but overall capture the correct shape of the profile. On the whole, the BHR2 results are considered to show good agreement with the experiment.

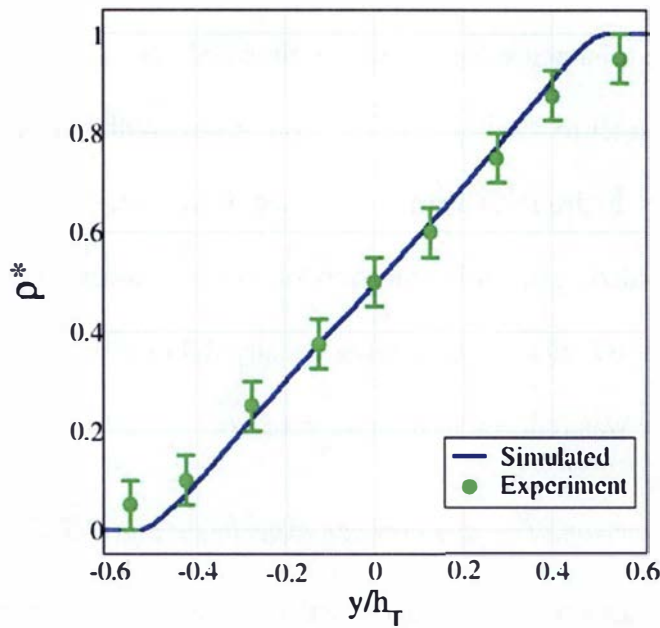


**Figure 40.** A comparison of experimental results and RAGE simulations using BHR2: Scaled mean density as a function of location across the mixing layer. Location is non-dimensionalized by total mixing width.

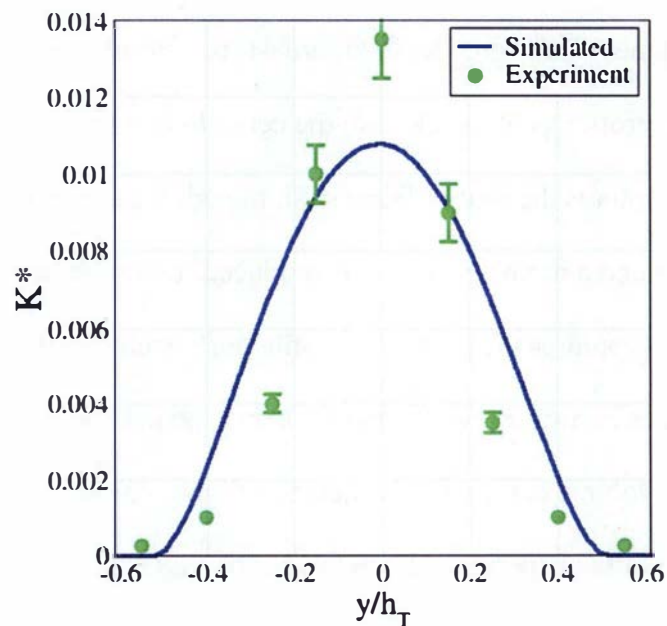


**Figure 41.** A comparison of experimental results and RAGE simulations using BHR2: Scaled turbulent kinetic energy as a function of location across the mixing layer. Location is non-dimensionalized by total mixing width.

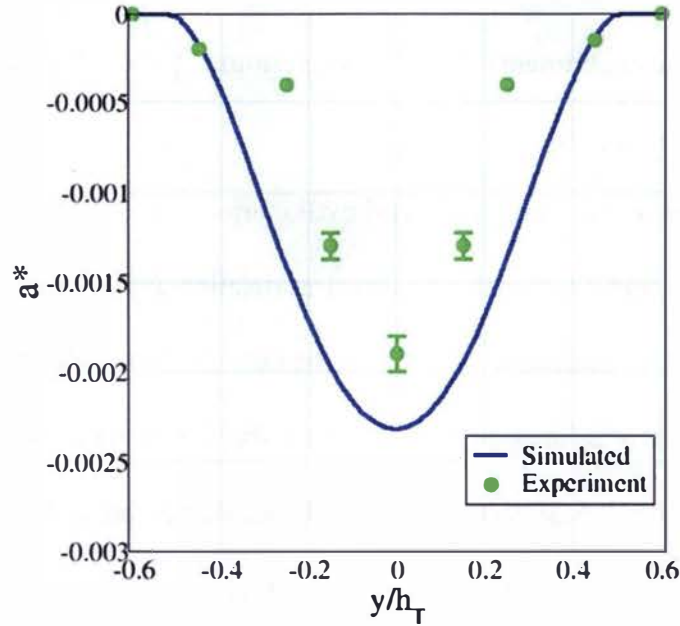


**Figure 42.** A comparison of experimental results and RAGE simulations using BHR2: Scaled mass flux velocity as a function of location across the mixing layer. Location is non-dimensionalized by total mixing width.

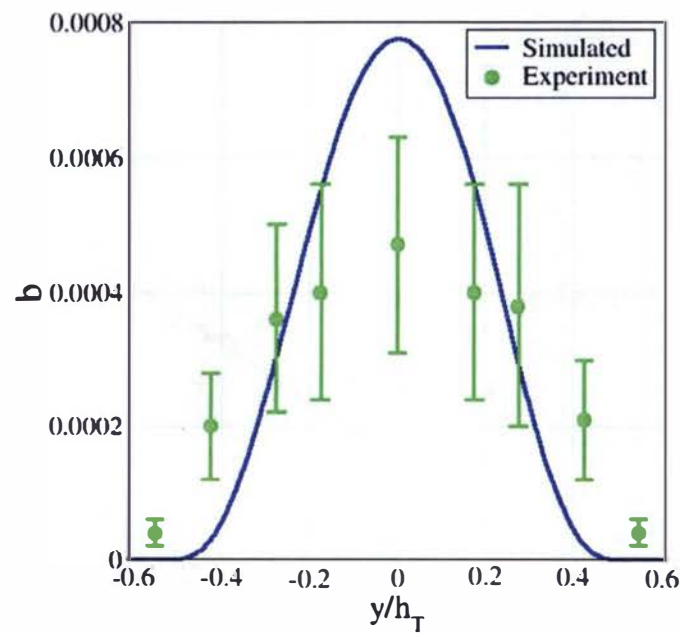


**Figure 43.** A comparison of experimental results and RAGE simulations using BHR2: Density-specific volume correlation as a function of location across the mixing layer. Location is non-dimensionalized by total mixing width.

The final measure of comparison for this case was the asymptotic growth rate of the mix width,  $\alpha$ . The experimental value was determined to be 0.14. This matched well with the simulated value of 0.13.

Similar experiments were performed by Banerjee et al. [42] for Atwood numbers of 0.097, 0.259, 0.47 and 0.6. For these cases, less detailed data was available than for the  $A = 0.04$  case, but it was possible to compare the growth rates of the mix layers. In Figure 44,  $\alpha$  is plotted as a function of Atwood number for both the experiments (red) and the BHR2 model in RAGE (blue). The calculated values fall within the error bars of the measured values. There is a decrease in the data from  $A = 0.04$  to  $A = 0.097$  and then an increase again, a trend that also is captured by the model. At this time, we have no explanation for this behaviour.

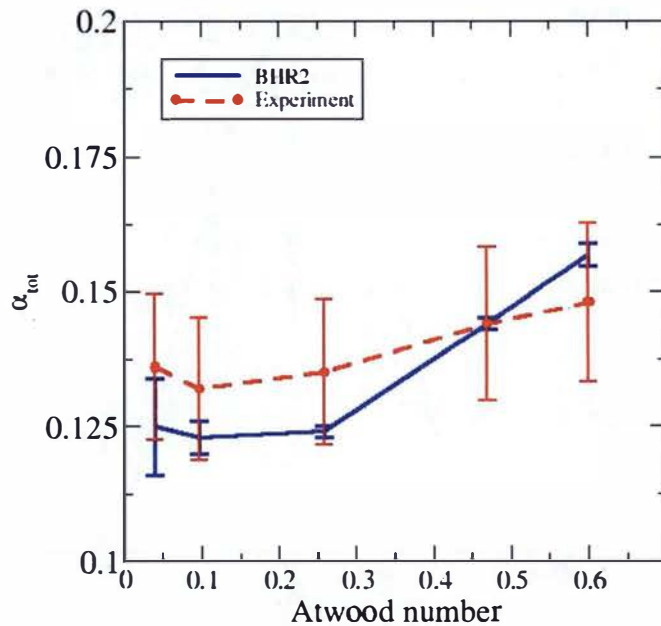


**Figure 44. Growth rate as a function of Atwood number for the Texas A&M RT experiments [42].**

#### *4.4.4 Rocket Rig experiments*

The original “rocket rig”, shown in Figures 45 through 47 was developed by Read [15] at the Atomic Weapons Establishment (AWE) to study the growth of Rayleigh-Taylor instabilities in fluids. The experiments were expanded by Burrows [81], Smeeton et al. [16] and Youngs [17] to include a wide variety of fluid combinations. The cases included two-fluid and three-fluid experiments, a tilted rig, high acceleration and acceleration-deceleration-coast (RT-unstable to RT stable) conditions. Here, we present mostly qualitative results for the acceleration-deceleration-coast experiment in order to more clearly show the effects of evolving  $b$  in variable-density flows.

##### *4.4.4.1 Description of experiment*

In this experiment, two fluids were contained in a rectangular tank in which the light fluid sat atop the heavy fluid. Rocket motors were attached to the top of the tank and used to drive the tank vertically downwards. This acceleration caused the system to become Rayleigh-Taylor unstable and the mixing layer to grow (see Figures 45 though 48). The experiment was extended by Smeeton and Youngs [16] such that when the motors died out, the tank was decelerated by springs. Here, partial demix of the fluids occurred and there was a decrease in the mix width as shown in Figure 48. Then the tank changed direction and coasted vertically upward at a near constant velocity. In this final stage, the system was RT stable again and slow growth of the mix layer due to turbulent diffusion effects was observed.

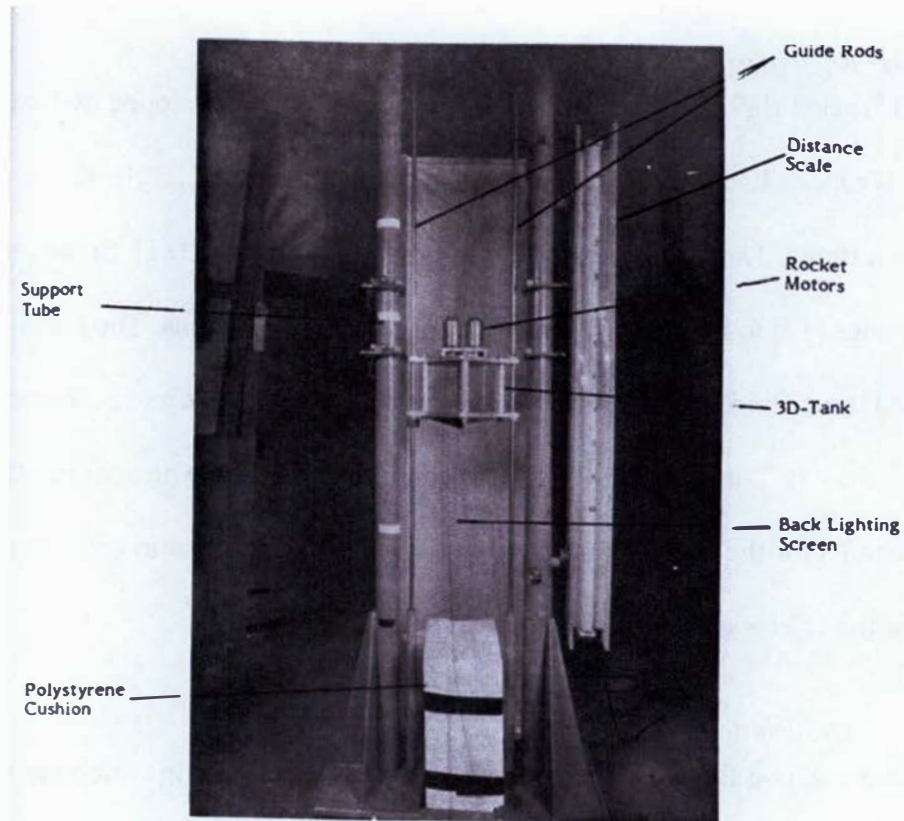
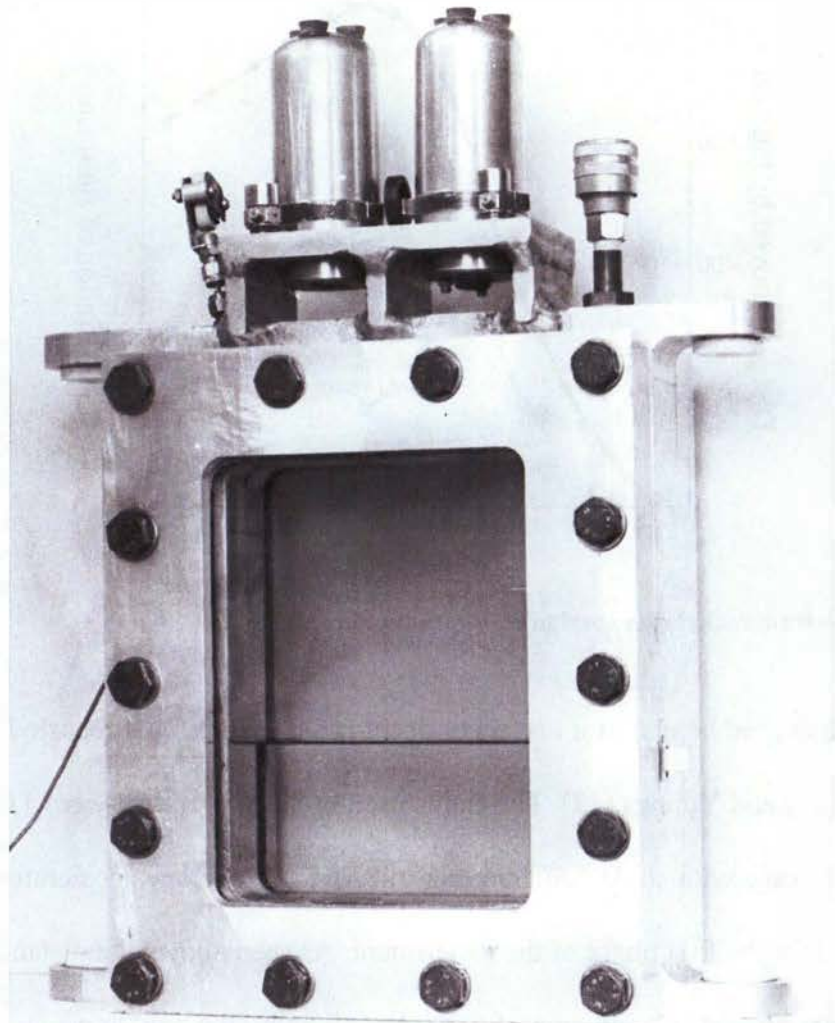
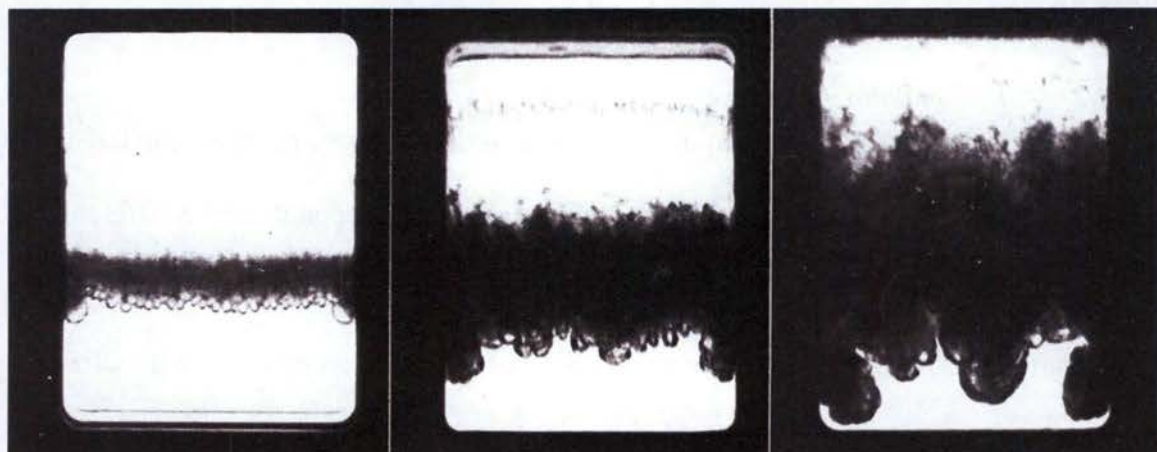


Figure 45. The "rocket rig" experimental apparatus [16].



**Figure 46.** Tank in rocket rig experiment [16]. Provided by D. Youngs.



**Figure 47.** Pictures of Rayleigh-Taylor mixing layers from rocket rig experiment [16].

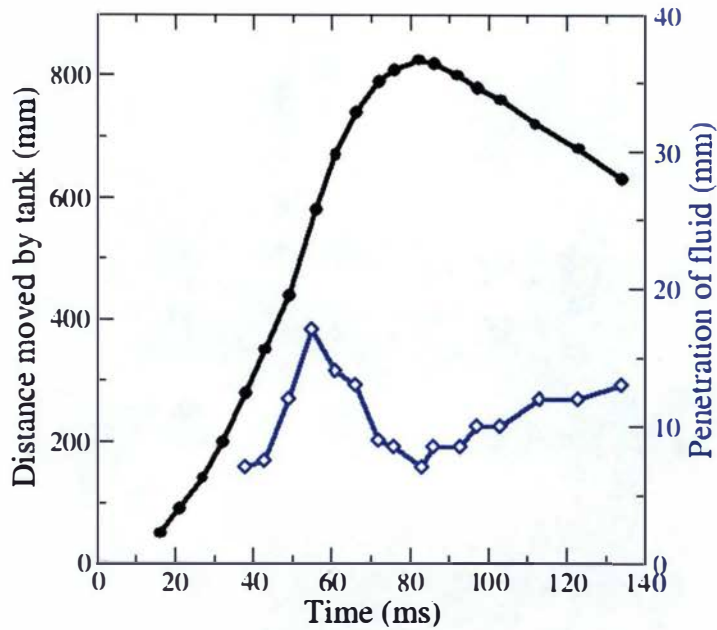


**Figure 48. Data from rocket rig experiment.** Reproduced from [16].

The data used here are for an “accel-decel-coast” experiment reported by Smeeton and Youngs [16] and Youngs [17]. The fluids used in the experiment were a  $\text{CaCl}_2$  solution and hexane with an Atwood number of 0.267. An average acceleration of  $32g$  was measured for the first phase of the experiment. As seen above, the distance travelled by the tank was plotted as a function of time. Additionally, the bubble penetration depth was plotted. Bubble penetration depth was measured to the point of 95% of the volume fraction.

#### 4.4.4.2        *Simulation details*

RAGE simulations were performed using a similar setup as for the previous Rayleigh-Taylor simulations. Adjustments were made to the density to account for the different Atwood number,  $A = 0.267$ . With respect to cell size and temperature, the same hydro initialization was used. Likewise, the same values of  $K_0$  and  $S_0$  were used for initializing the turbulence model. A constant acceleration of  $32,340 \text{ cm/s}^2$  was applied for the first

stage of the simulation. A time-dependent deceleration, roughly calculated from the plot in Figure 48, was specified for the second two stages of the simulation.

#### 4.4.4.3 BHR2 simulation results

Results showing the mixing widths and  $b$  are given in Figures 49 and 50, respectively.

The  $x$ -axes are normalized using the time that the direction of the acceleration was changed, or flipped. The mix widths on the  $y$ -axis in Figure 49 were normalized by the mix width, also at the time the direction of the acceleration was reversed.

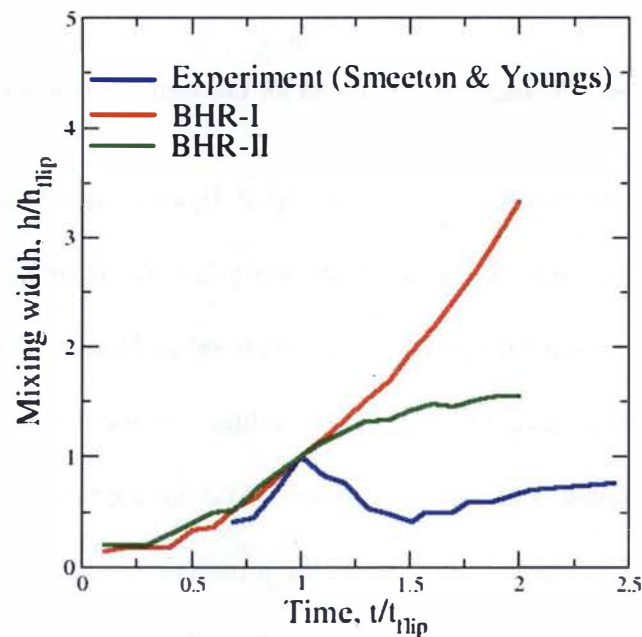


**Figure 49. Experimental and calculated mixing widths using BHR and BHR2 for the accel-decel coast experiment.**

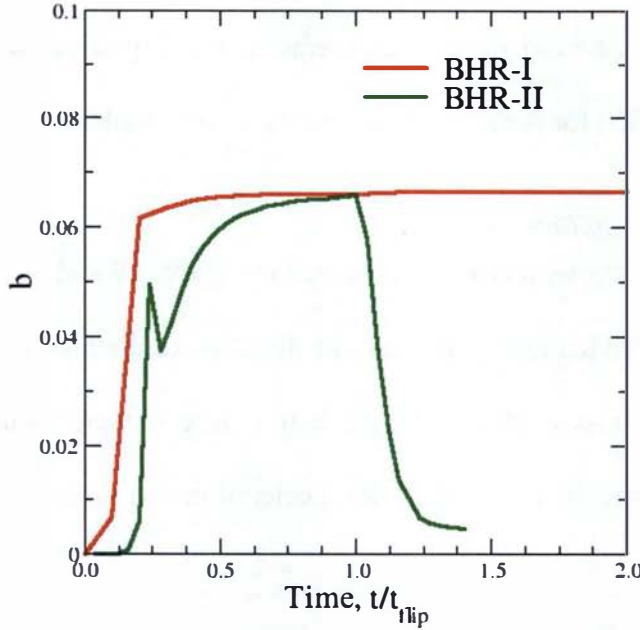


**Figure 50. Calculated values of  $b$  using BHR and BHR2 for the accel-decel-coast experiment.**

For the original implementation of BHR (BHR-I), an issue with the physics used to model  $b$  is observed. As seen in Figure 50, the analytic solution of  $b$  using BHR increases as the fluids mix until it reaches a maximum value. However, when the direction of the acceleration changes, the analytic solution cannot capture the new physics. It can only remain a constant and continues to drive the production of the mass flux velocity in Eqn. 1.72, which in turn drives the production of the turbulent kinetic energy. Thus, energy continues to feed the turbulence and the mixing layer continues to grow as shown in red in Figure 49.

For BHR2, a dramatic difference can be seen in Figure 50. During the unstable RT phase, as for BHR,  $b$  increases as the mixing occurs. When the direction of the acceleration switches, the evolution equation for  $b$  is able to capture the change, and decreases as the system returns to stable RT flow, such that the mixing slows. This is reflected in the slowing of the growth of the mixing width in Figure 49. The model is not

able to match the portion of the curve where the mix width decreases due to demix. This is because the species equation only allows for diffusion.

Preliminary work was performed for by implementing a species equation which allows for demix between two fluids:

$$\frac{\partial \bar{p}c^1}{\partial t} + \frac{\partial \bar{p}c^1 \tilde{u}_y}{\partial y} = - \left( \frac{\rho_1 \rho_2}{\rho_2 - \rho_1} \right) \frac{\partial a_y}{\partial y} \quad (1.101)$$

and

$$\frac{\partial \bar{p}c^2}{\partial t} + \frac{\partial \bar{p}c^2 \tilde{u}_y}{\partial y} = - \left( \frac{\rho_1 \rho_2}{\rho_1 - \rho_2} \right) \frac{\partial a_y}{\partial y}. \quad (1.102)$$

Initial results are promising, capturing the decrease in mix width due to demix, as shown in Figure 51, though they do not correctly calculate the growth rates. Regions seen experimentally are observed qualitatively. We see the initial growth of the mix width due to the downward acceleration of the rig. Immediately after the gravity is switched, inertial growth occurs. Then, there is “de-mixing” for ~20 ms before slow growth due to turbulent diffusion effects is observed at late time.

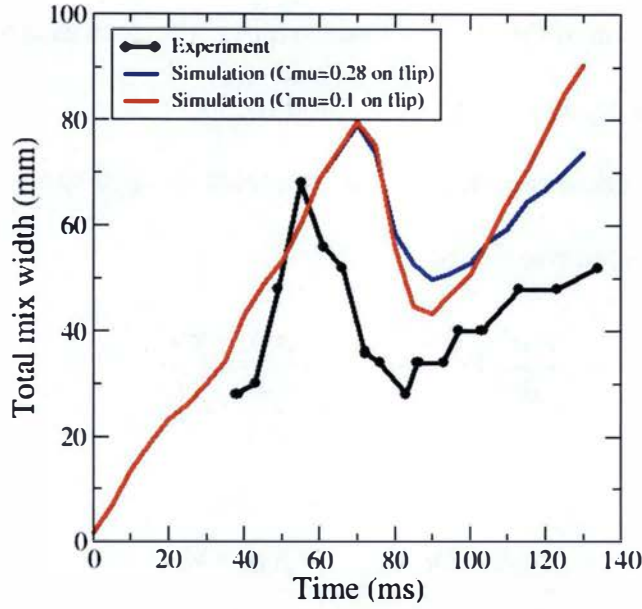


**Figure 51.** Total mix width as a function of time for the rocket rig "accel-decel-coast" experiment [15, 16, 17]. Red and blues lines are from RAGE simulations using BHR2 with the modified species equation.

#### 4.4.5 Linear Electric Motor (LEM) experiments

The Linear Electric Motor (LEM) experiments of Dimonte and Schneider [76] were Rayleigh-Taylor experiments performed for  $0.15 \leq A \leq 0.96$  with different acceleration histories. Data obtained from the experiments included volume fraction profiles and bubble and spike amplitudes from which the growth rate,  $\alpha$ , of the mixing layer was deduced. The results for  $\alpha$  are compared with BHR2 results using the standard model coefficients.

##### 4.4.5.1 Description of experiment

In the experimental setup, a sealed plastic container, holding the fluids of interest was accelerated along rails. The acceleration was controlled by an electromagnetic force, which was applied by two armatures that slid along two pairs of rails that acted as linear electrodes. The container had two spring-loaded armatures on top to complete the rail circuit and brake pads on the sides. The assembly was decelerated with spring-loaded

brakes. For a detailed description of the experimental configuration, including dimensions, please see [76].

As previously stated, the experiments were performed across a range of Atwood numbers, from 0.15 up to 0.96. Several fluids were used in a variety of combinations. The fluids included: water, Freon, decane, water/KI, water/NaCl, water/NaI, hexane, liquid metal, butane and SF<sub>6</sub>. The fluids are immiscible and relatively inviscid. They are also relatively clear, which allowed for better visibility of bubbles and spikes.

The fluids were stacked in the plastic container, with the light fluid on top. The container was then accelerated downward to generate Raleigh-Taylor turbulence at the interface between the two fluids. Experiments were performed for constant, variable and impulsive accelerations. The results shown here are for the constant acceleration case.

#### 4.4.5.2 *Comparison of computational to experimental results*

Results comparing the experimental  $\alpha$  values calculated using the BHR2 model in RTI3D and in RAGE are shown in Figure 52 as a function of Atwood number. The experimental values include LEM data, the Rocket Rig data of Youngs [17] described in the previous section, and the Texas A&M gas channel data [42]. The black lines/data are for the growth of the bubble, the red lines are the growth of the spike and the blue lines give the total growth rate of the mixing layer. For low Atwood numbers, the simulated values fall below the experimental data. The match improves at Atwood numbers between 0.3 and 0.8. At high Atwood numbers, the simulated values for the spikes are in good agreement, but are much lower than the data for the bubble.

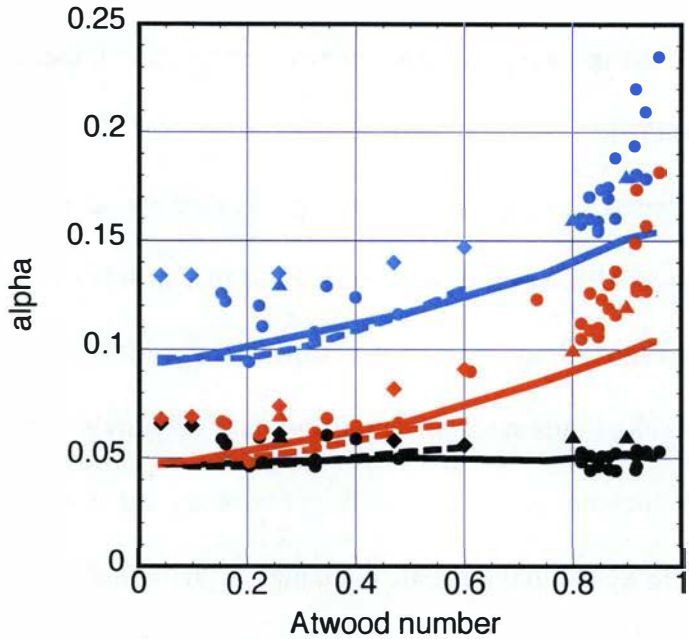


**Figure 52.** Growth rate as a function of Atwood number for LEM [76], gas channel [42] and rocket rig [17] experiments compared with BHR2 results calculated using RAGE and RTI3D. The dashed lines are from RAGE calculations; solid lines are from RTI3D calculations. Circles, diamonds and triangles represent the LEM, gas channel and rocket rig data, respectively.

There were issues associated with the LEM and rocket rig experiments that should be mentioned. First, the growth rates recorded for the LEM at high Atwood numbers and for the rocket rig experiments were based on visual interpretation of pictures used to record the mixing. Second, the growth rates at low Atwood numbers for the LEM were determined by calculating the mean slope of the growth of the mixing width, however, there were large variations in the values used in this averaging.

#### 4.4.6 Self-Similar analysis for low Atwood RT

The use of simplifying equations based on assumptions that may be specifically, but never universally, approximate was initially presented by Tennekes and Lumley [9], and can be found for Rayleigh-Taylor turbulence in Andrews [24] and Lohr [82]. Here, we present a similar analysis for BHR2 under the simplifying assumptions of low Atwood number and late time self-similar behaviour. The motivation for this analysis was to:

1. Potentially inform a starting point for the BHR2 coefficients. Note, this practical analysis occurred after setting of the coefficients using DNS and experimental results.
2. Demonstrate characteristics of self-similarity.
3. Provide order of magnitude estimates for individual terms to help better understand the physics, albeit for simplified equations under simplified conditions.

Assuming a one-dimensional, low Atwood number Rayleigh-Taylor flow, the BHR2 model equations can be simplified. The base model equations reduce to:

$$\frac{DK}{Dt} = \frac{a}{\rho} \frac{dP}{dx} + \frac{1}{\rho} \left( \frac{\rho v_T}{\sigma_K} \frac{dK}{dx} \right) - \frac{K^{3/2}}{S}, \quad (1.103)$$

$$\frac{Da}{Dt} = \frac{b}{\rho} \frac{dP}{dx} - \frac{R_{22}}{\rho^2} \frac{d\rho}{dx} + \frac{1}{\rho} \left( \frac{\rho v_T}{\sigma_a} \frac{da}{dx} \right) - \frac{C_{a1} K^{1/2} a}{S}, \quad (1.104)$$

$$\frac{Db}{Dt} = -\frac{2(b+1)a}{\rho} \frac{d\rho}{dx} + \left( \frac{v_T}{\sigma_K} \frac{d^2 b}{dx^2} \right) - \frac{C_b K^{1/2} b}{S} \quad (1.105)$$

and

$$\frac{DS}{Dt} = (3/2 - C_4) \frac{S}{K} \frac{a}{\rho} \frac{dP}{dx} + \frac{1}{\rho} \left( \frac{\rho v_T}{\sigma_S} \frac{dS}{dx} \right) - (3/2 - C_2) \sqrt{K}. \quad (1.106)$$

Next, assumptions are made about the shape of the self-similar forms of the variables. These shapes will be demonstrated later, but for now, we only present the equations:

$$K = K_{MAX} (1 - (y/h)^2), \quad (1.107)$$

$$K_{MAX} = \alpha_K (Agt)^2 \quad (1.108)$$

$$a = a_{MAX}(1 - (y/h)^2), \quad (1.109)$$

$$\alpha_{MAX} = \alpha_a(Agt), \quad (1.110)$$

$$b_{MAX} = \text{constant}, \quad (1.111)$$

$$b = b_{MAX}(1 - (y/h)^2), \quad (1.112)$$

$$S = S_{MAX}(1 - (y/h)^2)^{0.2}, \quad (1.113)$$

and

$$S_{MAX} = \alpha_s Agt^2. \quad (1.114)$$

Substituting these relationships into the reduced equations, the equation for turbulence kinetic energy,  $K$ , becomes

$$1 = -\frac{\alpha_a}{2\alpha_K A} - \frac{4C_\mu \sqrt{\alpha_K} \alpha_s}{\sigma_K \alpha^2} - \frac{\sqrt{\alpha_K}}{\alpha_s}; \quad (1.115)$$

the equation for mass flux velocity,  $a$ , becomes

$$1 = -\frac{b_{MAX}}{A\alpha_a} - \frac{4A\alpha_K}{3\alpha_a \alpha} - \frac{8C_\mu \sqrt{\alpha_K} \alpha_s}{\sigma_a \alpha^2} - \frac{C_{a1} \sqrt{\alpha_K}}{\alpha_s}; \quad (1.116)$$

the density-specific volume correlation,  $b$ , becomes

$$0 = -\frac{2\alpha_a A}{\alpha} - \frac{8C_\mu \sqrt{\alpha_K} \alpha_s b_{MAX}}{\sigma_b \alpha^2} - \frac{C_{b2} \sqrt{\alpha_K} b_{MAX}}{\alpha_s}; \quad (1.117)$$

and the turbulence length scale,  $S$ , becomes

$$1 = -\frac{(3/2 - C_4)\alpha_a}{2\alpha_K A} - \frac{0.8C_\mu \sqrt{\alpha_K} \alpha_s}{\alpha^2} - \frac{(3/2 - C_2)\sqrt{\alpha_K}}{2\alpha_s}. \quad (1.118)$$

The asymptotic growth rates,  $\alpha$ ,  $\alpha_K$ ,  $\alpha_a$  and  $\alpha_s$ , were described previously in Section 4.4.1. Because the approximations above are for low Atwood flows, the advection has been neglected in each equation.

For the species equation, this results in a balance between advection and diffusion. Beginning with the base equation,

$$\frac{\partial \bar{\rho}c^k}{\partial t} + \frac{\partial \bar{\rho}c^k \tilde{u}_n}{\partial x_n} = \frac{\partial}{\partial x_n} \left( \frac{\rho v_t}{\sigma_c} \frac{\partial \bar{\rho}c^k}{\partial x_n} \right), \quad (1.119)$$

we perform differentiation by parts using  $\tilde{u} = a$ . Assuming  $\partial(\ )/\partial x = 0$  at the centerline, except for the density and species concentration, this produces,

$$\rho a \frac{\partial c^k}{\partial x} + ac^k \frac{\partial \rho}{\partial x} = \left( \frac{C_\mu}{\sigma_c} \right) S \sqrt{K} \frac{\partial c^k}{\partial x} \frac{\partial \rho}{\partial x}. \quad (1.120)$$

Applying the above self-similar forms for  $K$ ,  $S$  and  $a$ , and assuming a linear profile for  $c$  and  $\rho$ , gives

$$1 + A = \left( \frac{C_\mu}{\sigma_c} \right) \frac{\alpha_s}{\alpha} \frac{2A\sqrt{\alpha_K}}{\alpha_a}. \quad (1.121)$$

In this case, the advection term is kept simply to illustrate the Atwood number dependence of the term. Each of these equations can be used to estimate the relative magnitude of the production, diffusion and dissipation terms for each variable, albeit not exact, which will be demonstrated here.

Consider the problem given in Table 4; except for  $\alpha_s$ , these values were determined from the RT low Atwood number gas channel experiments of Banerjee et al. [42].

**Table 4. Example problem.**

Variable	Value
A	0.04
$\alpha$	0.096
$\alpha_K$	0.0084
$\alpha_a$	0.0017
$\alpha_s$	$0.7\alpha$
$b_{MAX}$	0.0006

If we substitute the appropriate values for the turbulence kinetic energy in Eqn. (1.115), the equation gives  $1 \approx 2.50 - 0.77 - 0.67$ . This can be interpreted loosely as the unit rate of change in  $K$  at the centerline is approximately equal to 2.5 units of production less 0.8 units of diffusion and 0.7 units of dissipation. Also, for the self-similar regime of the low Atwood flow, the ratio of RT production to dissipation is  $2.5/0.7 = 3.6$ . Due to the approximate nature of the above expressions, the right-hand side of the equation does not sum exactly to one. Note, using a different method for defining the mix width, say 1% volume fraction versus the 5% mass fraction used here, gives slightly different values. The real balance only is achieved using the actual terms throughout the entire mixing layer, as was done for the DNS comparisons.

Continuing to the mass flux velocity and again substituting in the appropriate values, Eqn. (1.116) gives  $1 \approx 9 + 2 - 2 - 8$ . The unit rate of change in  $a$  occurs due to 11 units of production less 2 units of diffusion and 8 units of dissipation. As noted in the previous section, the balance of production terms is not correct due to the assumption of isotropic Reynolds stress. However, the ratio of *total* production to dissipation is  $11/8 = 1.4$ , i.e., though the ratio of “production 1” to “production 2” is not quite correct, the calculation of the total production is reasonable.

For the turbulent length scale, Eqn. (1.118) gives  $1 \approx 1.9 - 1.4 + 0.5$ . The ratio of production to dissipation is 3.8.

Because  $b_{MAX}$  is nearly constant in the self-similar state, the evolution equation for the density-specific volume correlation is perhaps the most interesting. For  $b$ , Eqn. (1.117) gives  $0 \approx 0.0014 - 0.0003 - 0.002$ , or  $0 \approx 1 - 0.2 - 1.4$ . The ratio of

production to dissipation is 0.7, such that there is nearly a balance between production and dissipation with little diffusion. Again, there is an imbalance between the two sides of the equations due to the approximate nature of these self-similar relationships.

In the transport of species, Eqn. (1.121) gives  $1 + 0.04 \approx 1.4$ , such that the first term of the left-hand side is balanced by the diffusion. Interestingly, if the advection term in Eqn. (1.120) is neglected, similar to the equations for  $K$ ,  $\mathbf{a}$ ,  $b$  and  $S$ , the species equation reduces to

$$\bar{\rho}a = \left( \frac{C_\mu}{\sigma_c} \right) S \sqrt{K} \frac{\partial \bar{\rho}}{\partial x}. \quad (1.122)$$

This does not imply that  $\mathbf{a}$  can be written as a function of the density gradient, but that modelling  $\mathbf{a}$  correctly is essential for calculating the density gradient accurately in this simple case of low Atwood steady-state RT.

Even though the self-similar analysis consists of approximations, the expressions also can be used for establishing the mix model coefficients. There are limitations due to the incompleteness of the data, but some results will be presented that illustrate useful trends and other essential information.

Neglecting the diffusion in  $b$ , we can rearrange Eqn. (1.117) such that,

$$C_b = -\frac{\alpha_s}{\alpha} \frac{\alpha_a}{\sqrt{\alpha}} \frac{2A}{b_{MAX}}. \quad (1.123)$$

Similarly, for the  $K$ ,  $\mathbf{a}$ ,  $S$  and species equations, we can rearrange Eqns. (1.115), (1.116) and (1.118) to obtain the following expressions, respectively:

$$C_\mu = \frac{\alpha^2}{4\alpha_s \sqrt{\alpha_K}} \left( 1 + \frac{\alpha_a}{2A\alpha_K} + \frac{\sqrt{\alpha_K}}{2\alpha_s} \right), \quad (1.124)$$

$$C_{a1} = \frac{\alpha_s}{\sqrt{\alpha_K}} \left( 1 + \frac{b_{MAX}}{A\alpha_a} + \frac{4A\alpha_K}{3\alpha\alpha_a} + \frac{8C_\mu\alpha_s\sqrt{\alpha_K}}{\alpha^2} \right), \quad (1.125)$$

$$C_4 = 3/2 + \frac{2A\alpha_K}{\alpha} \left( 1 - \frac{0.42\sqrt{\alpha_K}}{\alpha_s} + \frac{8C_\mu\sqrt{\alpha_K}}{2\alpha_s} \right) \quad (1.126)$$

and

$$\frac{C_\mu}{\sigma_c} = \frac{1}{2A} \frac{\alpha}{\alpha_s} \frac{\alpha_a}{\sqrt{\alpha_K}}. \quad (1.127)$$

Substituting the experimental values from Table 4 and the coefficients shown in Table 5,

**Table 5. Model coefficients.**

Model Coefficient	Value
$\sigma_b$	3.0
$\sigma_f$	0.1
$\sigma_K$	1.0
$\sigma_a$	1.0

produces a value of  $C_b = 2.1$ . This can be compared to the optimized value of 2.5 determined from matching the model calculations with the DNS and experimental values presented in earlier sections. Similarly, one can calculate the values for the remaining coefficients. These are given in Table 6.

**Table 6. Model coefficients.**

Coefficient	Value	
	Self-similarity Analysis	Calibration to DNS and Experiment
$C_b$	2.1	2.5
$C_u$	0.32	0.28
$C_{a1}$	5.2	6.0
$C_4$	0.42	0.65
$\sigma_c$	1.0	0.6

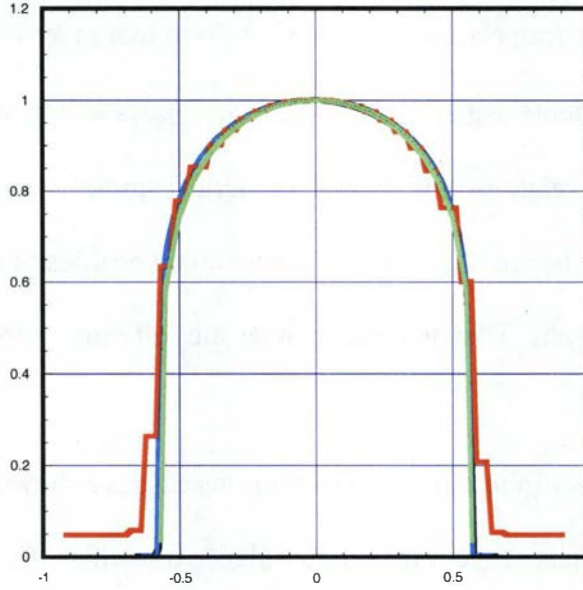
As mentioned above, the coefficients were set primarily by optimization to the Cabot and Cook DNS [25], but the comparison using the different approaches is interesting.

These equations can also be rewritten in a form that gives the growth rates as a function of the coefficients, e.g.,  $\alpha = f(C_b, C_\mu, C_{al}, C_4)$ . As will be demonstrated later, we chose to explore these relationships through numerical studies. This is because some of the coefficient values change the shapes of the assumed profiles of the variables used in the self-similarity analysis. This, in turn, changes the self-similar forms of the equations given above.

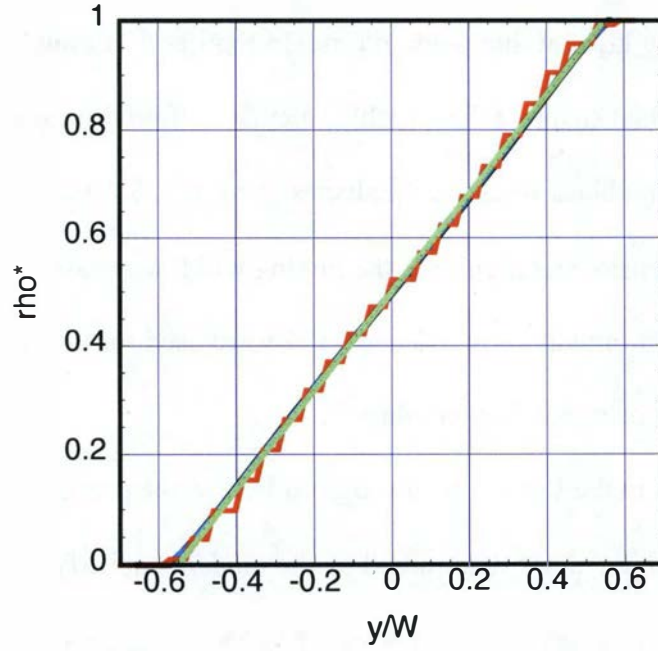
Demonstrations of the self-similarity for this case are shown in the figures below. We begin with the shapes of the principal turbulence quantities,  $K$ ,  $S$ ,  $a$ ,  $b$  and density. On the  $y$ -axis, the turbulence quantities are plotted at various times and non-dimensionalized with the maximum values at that time. On the  $x$ -axis, the curve is non-dimensionalized by the width of the mixing layer at that point in time. In Figures 53 through 57, the green line indicates the nominal shape of the variable calculated from the equations on pages 97 and 98, the red, blue and black lines are the shapes at  $t = 0.1, 5.0$  and  $7.0$  s, respectively. Note, for the non-dimensionalization of  $S$ , the mixing width was based on 0.1% and 99.9% of the mass fraction; values of 5% and 95 % were used for the non-dimensionalization of the remaining variables.

As can be seen in the Figures 53 through 57 below, the profiles are approximately correct and the self-similar shape determined by the model is quickly achieved. The best matches are for  $K$ ,  $a$ ,  $S$  and density. The nominal parabolic shape used for  $b$  in this analysis does not work as well; however, there is no physical requirement that  $b$ , or any

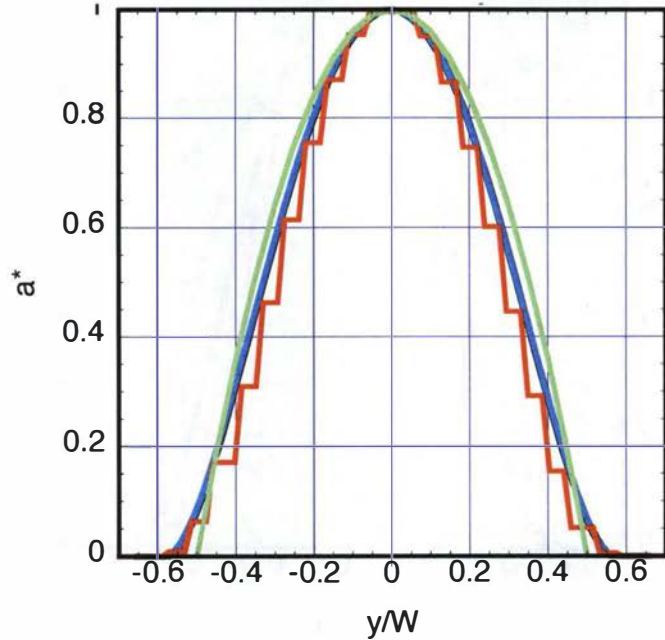
other variable, have a parabolic profile. In this case, it was chosen as a matter of convenience.



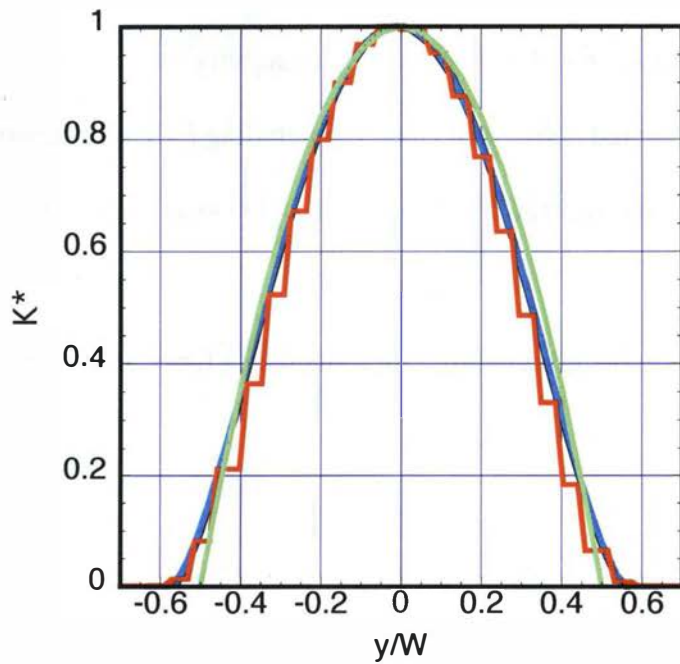
**Figure 53.** Self-similar form for the turbulent length scale,  $S$ . The green line indicates the nominal shape of the variable, the red, blue and black lines are the shapes at  $t = 0.1, 5.0$  and  $7.0$  s, respectively.



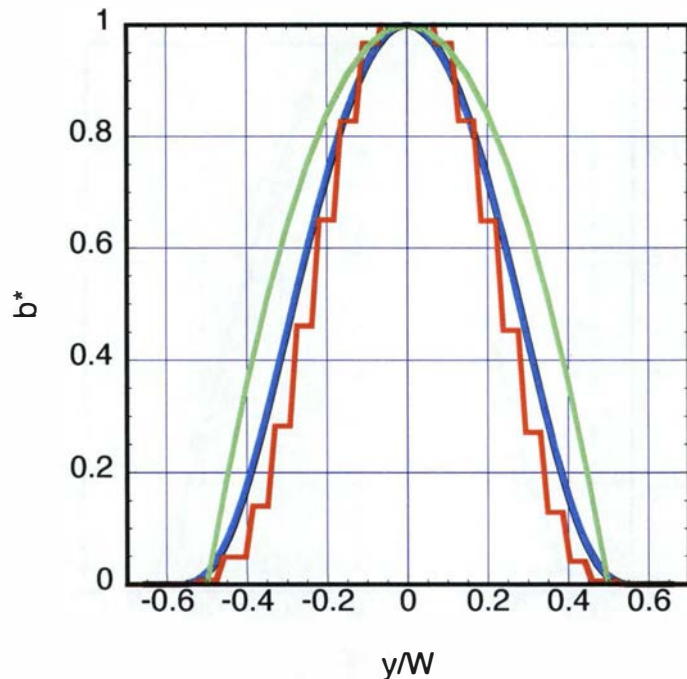
**Figure 54.** Non-dimensional density profile. The green line indicates the nominal shape of the variable, the red, blue and black lines are the shapes at  $t = 0.1, 5.0$  and  $7.0$  s, respectively.



**Figure 55.** Non-dimensional mass flux velocity profiles. The green line indicates the nominal shape of the variable, the red, blue and black lines are the shapes at  $t = 0.1, 5.0$  and  $7.0$  s, respectively.



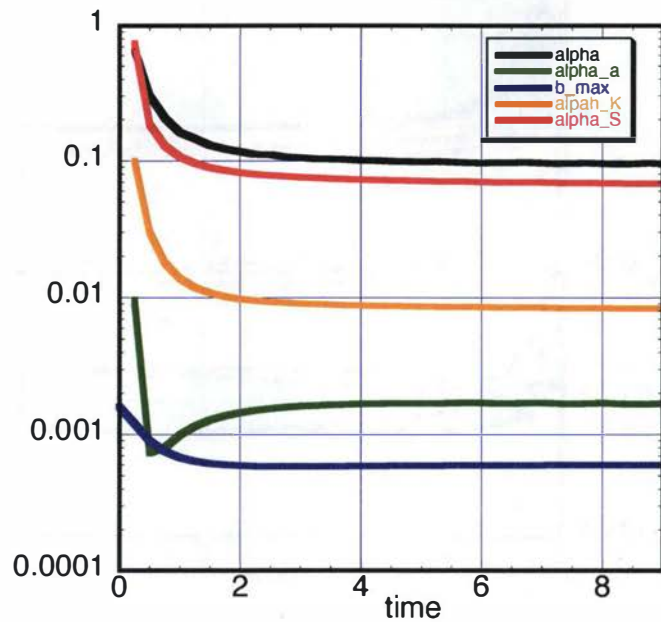
**Figure 56.** Non-dimensional turbulent kinetic energy profiles. The green line indicates the nominal shape of the variable, the red, blue and black lines are the shapes at  $t = 0.1, 5.0$  and  $7.0$  s, respectively.



**Figure 57.** Non-dimensional “b” profiles. The green line indicates the nominal shape of the variable, the red, blue and black lines are the shapes at  $t = 0.1, 5.0$  and  $7.0$  s, respectively.

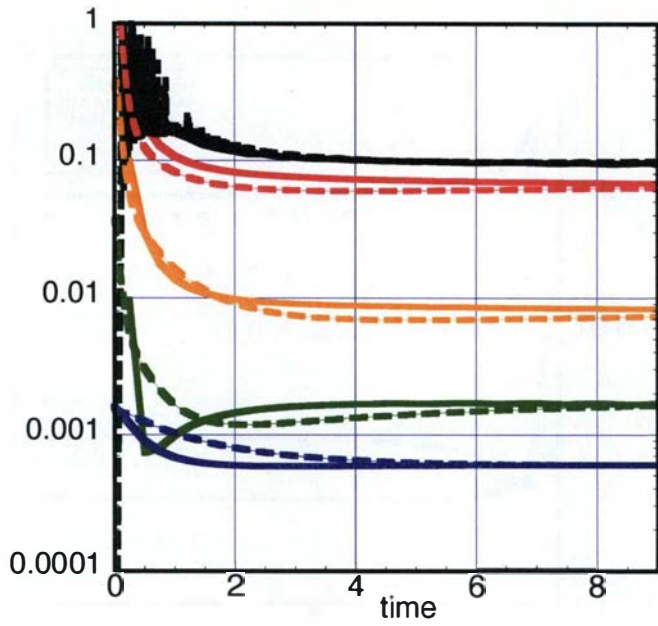
Once self-similar growth is achieved, the magnitudes of the maximum values of the variables presented above will change (excluding  $b$ ) but, in theory, the non-dimensional growth rates ( $\alpha, \alpha_k, \alpha_a, \alpha_s$ ) should not change. This asymptotic behaviour is shown in

Figure 58, where the growth rates are plotted as a function of time.



**Figure 58.** Variation in  $\alpha$ ,  $\alpha_\kappa$ ,  $\alpha_a$  and  $\alpha_s$  as a function of time exhibit self-similar behavior.

In Figure 59, the same plot is shown including the results obtained using the incompressible RTI3D code (dashed). The agreement is good given that the differences in the codes and the growth rates converge at nearly the same self-similar values.



**Figure 59. Alpha versus time for RAGE and RTI3D. Dashed lines are RTI3D simulations; solid lines are from RAGE simulations.**

The self-similar shapes for individual terms for each equation at  $t = 5$  and  $t = 7$  seconds are shown in Figures 60 through 64. These results illustrate that self-similarity is achieved also in term-by-term comparisons; only the dissipation of  $b$  appears to vary slightly. Regarding the profile of the diffusion term in the  $S$  equation, the large value near the edge is due to setting  $\sigma_\epsilon$  to a small value (0.10) to create a flatter profile. If a top hat profile were used, a delta function would be observed at the edges. Overall, the agreement is a remarkable achievement in self-similarity.

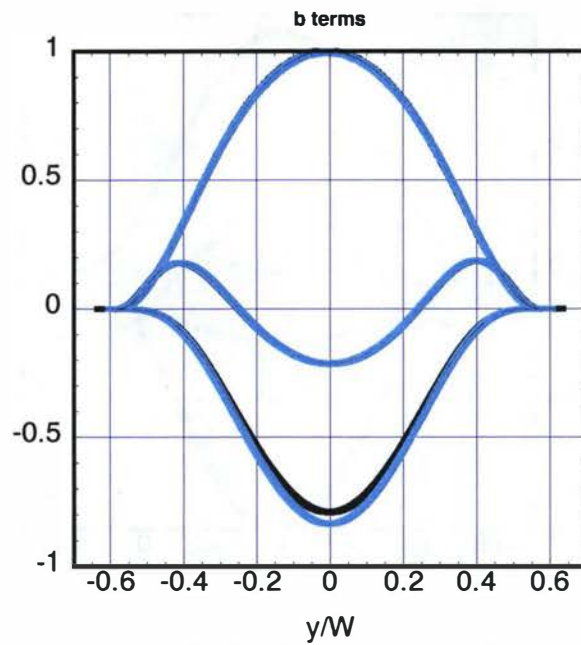


**Figure 60.** Non-dimensionalization of the individual terms in the evolution equation for  $b$ . Black and blue lines indicate  $t = 5$  and  $t = 7$  seconds.

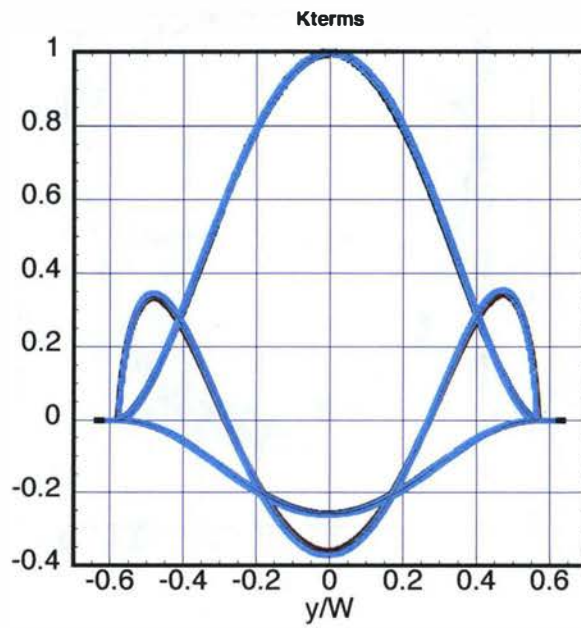


**Figure 61.** Non-dimensionalization of the individual terms in the turbulent kinetic energy,  $K$ . Black and blue lines indicate  $t = 5$  and  $t = 7$  seconds.

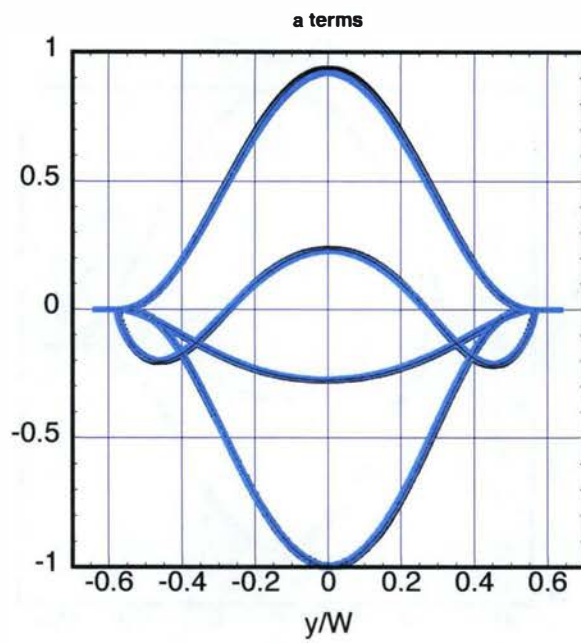


**Figure 62.** Non-dimensionalization of individual terms in evolution equation for mass flux velocity,  $a$ . Black and blue lines indicate  $t = 5$  and  $t = 7$  seconds.

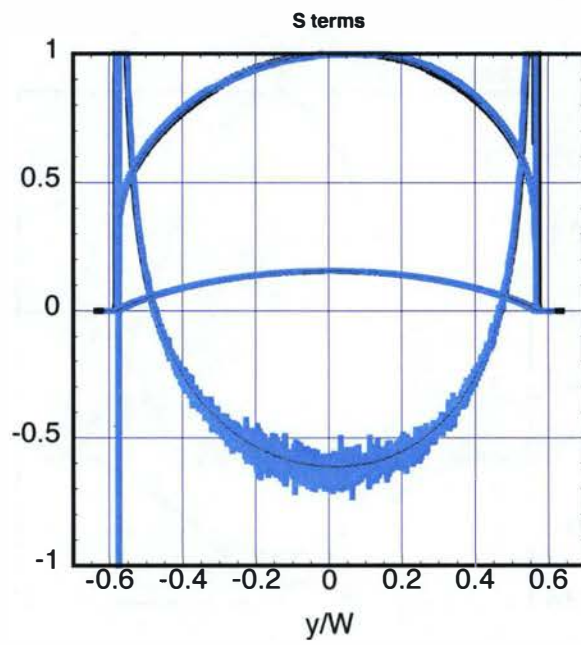


**Figure 63.** Non-dimensionalization of individual terms in evolution equation for turbulent length scale,  $S$ . Plot is scaled such that it does not show full extent of diffusion terms. Black and blue lines indicate  $t = 5$  and  $t = 7$  seconds.

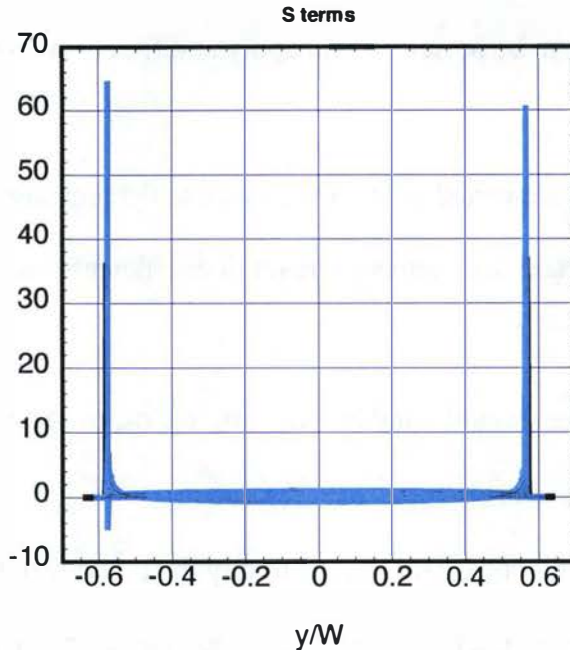


**Figure 64.** Non-dimensionalization of individual terms in evolution equation for turbulent length scale,  $S$ . Plot shows full effect of diffusion. Black and blue lines indicate  $t = 5$  and  $t = 7$  seconds.

On a final note regarding self-similarity, currently, no set of coefficients has been observed to give rise to a non-self-similar state. This is true whether the results match data or if the conditions are considered non-physical, as in the generation of peculiar profiles. It also should be noted the state that is reached is independent of the initial conditions – regardless of the manner in which the model is initialized, it will eventually reach the same self-similar conditions. Those conditions appear to be solely a function of the choice of coefficients.

#### 4.4.7 Effects of varying model coefficients

The motivation for this section is to give the reader a feel for the effects of varying the input coefficients on model outputs. In particular, we are interested in the degree of complexity of the interaction and whether the behaviour is non-linear or non-monotonic. For this analysis, the nominal case is for an Atwood number of 0.20 – a low value, but not too close to zero – and using the base coefficients given in Table 1 above. Though the

results can be useful for model calibration efforts in exploring different data sets, it is uncertain that the trends to be presented will apply at different Atwood numbers and base settings.

The coefficients are varied over a wide range to demonstrate the sensitivity of the overall growth of important parameters. The set of coefficients can be separated into three categories:

1. turbulence Prandtl numbers ( $\sigma_{SIE}$ ,  $\sigma_\varepsilon$ ,  $\sigma_c$ ,  $\sigma_b$ ,  $\sigma_k$ ,  $\sigma_a$ ) that modify the diffusion terms,
2. coefficients ( $C_{al}$ ,  $C_2$ ,  $C_b$ ) that modify the individual dissipation terms and
3. coefficients ( $C_l$ ,  $C_4$ ) in the length scale equation that modify the production terms.

The quantities examined here are primarily the growth rates, or “alphas”, presented in previous sections. These include  $\alpha$ ,  $\alpha_a$ ,  $\alpha_K$ ,  $S/h_{tot}$  or  $\alpha_S/\alpha$  and  $b_{MAX}$ , the last of which is a constant so there is no growth rate associated with it under self-similar conditions.

Additionally, the non-dimensional shapes of some quantities will be presented, e.g.,  $S/S_{max}$  versus  $y/h_{tot}$ .

Before presenting the results, it is useful to comment on some global observations. Typically, the turbulence Prandtl numbers have only a small effect on the non-dimensional growth rates, but they have a more significant effect on the shape of the variable profiles. Conversely, the dissipation coefficients generally don’t result in changes to the shape of the profiles, but changes to these coefficients do affect the alphas. Unlike the Boussinesq model,  $C_\mu$  is not a part of the Reynolds stress model developed by Ristorcelli [46];  $C_\mu$  modifies the turbulent viscosity in only the diffusion of  $K$ ,  $a$ ,  $b$ ,  $S$

and  $c^k$ . Therefore,  $\sigma_a$  and  $\sigma_K$  currently are set to unity in the model and have not been included in this examination. Additionally, the term in the  $S$  equation containing  $C_3$  has not been extensively explored and in this study has been set to zero. Finally, without providing details, we will state that variations in  $C_1$  and  $\sigma_{SIE}$  show very little effect (<1%) on the results.

#### 4.4.7.1        *Effect of varying $\sigma_\epsilon$*

The base value for  $\sigma_\epsilon$  was chosen primarily to match the shape of the length scale data from the two DNS sources [25, 33] presented in Section 4. The change in shape of  $S$  across the mixing layer with variation in  $\sigma_\epsilon$  is shown in Figure 65. As  $\sigma_\epsilon$  is increased, not only does the shape of  $S$  change but, more importantly, the density profile changes as well, as shown in Figure 66. As the shape of the turbulence length scale becomes more parabolic with decreasing  $\sigma_\epsilon$ , the density profile develops an inverted “S” shape, which is not physical. The shape of the length scale reaches self-similarity but we know that it is incorrect.<sup>10</sup> The trends continue in the other direction as  $\sigma_\epsilon$  drops to 0.01, where a more parabolic shape is achieved and a slight “S” shape develops in the density profile. The variation of alphas with  $\sigma_\epsilon$  is shown in Figure 67. As stated previously, the effect on the alphas is relatively small, in this case  $\pm 40\%$  variation in alphas for a  $\pm 10x$  change in  $\sigma_\epsilon$ . Additionally, the effect is not linear or even monotonic for all the variables.

---

<sup>10</sup> This is an issue with the original implementation of the model, which created a density “cleave”, as seen in Steinkamp, 1999 [59].

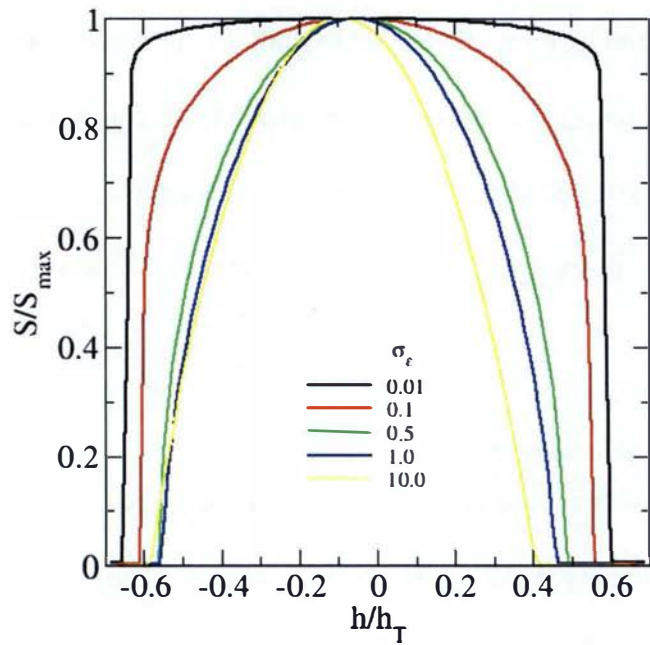


**Figure 65.** Profile of non-dimensionalized turbulent length scale,  $S/S_{max}$ , as a function of  $\sigma_\epsilon$  across the mixing layer.

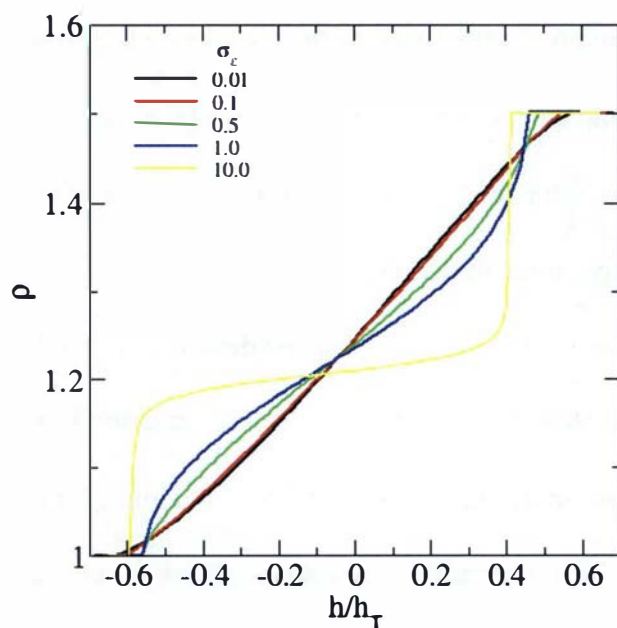


**Figure 66.** Density profile,  $\rho$ , as a function of  $\sigma_\epsilon$  across the mixing layer.

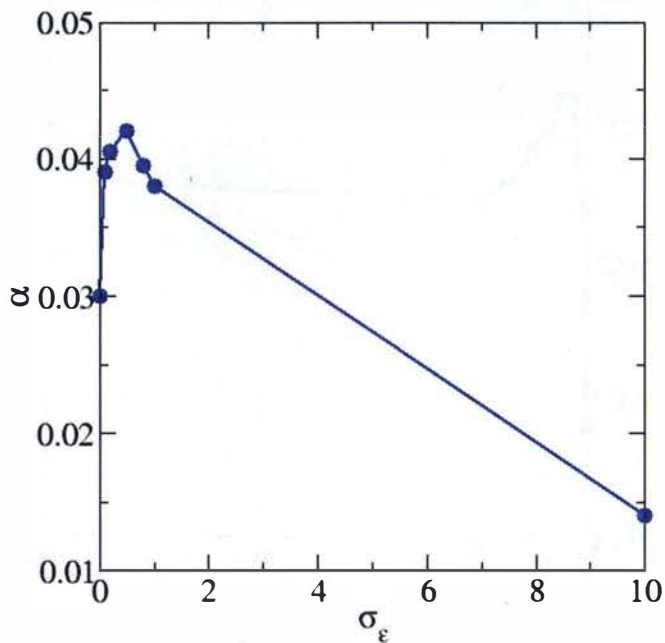


**Figure 67.** Growth rate of mixing layer,  $\alpha$ , as a function of  $\sigma_\epsilon$ .

#### 4.4.7.2      *Effect of varying $\sigma_c$*

In Figure 68, varying the value of  $\sigma_c$  results in only small changes to the late-time self-similar growth, except when the value is small ( $< 0.1$ ). The variation is non-linear and non-monotonic.

The behaviour of density with changes to  $\sigma_c$  is shown in Figure 69. The same type of “S” and inverted “S” shapes appear that were observed above in Figure 66, but to a lesser extent. As mentioned previously,  $\sigma_c$  was set using the shape of the density profile for *low* Atwood number Rayleigh-Taylor turbulence. The value of  $\sigma_c = 0.6$  was chosen for a density profile that was linear through the mixing layer with a smooth transition at the edges.

The non-dimensional shapes of the turbulence quantities are not shown here, but change only modestly through this set of variations. The turbulence variable that is most sensitive to variations in  $\sigma_c$  is  $b_{MAX}$ , shown in Figure 70.

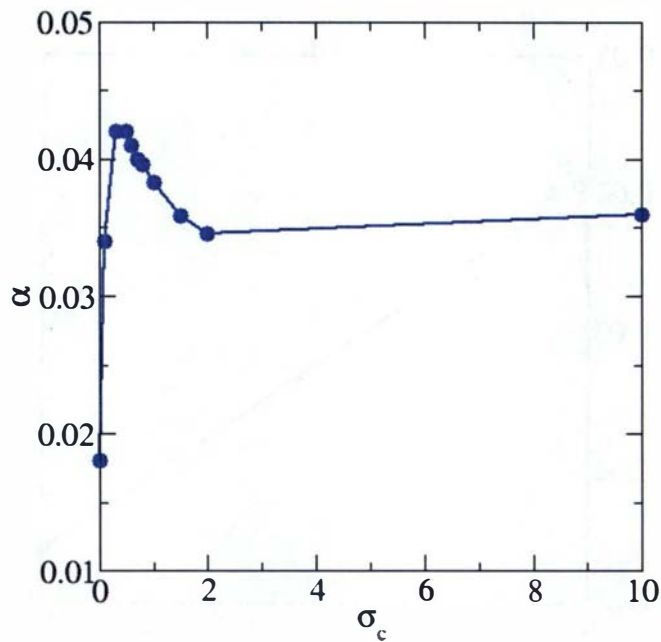


Figure 68. Growth rate of mixing layer,  $\alpha$ , as a function of  $\sigma_c$ .

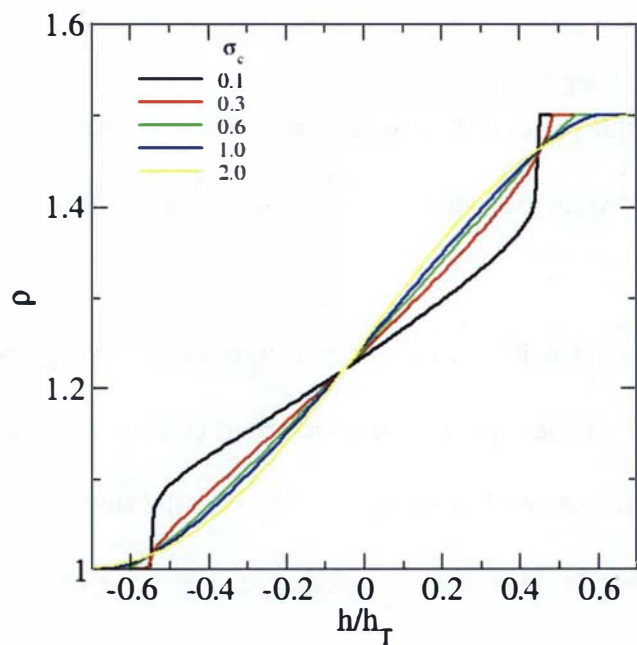
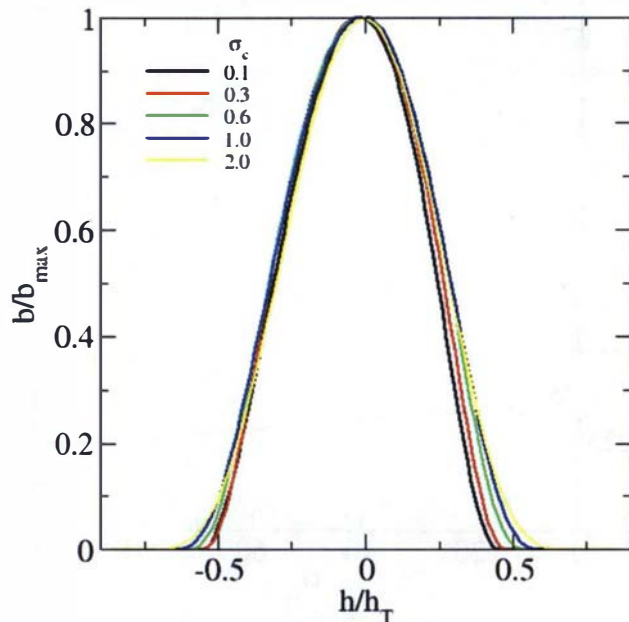


Figure 69. Density profile,  $\rho$ , as a function of  $\sigma_c$  across the mixing layer.



**Figure 70. Profile of non-dimensionalized density-specific volume correlation,  $b/b_{max}$ , as a function of  $\sigma_c$  across the mixing layer.**

#### 4.4.7.3        *Effect of varying $\sigma_b$*

The effect of the variation of  $\sigma_b$  on the alphas is shown in Figure 71. Varying  $\sigma_b$  resulted in very small changes to the model variables, particularly for  $1.0 \leq \sigma_b \geq 6.0$  ( $0.046 > \alpha > 0.036$ ), and therefore those results are not included here. The default model value for  $\sigma_b$  is 2.5, based on the calculations discussed in Section 4.4.2.

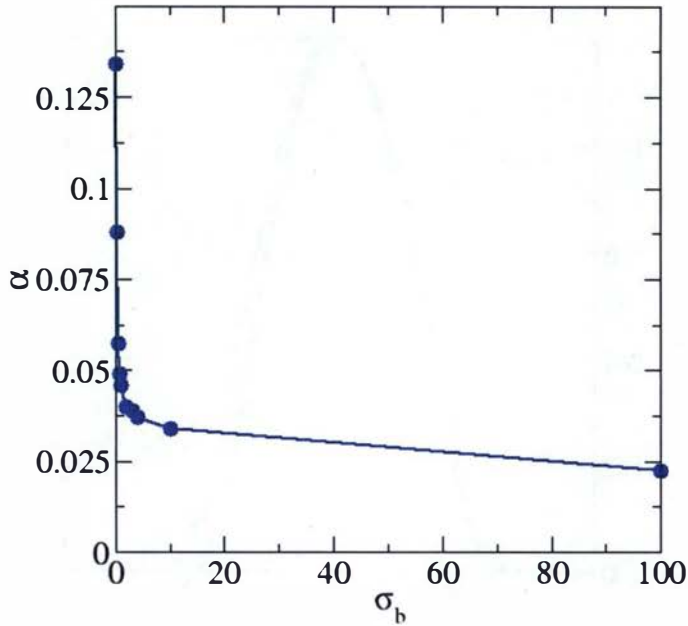


**Figure 71.** Growth rate of mixing layer,  $\alpha$ , as a function of  $\sigma_b$ .

#### 4.4.7.4 Effects of varying $C_4$ , $C_{al}$ , $C_2$ and $C_b$

The dissipation coefficients  $C_{al}$ ,  $C_2$  and  $C_b$  play a reduced yet important role when compared to  $C_4$ , the turbulent length scale production coefficient in  $S$ . This is shown in Figures 73 through 76. The coefficients, in order of most sensitive to least sensitive to variations, are  $C_4$ ,  $C_{al}$ ,  $C_2$  and  $C_b$ . The coefficient  $C_2$  is the only coefficient that was set using a completely different flow, i.e., homogeneous isotropic decay. The sensitivity of the flow to the  $C_4$  coefficient (note the variation amongst the different numerical values for the axes), along with the relative tie between  $\alpha$ ,  $\alpha_a$ , and  $\alpha_K$ , was the principal reason for trying to maintain only one coefficient change when modelling experiments with different self-similar growth rates.

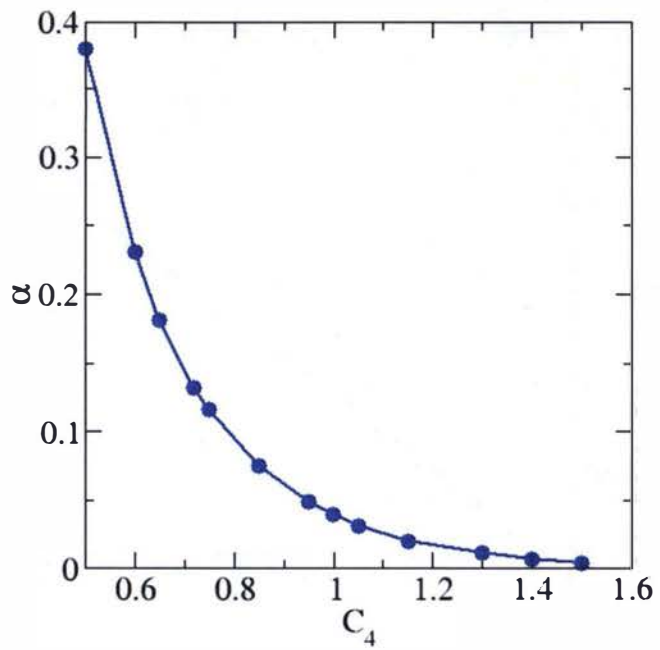


Figure 72. Growth rate of mixing layer,  $\alpha$ , as a function of  $C_4$ .

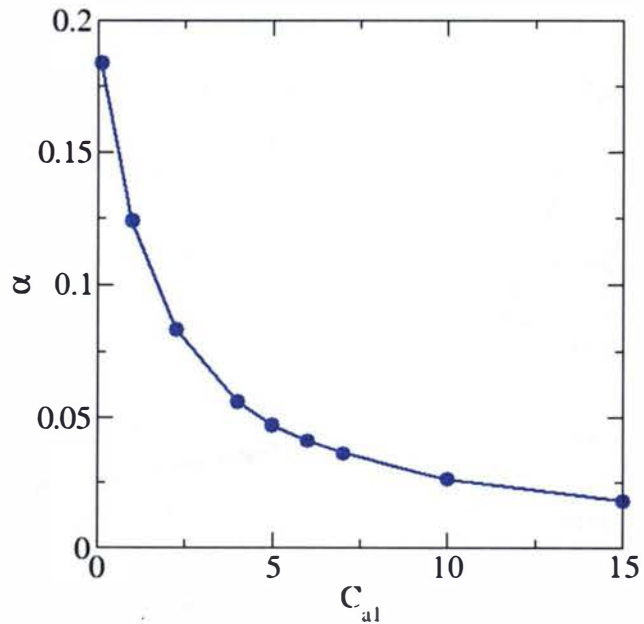


Figure 73. Growth rate of mixing layer,  $\alpha$ , as a function of  $C_{al}$ .

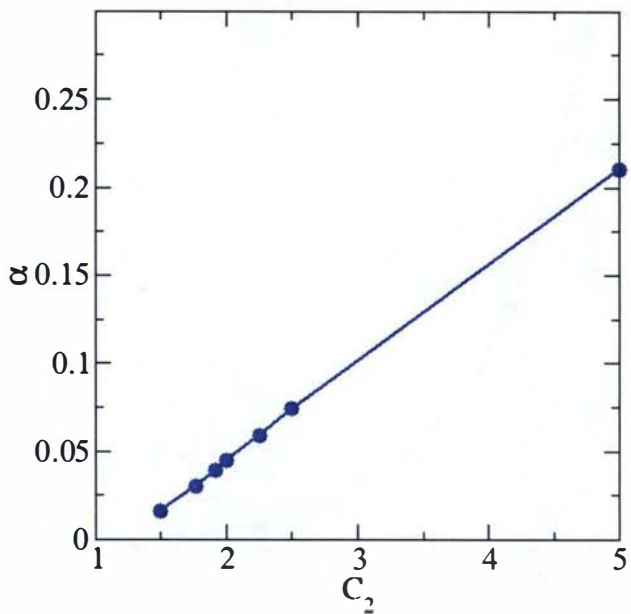


Figure 74. Growth rate of mixing layer,  $\alpha$ , as a function of  $C_2$ .

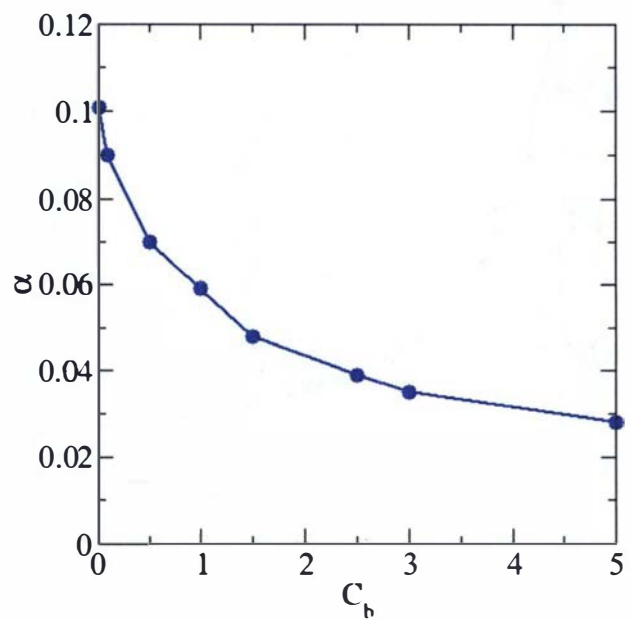


Figure 75. Growth rate of mixing layer,  $\alpha$ , as a function of  $C_{b2}$ .

#### **4.5 Homogeneous variable-density turbulence**

Livescu and Ristorcelli [33] examined buoyancy-driven homogeneous variable-density turbulence (HVDT) in an unstably stratified medium composed of two compressible, miscible fluids with different densities using DNS. It was treated as a unit problem for variable density turbulence to study: “(i) the nature of variable density turbulence, (ii) the transition to turbulence and the generation of turbulence by the conversion of potential to kinetic energy, (iii) the role of non-Boussinesq effects, and (iv) a parameterization of the initial conditions by a static Reynolds number.” In this investigation, the HVDT results are used as a “proof of concept” tool for validating BHR2.

##### *4.5.1 Method and simulation details*

For the DNS, the governing equations are solved in a domain that is periodic in all three directions using a pseudo-spectral method. Further details can be found in [33]. Initially, the density field is composed of random blobs of pure fluids shown in red and purple in Figure 76. Gravity is “turned on” and the fluids begin to mix. As mass flux is created by the pressure gradient-density gradient mismatch, potential energy is converted to kinetic energy. The turbulent kinetic energy increases and peaks at a point where the fluids are atomically mixed enough that production due to buoyancy forces decreases and is overtaken by viscous dissipation (cf. Figure 76 (b)). In late time, the fluids are well mixed, as indicated by the green and blue in (c). The density gradient goes to zero and viscous dissipation dominates.



**Figure 76. HVDT density plot: (a) Initial time, (b) peak turbulent kinetic energy and (c) late time.**  
Reproduced from [33].

Due to the homogeneity of the flow and incompressibility of the fluids, the  $K$ ,  $S$  and  $\alpha$  equations in BHR and BHR2 can be reduced to a set of first order ordinary differential equations and arranged as follows,

$$\frac{dK}{dt} = \left( \frac{1}{\bar{\rho}} \frac{d\bar{p}}{dx} \right) a_x - \frac{K^{3/2}}{S}, \quad (1.128)$$

$$\frac{dS}{dt} = \frac{S}{K} \left( \frac{3}{2} - C_4 \right) \left( \frac{1}{\bar{\rho}} \frac{d\bar{p}}{dx} \right) a_x - \left( \frac{3}{2} - C_2 \right) \sqrt{K} \quad (1.129)$$

and

$$\frac{da_x}{dt} = \left( \frac{1}{\bar{\rho}} \frac{d\bar{p}}{dx} \right) b - C_{al} a_x \frac{\sqrt{K}}{S}. \quad (1.130)$$

Additionally, for BHR2, we have a reduced equation for  $b$ ,

$$\frac{db}{dt} = -C_b b \frac{\sqrt{K}}{S}. \quad (1.131)$$

This simplified system of equations was solved using Mathematica. These results are compared with the DNS results next.

#### 4.5.2 Results comparing BHR and BHR-2

Results for the turbulent kinetic energy,  $K$ , mass flux velocity,  $a_y$ , and density-specific volume correlation,  $b$ , from the HVDT DNS are shown in Figure 77 for an Atwood number of 0.25. A more detailed description of the evolution of the flow can be found in Livescu and Ristorcelli [33], but an overview is given here. At initial time,  $K$  and  $a_y$  are small values close to zero and  $b$  is at the maximum value, i.e., the density fluctuations are largest before the two fluids have begun to mix. Gravity is turned on and the body force results in the two fluids moving in opposite directions relative to each other. The mass flux increases, consequently, driving the increase in the turbulent kinetic energy. Large and small-scale fluctuations in the density and velocity fields cause the fluids to mix, and molecular mixing occurs where the two fluids come into contact with each other. The molecular mixing results in a decrease in the density fluctuations and, thus, a decrease in  $b$ . As the fluids become molecularly mixed,  $b$  goes to zero and the mass flux decreases. Buoyancy forces are overtaken by viscous forces and the turbulence begins to decay. At late time, the fluids are nearly completely molecularly mixed. The larger scale motions still being fed by buoyancy forces slowly decay as viscous forces dominate and, consequently, we see  $K$  gradually decrease and flatten.

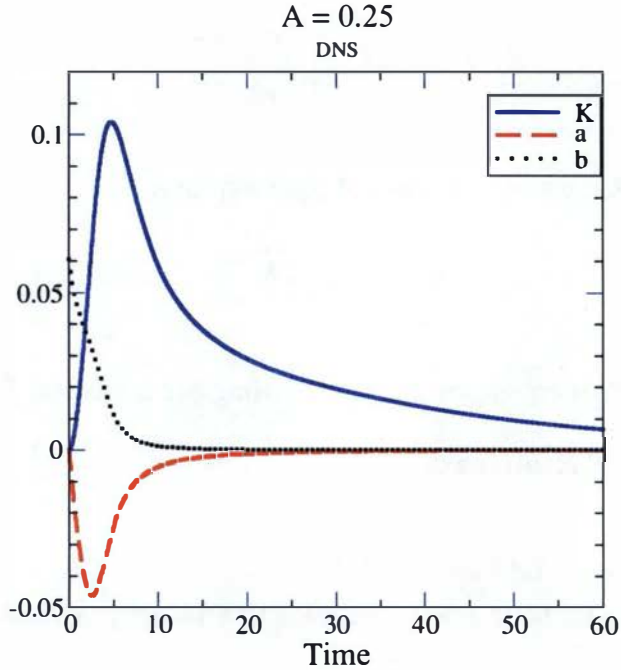


**Figure 77. Turbulent kinetic energy,  $K$ , mass flux velocity,  $a_y$ , and density-specific volume correlation,  $b$ , results for DNS of homogeneous variable-density turbulence.**

BHR and BHR2 results have been compared with the DNS data for low to mid-range Atwood numbers of 0.05, 0.25 and 0.5. These are “proof of concept” cases to demonstrate the ability of the new model to better capture the physics of the flow. First, BHR results are compared to the DNS for an Atwood number of 0.25 in Figure 78. The dashed and solid lines represent the DNS and BHR results, respectively. It is clear that the model cannot capture the correct turbulence physics, particularly the effects of molecular mixing, for this configuration. Using the original BHR model implementation,  $b$  is solved using the simple analytic formula and, therefore, remains constant. The constant  $b$  continues to drive the  $bdp/dx$  production term in the mass flux velocity and, consequently,  $a$  continuously drives the  $adp/dx$  production of the turbulent kinetic energy. BHR fails for this case because the density fluctuations should decrease as the fluids molecularly mix, but this is not allowed to happen. Another way to understand the

problem is to note that, physically, fluids may break down but they never mix so there are always density fluctuations driving  $a$  and  $K$ , never allowing the turbulence to decay.

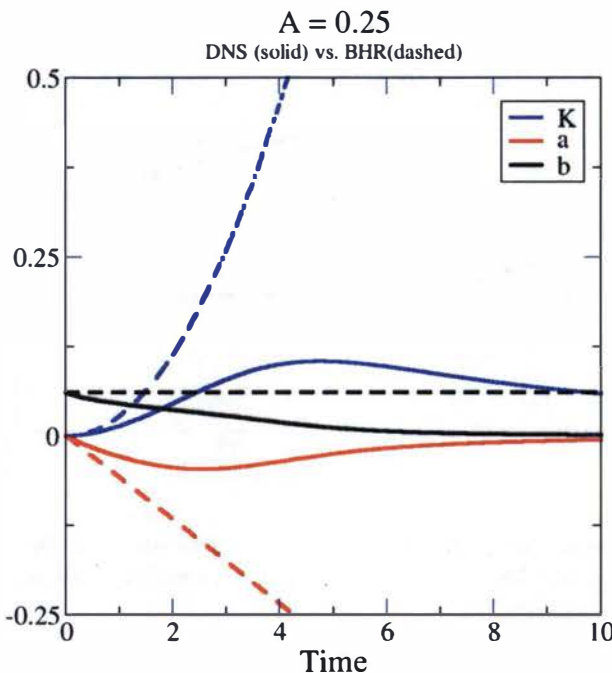


**Figure 78.** Turbulent kinetic energy, mass flux velocity and density-specific volume correlation results for DNS of homogeneous variable-density turbulence for an Atwood number of 0.25 compared with results using the first generation BHR model.

Next, the results using BHR2, with the capability of evolving  $b$ , are presented in Figures 80 through 82. One can see that the match between the model and the DNS is improved significantly. The value of  $b$  decreases as the fluids molecularly mix. When the fluids are mixed enough such that viscous dissipation begins to overtake the turbulent production, the mass flux and, consequently, the turbulent kinetic energy subsequently decrease. Good matches were obtained across the full range of Atwood numbers with the same set of model coefficients.

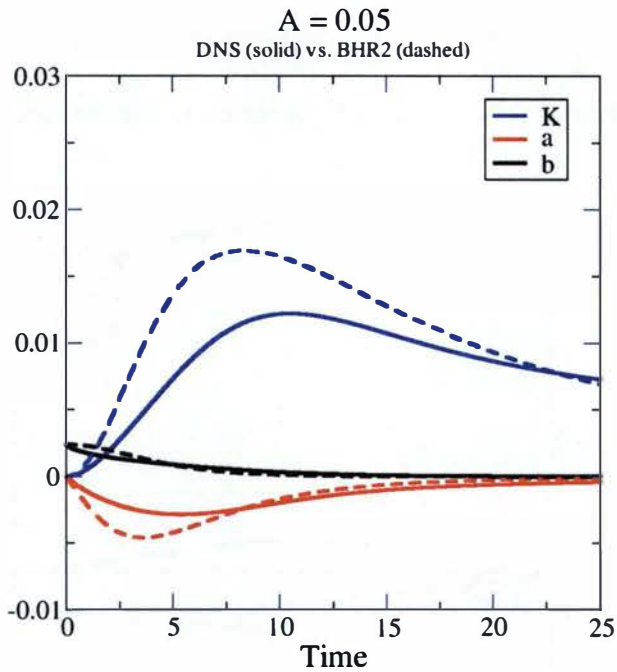


**Figure 79.** Turbulent kinetic energy, mass flux velocity and density-specific volume correlation results for DNS of homogeneous variable-density turbulence with an Atwood number of 0.05 compared with results using BHR2.

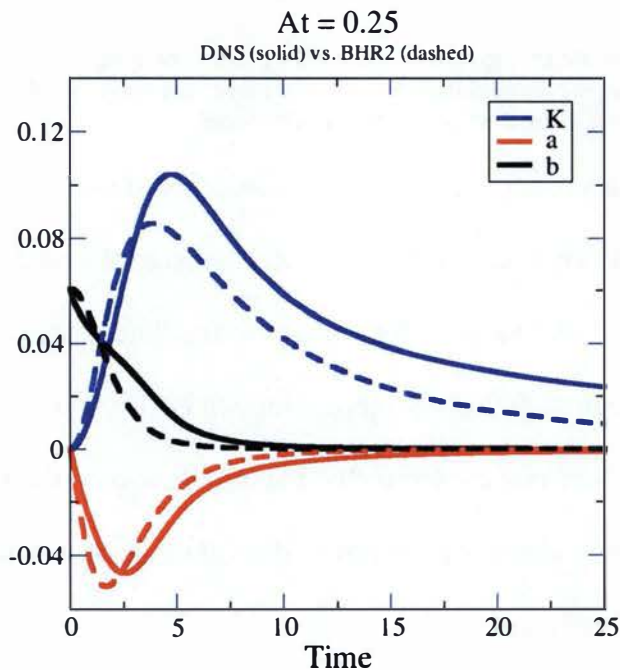


**Figure 80.** Turbulent kinetic energy, mass flux velocity and density-specific volume correlation results for DNS of homogeneous variable-density turbulence with an Atwood number of 0.25 compared with results using BHR2.

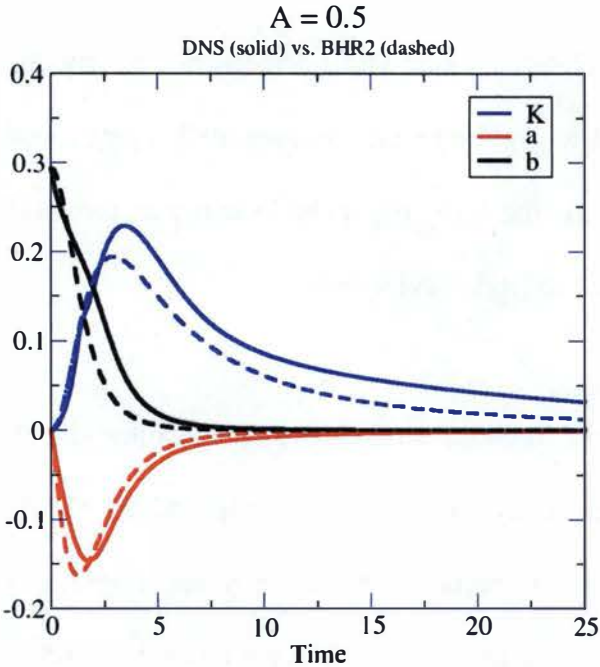


**Figure 81.** Turbulent kinetic energy, mass flux velocity and density-specific volume correlation results for DNS of homogeneous variable-density turbulence with an Atwood number of 0.5 compared with results using BHR2.

## 5. Summary and conclusions

In summary, an evolution equation for the density-specific volume correlation,  $b$ , was implemented in RAGE as part of the second generation BHR2 turbulence model. Other changes to the original implementation of the BHR model included a new model for the Reynolds stress tensor [43] and the inclusion of more of the derived terms from the exact equation for the mass flux velocity.

As part of the validation process, this model was tested and analysed using a suite of small-scale Rayleigh-Taylor experiments, including direct numerical simulations. These included the DNS of Cabot et al. [25] for a simple RT mixing layer, the RT gas channel experiments of Banerjee et al. [42], the homogeneous variable-density turbulence DNS of Livescu et al. [33] and the rocket rig experiments of Read [15], Smeeton et al. [16] and Youngs [17]. The first two cases were used refine the values of

coefficients in the model equations, as well as for validation. The latter cases were utilized as additional validation cases which demonstrate clearly the ability of the evolution equation of  $b$  to capture previously unmodelled physics important to variable-density flows, particularly the decay of  $b$  in molecularly mixed fluids and in the transition from unstable to stable Rayleigh-Taylor flows.

## 6. Future directions

The manner in which the Reynolds stress is evaluated varies widely in the literature. Unfortunately, in the currently used Reynolds stress model for BHR2, the numerical implementation leads to instabilities in the results of some flows at very late times. Two of the key constraints on our modelling efforts are robustness and stability. It is hoped that future research will lessen or eliminate this problem. One approach is to go to a new model, more specifically, modelling the full evolution of the Reynolds stress. This effort currently is being pursued by Schwartzkopf et al. [43].

Future work is planned to explore the differences between the use of a gradient diffusion approximation for the energy and concentration equations versus full evolution equations. No known references are available that model the full equations.

Richtmyer-Meshkov turbulence, also important to the flow problems of interest, has been explored in the past, though not extensively validated. This will be the focus of future efforts towards verification and validation of future BHR models.

## Nomenclature

$\mathbf{a}$	acceleration vector
$a_i$	turbulent mass flux velocity (“drift velocity”)
$A$	$= (\rho_1 - \rho_2) / (\rho_1 + \rho_2)$ , Atwood number
$b$	density-specific volume correlation, turbulence parameter
$b_{ij}$	Reynolds stress anisotropy tensor
$c$	speed of sound

$c^k$	species concentration
$C_i$	$i = 1, 2, 3$ and $4$ , BHR2 model coefficient in turbulent length scale equation
$C_{al}$	BHR2 model coefficient in mass flux velocity equation
$C_A$	Reynolds stress model coefficient
$C_b$	BHR2 model coefficient in density-specific volume correlation equation
$C_p$	specific heat, constant pressure
$C_v$	specific heat, constant volume
$C_S$	Reynolds stress model coefficient
$C_\mu$	model coefficient for turbulent viscosity
$D$	coefficient of diffusivity
$E$	kinetic energy
$\mathbf{F}$	force vector
$g$	acceleration due to gravity
$h$	specific enthalpy; width of mixing layer
$\dot{h}$	rate of change of mix width
$I$	internal energy
$k$	$\equiv 2\pi / \lambda$ , wave number; species index
$K$	turbulence kinetic energy
$l_t$	turbulence length scale
$L$	characteristic length
$m$	mass
$M$	molecular weight
$M$	$= U / c$ , Mach number
$M_t$	$M_t = \sqrt{2K} / \bar{c}$ , turbulence Mach number
$p$	pressure
$Pr_t$	turbulence Prandtl number
$R$	$\equiv UL / \nu$ , bulk Reynolds number
$R_t$	$= \frac{u_t l_t}{\nu} = \frac{l_t^2 / \nu}{l_t / u_t}$ , turbulence Reynolds number
$R_{ij}$	Reynolds stress tensor
$s$	wave propagation speed
$S$	$\equiv K^{3/2} / \varepsilon$ , turbulence length scale in BHR2 model
$S^*$	$S/S_{centerline}$
$S_n$	turbulent “heat flux”
$t$	time
$t_t$	turbulence time scale
$\mathbf{u}$	velocity vector
$u''$	mass-weighted velocity fluctuation
$u_t$	turbulence velocity scale
$U$	characteristic velocity
$V$	volume
$\mathbf{x}$	position vector

### Greek Symbols

$\alpha$	growth constant or rate of turbulent mixing layer
$\delta_{ij}$	Kronecker delta
$\varepsilon$	$= u_t^3 / l_t, = K^{3/2} / S, = -dK / dt$ , dissipation of turbulence kinetic energy
$\gamma$	polytropic index
$\kappa$	coefficient of thermal conductivity
$\kappa_t$	coefficient of thermal conductivity for turbulent material
$\eta$	$\equiv (v^3 / \varepsilon)^{1/4}$ , Kolmogorov length scale
$\mu$	dynamic viscosity
$\nu$	kinematic viscosity
$\nu_t$	turbulent viscosity
$\rho$	density
$\sigma_a$	BHR2 model coefficient in mass flux velocity equation
$\sigma_b$	BHR2 model coefficient in density-specific volume correlation equation
$\sigma_c$	BHR2 model coefficient in species concentration equation
$\sigma_k$	BHR2 model coefficient in turbulent kinetic energy equation
$\sigma_{SIE}$	BHR2 model coefficient in energy equation
$\sigma_\varepsilon$	BHR2 model coefficient in turbulent length scale equation
$\tau$	$\equiv (v / \varepsilon)^{1/2}$ , Kolmogorov time scale
$\theta$	$\sim 1 - (b / b_{\max})$ , molecular mix variable
$v$	$\equiv (v\varepsilon)^{1/4}$ , Kolmogorov velocity scale

#### Other

$\bar{x}$	uniformly weighted ensemble-averaged variable
$\tilde{x}$	mass weighted ensemble-averaged variable
$x'$	fluctuation about uniformly weighted ensemble-averaged variable
$x''$	fluctuation about mass weighted ensemble-averaged variable
$x_0$	initial value
$x^*$	non-dimensionalized

#### References

1. B. R. Stull, *An Introduction to Boundary Layer Meteorology*, Kluwer Academic Publishers, 1998.
2. *Rough around the edges*, NASA/JPL/Space Science Institute (2004), Available at <http://photojournal.jpl.nasa.gov/catalog/PIA06502>.
3. G. L. Mellor and P. A. Durbin, *The structure and dynamics of the ocean surface mixed layer*, J. Phys. Oceanogr. 5 (1975), pp. 718-728.
4. E. B. Kraus and J. A. Businger, *Atmosphere–Ocean Interaction*. Oxford University Press, p. 362, 1994.
5. J. J. Hester, *The Crab Nebula: an astrophysical chimera*, Annual Review of Annu. Rev. Astron. Astrophys., 46 (2008), pp. 127–155.
6. R. Nemiroff and J. Bonnell, *The Crab Nebula from VLT*, FORS Team (1999), Available at <http://apod.nasa.gov/apod/ap991122.html>.

7. J. Franco and A. Carraminana, *Interstellar Turbulence*. Cambridge University Press, p. xi, 1999.
8. J. O. Hinze, *Turbulence: An Introduction to Its Mechanism and Theory*, McGraw-Hill, Inc., New York, 1959.
9. H. Tennekes and J. L. Lumley, *A First Course in Turbulence*, The MIT Press, Cambridge, 1972.
10. P. K. Kundu and I. M. Cohen. *Fluid Mechanics*, 3<sup>rd</sup> ed., Elsevier Academic Press, San Diego, 2004.
11. S. B. Pope, *Turbulent Flows*, Cambridge University Press, New York, 2000.
12. D. C. Wilcox, *Turbulence Modeling for CFD*, 3<sup>rd</sup> ed., DCW Industries, Inc., San Diego, CA, 2006.
13. A. N. Kolmogorov, *The local structure of turbulence in incompressible viscous fluid for very large Reynolds numbers*, Proc. R. Soc. London Ser. A 434 (1991), pp. 9-13.
14. P. Chaissang, R. A. Antonia, F. Anselmet, L. Joly and S. Sarkar, *Variable Density Fluid Turbulence*, Kluwer Academic Publishers, Dordrecht, Netherlands, 2002.
15. K. I. Read, *Experimental investigation of turbulent mixing by Rayleigh-Taylor instability*, Physica 12D (1984), pp. 45-58.
16. V. S. Smeeton and D. L. Youngs. *Experimental investigation of turbulent mixing by Rayleigh-Taylor instability: Part 3*, Tech. Rep. 035/87, AWRE, Aldermaston, UK, 1987.
17. D. L. Youngs, *Modelling turbulent mixing by Rayleigh-Taylor instability*, Physica D 37 (1989), pp. 270-287.
18. J. R. Ristorcelli and T. T. Clark, *Rayleigh-Taylor turbulence: self-similar analysis and direct numerical simulations*, J. Fluid Mech. 507 (2004), pp. 213-253.
19. S. Terrade, *Overview of Hydrodynamic Instabilities*, ENSEEIHT (2001), Available at  
[http://hmf.enseeiht.fr/travaux/CD0001/travaux/optmfn/hi/01pa/hyb72/kh/kh\\_theo.htm](http://hmf.enseeiht.fr/travaux/CD0001/travaux/optmfn/hi/01pa/hyb72/kh/kh_theo.htm).
20. P. G. Drazin and W. H. Reid, *Hydrodynamic Stability*, 2<sup>nd</sup> ed., Cambridge University Press, New York, 2004.
21. J. Mathieu and J. Scott, *An Introduction to Turbulent Flow*, 1<sup>st</sup> ed., Cambridge University Press, New York, 2000.
22. Lord Rayleigh, *Investigation of the character of the equilibrium of an incompressible heavy fluid of variable density*, Scientific Papers, Cambridge University Press, Cambridge 2 (1900), pp. 200-207.
23. G. I. Taylor, *The instability of liquid surfaces when accelerated in a direction perpendicular to their planes*, Proc. R. Soc. London Ser. A 201 (1950), pp. 192-196.
24. M. J. Andrews, *Turbulent mixing by Rayleigh-Taylor instability*, Ph.D. diss., Imperial College of Science and Technology, London, 1986.
25. W. H. Cabot and A. W. Cook, *Reynolds number effects on Rayleigh-Taylor instability with the possible implications for type-Ia supernovae*, Nature Physics 2 (2006), pp. 562-568.
26. S. Chandrasekhar, *Hydrodynamic and Hydromagnetic Stability*, Oxford University Press, Oxford, England, 1961.

27. R. LeLevier, G. Lasher and F. Bjorkland, *Effect of a density gradient on Rayleigh-Taylor instability*, Tech. Rep. UCRL-4459, Lawrence Livermore Laboratory, Livermore, CA, p. 4459, 1955.
28. D. Livescu, *Compressibility effects on the Rayleigh-Taylor instability growth between immiscible fluids*, Phys. Fluids 16 (2004), pp. 118-127.
29. K. Prestridge, Pictures from shocked and reshocked gas curtain experiment, P-23 Extreme Fluids Team, Los Alamos National Laboratory, Los Alamos, NM, 2008.
30. D. Israel, Picture from LES simulation of Rayleigh-Taylor layer, Los Alamos National Laboratory, Los Alamos, NM, 2008.
31. K. Stalsberg-Zarling. Picture from RANS simulation of Rayleigh-Taylor layer, Los Alamos National Laboratory, Los Alamos, NM, 2008.
32. S. A. Orszag, *Analytical theories of turbulence*, J. Fluid Mech. 41 (1970), pp. 363-386.
33. D. L. Livescu and J. R. Ristorcelli, *Buoyancy-driven variable-density turbulence*, J. Fluid Mech. 591 (2007), pp. 43-71.
34. D. J. Hill, C. Pantano and D. I. Pullen, *Large-eddy simulation and multiscale modeling of a Richtmyer-Meshkov instability with reshock*, J. Fluid Mech 557 (2006), pp. 29-61.
35. J. C. Tannehill, D. A. Anderson and R. H. Pletcher, *Computational Fluid Mechanics and Heat Transfer*, 2<sup>nd</sup> ed., Taylor & Francis, Washington, D. C., 1997.
36. K. K. Kuo, *Principles of Combustion*, 2<sup>nd</sup> ed., John Wiley & Sons, Inc., Hoboken, NJ, 2005.
37. M. Ishii, *Thermo-fluid Dynamic Theory of Two-Phase Flow*, Eyrolles, Paris, France, 1975.
38. D. C. Besnard, F. H. Harlow, R. M. Rauenzahn and C. Zemach, *Turbulence transport equations for variable-density turbulence and their relationship to two-field models*, Tech. Rep. LA-12303, Los Alamos National Laboratory, Los Alamos, NM, 1992.
39. F. H. Harlowe and A. Amsden, *Fluid dynamics*, Tech. Rep. LA-4700, Los Alamos National Laboratory, Los Alamos, NM, 1971.
40. B. E. Launder, G. J. Reece and W. Rodi, *Progress in the development of a Reynolds-stress turbulence closure*, J. Fluid Mech. 68 (1975), pp. 537-566.
41. J. S. Bendat and A. G. Piersol, *Random Data: Analysis and Measurement Procedures*, Wiley-Interscience, New York, 1971.
- BHR or BHR1** 42. A. Banerjee, R. A. Gore and M. J. Andrews, *Development and validation of a turbulent-mix model for variable-density and compressible flows*, Phys. Rev. E 82, 046309 (2010).
43. J. Schwartzkopf, D. Livescu, R. A. Gore, R. M. Rauenzahn and J. R. Ristorcelli, *Application of a second-moment closure model to mixing processes involving multi-component miscible fluids*, Tech. Rep. LA-UR-11-02406, Los Alamos National Laboratory, Los Alamos, NM, 2011.
44. G. Dimonte and R. Tipton, *K-L turbulence model for self-similar growth of the Rayleigh-Taylor and Richtmyer- Meshkov instabilities*, Phys. Fluids 18, 085101 (2006).

45. O. Gregoire, D. Souffland and S. Gauthier, *A second-order turbulence model for gaseous mixtures induced by Richtmyer-Meshkov instability*, J. Turbul. 6 (2005).
46. R. J. Ristorcelli, D. Livescu and N. Hjelm, *An eddy viscosity expression for Favre averaged Reynolds stresses in variable density turbulence*, Tech. Rep. LA-UR-05-5837, Los Alamos National Laboratory, Los Alamos, NM, 2005.
47. T. Clark, *A multispecies generalization of the BHR turbulent mix model*, Tech. Rep. undocumented, Los Alamos National Laboratory, Los Alamos, NM, 2002.
48. D. Livescu, J. R. Ristorcelli, R. A. Gore, S. H. Dean, W. H. Cabot and A. W. Cook, *High Reynolds number Rayleigh-Taylor turbulence*, J. Turbul. (submitted 2008).
49. G. Dimonte, *Spanwise homogeneous buoyancy-drag model for Rayleigh-Taylor mixing and experimental evaluation*, Phys. Plasmas 7 (2000), pp. 2255-2269.
50. R. Schiestel, *Modeling and Simulation of Turbulent Flows*, John Wiley & Sons, Inc., Hoboken, NJ, 2008.
51. J. H. Kent and R. W. Bilger, *The prediction of turbulent diffusion flame fields and nitric oxide formation*, Proceedings 16<sup>th</sup> Symp. Combustion, The Combustion Institute, 1977.
52. S. Sarkar and B. Lakshmanan, *Application of a Reynolds-stress turbulence model to the compressible shear layer*, AIAA J. 29 (1991), pp. 743-749.
53. W. P. Jones, *Models for turbulent flows with variable density and combustion*, Prediction Methods for Turbulent Flows, Lect. Ser. 1979-2, Edited by W. Kollman, Von Karman Institute, 1979.
54. C. Chen and S. Law, *Fundamentals of Turbulent Flow*, Taylor and Francis, 1998.
55. Ristorcelli, J. R. Personal communication, 2008
56. D. B. Spalding, *Concentration fluctuations in a round turbulent free jet*, J. Chem. Eng. Sci. 26 (1971), pp. 95-107.
57. D. B. Taulbee and J. Van Osdol, *Modeling turbulent compressible flows: the mass fluctuating velocity and the squared density*, AIAA Paper 91-0524, 29<sup>th</sup> Aerospace Sciences Meeting, Reno, NV, 1991.
58. M. Gittings, R. Weaver, M. Clover, T. Betlach, N. Byrne, R. Coker, R. Dendy, E. Hueckstaedt, K. New, W. R. Oakes, D. Ranta and R. Stefan. *The RAGE radiation-hydrodynamic code*, Comput. Sci. Disc., vol. 1, 2008.
59. M. J. Steinkamp, *Spectral analysis of the turbulent mixing of two fluids*, Tech. Rep. LA-13123-T, Los Alamos National Laboratory, Los Alamos, NM, 1996.
60. P. V. Dankwartz, *Continuous flow systems*, Chem. Eng. Sci. 2 (1953), pp. 1-13.
61. M. J. Steinkamp, M. Gittings, R. Weaver and F. H. Harlow. *Implementation of a mix model into RAGE*, JOWOG 32M, Tech. Rep. LA-UR-01-0572, 2001.
62. M. Vetter and B. Sturtevant, *Experiments on the Richtmyer-Meshkov instability of an air/SF<sub>6</sub> interface*, Shock Waves 4 (1995), pp. 247-252.
63. M. Andrews, *Turbulence by Design*, LDRD Project #20090058DR.
64. Eulerian Applications Code Team, *xRAGE Users Manual*, Code Version 1009.02, LA-CP-08-01044, Los Alamos National Laboratory, Apr. 26, 2011.
65. J. Fincke, N. E. Lanier, S. H. Batha, R. M. Hueckstaedt, G. R. Magelssen, S. D. Rothman, K. W. Parker, C. J. Horsfield, *Effect of convergence on growth of the Richtmyer-Meshkov Instability*, Laser and Particle Beams, 23 (2005), pp. 21-25.

66. J. R. Fincke, N. E. Lanier, S. H. Batha, R. M. Hueckstaedt, G. R. Magelssen, S. D. Rothman, K. W. Parker and C. J. Horsfield, (2004), *Postponement of saturation of the Richtmyer-Meshkov instability in a convergent geometry*, Phys. Rev. Lett. 93 (2004), 115003.
67. G. R. Magelssen, J. A. Cobble, I. L. Tregillis, M. J. Schmitt, S. H. Batha, P. A. Bradley and K. A. Defriend-Obrey, *Single-shell direct-drive capsule designs to study effects of perturbations on burn*, Journal of Physics Conference Series 244 (2010), 022006.
68. P. A. Bradley, J. A. Cobble, S. C. Hsu, G. R. Magelssen, T. J. Murphy, M. J. Schmitt, I. L. Tregillis, N. S. Vinyard, F. J. Wysocki and S. M. Finnegan, *Mix in Defect Imaging Experiments (DIME-I) on Omega*, LA-UR-11-03504, Poster, Anomalous Absorption Conference, San Diego, CA, June 2011.
69. F. Poggi, M. Thorembey and G. Rodriguez, *Velocity measurements in gaseous mixtures induced by Richtmyer-Meshkov instability*, Phys. Fluids 10 (1998), pp. 2698-2700.
70. M. S. Mohamed and J. C. Larue, *The decay power law in grid-generated turbulence*, J. Fluid Mech. 219 (1990), pp. 195-214.
71. G. Comte-Bellot and S. Corrsin, *The use of a contraction to improve the isotropy of grid-generated turbulence*, J. Fluid Mech. 25 (1966), pp. 657-682.
72. R. D. Mehta, O. Inoue, L. S. King and J. H. Bell, *Comparison of experimental and computational techniques for plane mixing layers*, Phys. Fluids 30 (1987), pp. 2054-2062.
73. M. M. Rogers and R. D. Moser, *Direct simulation of a self-similar turbulent mixing layer*, Phys. Fluids 6 (1994), pp. 903-923.
74. P. E. Dimotakis, *Free shear layer*, Caltech University, Available at <http://www.dimotakis.caltech.edu/facilities.html>.
75. M. J. Andrews, *RTI3D code*, Los Alamos National Laboratory, Los Alamos, NM.
76. G. Dimonte and M. Schneider, *Density ratio dependence of Rayleigh-Taylor mixing for sustained and impulsive acceleration histories*, Phys. Fluids 12 (2000), pp. 304-321.
77. A. W. Cook, W. Cabot and P. L. Miller, *The mixing transition in Rayleigh-Taylor instability*, J. Fluid Mech. 511 (2004), pp. 333-362.
78. A. W. Cook and P. E. Dimotakis, *Transition stages of Rayleigh-Taylor instability between miscible fluids*, J. Fluid Mech. 443 (2001), pp. 69-99.
79. Illustration of Texas A&M University gas channel experiment, provided by M. J. Andrews, 2008.
80. A. Banerjee, W. N. Kraft and M. J. Andrews, *Detailed measurements of a statistically steady Rayleigh-Taylor mixing layer from small to high Atwood numbers*, J. Fluid Mech. 659 (2010), pp. 127-190.
81. A. Burrows, *Supernova explosions in the universe*, Nature 403 (2000), pp. 727-733.
82. A. Llor, *Statistical Hydrodynamic Models for Developed Mixing Instability Flows*, Lect. Notes Phys. 681, Springer, Berlin Heidelberg, 2005.